Single impurity atoms immersed in an ultracold gas

Dissertation

zur

Erlangung des Doktorgrades (Dr. rer. nat.)

der

Mathematisch-Naturwissenschaftlichen Fakultät

der

Rheinischen Friedrich-Wilhelms-Universität Bonn

vorgelegt von

Nicolas Spethmann

aus

Augsburg

Bonn 2012

Angefertigt mit Genehmigung der Mathematisch-Naturwissenschaftlichen Fakultät

der Rheinischen Friedrich-Wilhelms-Universität Bonn

1. Gutachter: Prof. Dr. Dieter Meschede
2. Gutachter: Prof. Dr. Artur Widera

Tag der Promotion: 15.05.2012
Erscheingungsjahr: 2012

Abstract

In this thesis, experiments with an ultracold gas doped with few and single atoms of another species are presented.

The techniques to adequately prepare and manipulate an ultracold Rb gas and to dope it with a precisely known number of few Cs atoms are presented. These techniques allow the time-resolved observation of the sympathetic cooling of initially laser-cooled, cold impurity atoms into the ultracold temperature regime of the Rb buffer gas. During the cooling, the confinement of the impurity atom is enhanced to a reduced volume inside the buffer gas, which increases the interspecies collision rate. By analyzing the cooling process, the interspecies scattering cross section is estimated.

The lifetime of the resulting hybrid system is limited by three-body recombination of the impurity atom with atoms of the buffer gas. The atomic resolution of the impurity atom number allows the determination of the lifetime atom-by-atom. Additional information is gained from the precisely known fluctuations of the number of lost impurity atoms. This information is exploited to assign the three-body losses unambiguously to a single loss channel.

The interaction of an impurity atom in a quantum-mechanical superposition state with the buffer gas is of special interest for future experiments. First experiments into this direction are presented at the end of the thesis.

Zusammenfassung

Gegenstand dieser Arbeit ist ein mit wenigen und einzelnen Fremdatomen dotiertes, ultrakaltes Gas.

Die notwendigen Techniken, um ein ultrakaltes Rb Gas zu erzeugen, geeignet zu manipulieren und gezielt mit einer genau bekannten Anzahl weniger Cs Atome zu dotieren, wurden im Rahmen dieser Arbeit entwickelt und werden vorgestellt. Diese Techniken erlauben es, das sympathetische Kühlen der anfangs laser-gekühlten, kalten „Störatome“ in das Regime ultrakalter Temperaturen des Rb Puffergases zeitaufgelöst zu beobachten. Während des Kühlens wird das Störatom in einem immer kleiner werdenden Volumen innerhalb des Puffergases gefangen, was zu einer Verstärkung der Stoßrate führt. Durch die Analyse des Kühlvorgangs wird die Streulänge der elastischen Zweikörperstöße abgeschätzt.

Die Lebensdauer des so erzeugten Hybridsystems ist begrenzt durch Dreikörperrekombination des Störatoms mit Atomen des Puffergases. Die atomare Auflösung der Anzahl der Störatome erlaubt die Bestimmung der Lebensdauer Atom für Atom.

Die präzise bekannten Fluktuationen der Anzahl der verlorenen Störatome bieten zusätzliche Information, die genutzt wird, um die Dreikörperrekombination eindeutig einem einzigen Verlustkanal zuzuordnen.
Von besonderem Interesse für zukünftige Experimente ist die Wechselwirkung von Störatomen in einem quantenmechanischen Superpositionszustand mit dem Puffergas. Erste Experimente in diese Richtung werden am Ende der Arbeit vorgestellt.

Parts of this thesis have been published in the following paper:

- N. Spethmann, F. Kindermann, S. John, C. Weber, D. Meschede and A. Widera, *Inserting single Cs atoms into an ultracold Rb gas*, Applied Physics B, doi: 10.1007/s00340-011-4868-6 (2012).

Contents

Introduction

The development of laser cooling [1, 2] and evaporative cooling [3] allows to cool atomic samples routinely into the regime of ultracold temperatures. This has enabled the production of Bose-Einstein condensates (BECs), matter waves governed by the laws of quantum mechanics [4, 5]. First experiments demonstrated striking features of the quantum world, like the interference of matter waves [6, 7], the creation of vortices in a quantum gas [8, 9] and the coupling of atoms out of a BEC, forming a coherent atom laser [10–12]. In the recent years, these macroscopic quantum objects proved to be excellent model systems to study many-body physics [13].

In the few-body regime, single neutral atoms have been employed for many fascinating experiments, as for instance a quantum register [14], the quantum walk in position space [15] or the entanglement of single Rydberg atoms [16, 17]. These experiments feature intrinsically single atom resolution and usually have a very good spatial resolution, ideally single-site resolution [18]. In general, however, the realization of coherent interactions between single atoms, that are usually laser cooled and have therefore a rather large temperature, is challenging.

In a BEC, in contrast, coherent interactions dominate. In this case, detection and manipulation on a single atom level and with high spatial resolution are quite demanding. Recently, some experiments combined features of these rather separated fields of research, as for example the demonstration of single atom detection and manipulation in BECs [19–21], the study of an ensemble of single fermionic atoms in a small bosonic field [22] and the creation of a system of a few interacting degenerate fermions [23].

The study of these atomic systems is facilitated by the extremly good isolation from the enviroment. Furthermore, impurities can be ruled out completely, allowing to study perfect, defect-free model systems. However, many interesting effects in physics arise because of the interplay of an impurity with a many-body system. This is the starting-point of the experiments presented in this thesis. The goal is the controlled doping of an ultracold many-body model system with single neutral impurity atoms, to create a hybrid system.

Here, the interactions between the impurity atom and the buffer gas are of crucial importance. Recently, in a similiar approach, a system of a BEC doped with a single ion has been created [24, 25]. In this case, interactions are dominated by the charge of the ion, leading to complex interaction dynamics [26]. In our system, in contrast, the impurity atom is neutral. Therefore, interactions are completely

determined by s-wave scattering, as in the ultracold gas itself. Fundamental features of quantum gases, as for example superfluidity [27], are caused by these interactions. Furthermore, Feshbach resonances allow the tuning of the scattering length [28, 29]. This has been exploited in a variety of experiments, as for example the creation of dimers [30] and entanglement [31], and the condensation of fermionic pairs [32–34].

This thesis presents experiments with a thermal ultracold rubidium (Rb) gas, doped with few and single caesium (Cs) atoms. Initially, Cs is captured in a magneto-optical trap. Its temperature is therefore about two orders of magnitude larger than the temperature of the ultracold gas, that is cooled by evaporative cooling. After bringing both subsystems into contact, we observe the cooling of the impurity atom to the temperature of the buffer gas. This provides single atoms cooled far below the limit of standard laser cooling. In a few single species experiments, preparation of ultracold, single neutral atoms has been demonstrated by extraction out of an ultracold gas [23, 35]. With our hybrid system, it might be possible in future experiments to cool impurity atoms containing quantum information by immersing them into a BEC, without affecting the inscribed quantum state [36, 37]. Additionally, the creation of a doped quantum gas should pave the way to study polarons, a quasi-particle of the impurity dressed with atoms from the buffer gas, as observed in a slightly imbalanced mixture of fermions [38].

Furthermore, the impurity atom can be employed as a probe for the many-body system. In this thesis, first steps towards this goal are presented. Besides measuring the temperature of the buffer gas, the time-resolved observation of the cooling of the impurity atom allows estimating the interspecies scattering cross section. During the cooling, the impurity atom becomes localized in a reduced volume inside the buffer gas because of the species-selective trap employed. In future experiments, with comparable techniques, the spatially resolved probing of a BEC could be realized. Furthermore, the coherence of the quantum gas could be analyzed by employing the impurity atom as coherent probe [39, 40]. In certain regimes, the probing by the impurity atom is a negligible perturbation.

Indeed, in the experiments discussed in this thesis, the buffer gas is not affected by the interaction with the impurity atom. This simplifies the interpretation of the observed three-body recombination considerably. Owing to the observation with atomic resolution, the loss of impurity atoms immersed in the buffer gas can be ascertained to be caused by an inelastic collision of an impurity atom with two atoms of the buffer gas.

In most ultracold atom experiments, averaged quantities of a large number of atoms are probed, usually with only small statistical fluctuations of this quantity. How-

ever, fluctuations allow to directly observe the statistics governing the properties of quantum gases. The observation of atom number fluctuations, for instance, has been employed to directly observe sub-Poissonian number statistics in a BEC [41] and the number squeezing in a Mott insulator [21, 42].

In our experiment, the fluctuations of the number of lost impurity atoms, that are on the same order as the impurity atom number itself, facilitate identifying the respective loss events of the three-body recombination. The occurrence of the loss of a pair of impurity atoms, for example, shows that collisions involving more than one impurity atom can be neglected in the regime studied in this thesis. In future experiments, this could be employed as a sensitive probe. Many interesting effects arise at the transition from a two-body to a many-body system. Two-body collisions dominate the interaction in low density samples on short time scales, as is observed in this thesis in the thermalization measurement. When more atoms come into play, as for instance in three-body recombination [43–45], new effects arise, in this example molecule formation. In our experiment, this transition could be studied in the future in a controlled way by increasing the number of impurity atoms. Thus, it should be possible to study the increase in complexity at a fundamental level, caused for example by the onset of collisions with more than one impurity atom involved. This could be observed by an enhanced probability for the loss of pairs of impurity atoms.

The experiments presented in this thesis demonstrate the creation of the hybrid system and provide insight into the interaction of both subsystems. This should pave the way for the scenarios outlined above.

Chapter 1

Production and guided magnetic transport of ultracold Rb

The preparation of ultracold gases, as the first constituent of the hybrid system, is introduced in this chapter. The goal is a Rb sample with high phase-space density at the position, where in a next step single Cs atoms are cooled and trapped. The same quadrupole coils as close as possible to the sample are employed for magnetic trapping of ultracold Rb and, in a later step, for trapping single Cs atoms in a magneto-optical trap (MOT). This facilitates to achieve the necessary strong magnetic field gradient for both sub-systems. To avoid Majorana spin flips [46], that lead to loss of atoms from the trap, the quadrupole coils are combined with an Ioffe coil for trapping ultracold Rb, forming a **Qu**adrupole-**I**offe-**C**onfiguration (QUIC) trap [47]. As a consequence, the trap center of the QUIC is shifted to a position about 7 mm apart from the quadrupole field center. In the QUIC trap, Rb is precooled by evaporative cooling into the ultracold regime. Subsequently, a transport of the Rb sample back to the center of the apparatus, where Cs can be trapped, is necessary. The transport has to be adiabatic to avoid excitations and heating of the ultracold cloud. Furthermore, the transport needs to be sufficiently precise and reproduceable to accurately and reliably adjust the spatial position of the Rb cloud relative to the single atom trap. Furthermore, the spatial confinement should not significantly decay during the transport.

Ultracold atoms stored in magnetic traps can be moved by varying the inhomogeneouse magnetic field creating the trap. In some experiments, a sequence of quadrupole coils has been employed for this purpose [48, 49]. We use a similar magnetic transport, which works with the single pair of quadrupole coils present. As a consequence, the confinement decays during this purely magnetic transport, leading to a decrease of the atomic density and impeding evaporative cooling in the shifted trap. Therefore, an optical dipole trap is used as a guiding field, allowing to keep

the confinement constant during the magnetic transport. Subsequently, a second dipole trap is intersected with the guiding field to form a crossed dipole trap. The manipulation of the internal degree of freedom of the Rb gas, stored in this trap in close vicinity to the Cs MOT, is demonstrated. A final evaporative cooling stage is applied, allowing to cool the sample to degeneracy.

1.1 Magnetic trap and magnetic transport

In the following, the concept to produce degenerate quantum gases in our experiment is briefly summarized. The employed techniques are well established and used in many labs, so that for details we reference to the literature [50–52].

1.1.1 Magnetic trapping of ultracold Rb

The starting point of our experiment is the preparation of a ^{87}Rb sample in the QUIC trap. Laser cooling is employed as a precooling stage. For this, an atomic beam is produced by pushing atoms out of a vapour pressure MOT. This atomic beam loads a second MOT (UHV-MOT) in an ultra-high vacuum with a pressure of about 10^{-11} mbar, that allows storing the sample with a decay time constant of 160 s, limited by collisions with atoms of the background gas. The phase-space density in the UHV-MOT is about 10^{-8}.

In a MOT, the energy scale of the atoms is limited to the recoil energy $\hbar^2k^2/(2m)$ by scattering of photons, which is much larger than the typical energy scale of ultracold gases. Therefore, in the next step, a conservative potential without scattering of photons is required. For this, a magnetic trap is employed, that relies on the interaction of the magnetic moment of the atom $\mu = g_\mathrm{f}\mu_\mathrm{B}m_\mathrm{F}$ and an inhomogenous magnetic field B, where μ_B is Bohr's magneton, g_f the Landé factor and m_F the projection onto the quantization axis. Hence, the resulting potential $V = g_\mathrm{f}\mu_\mathrm{B}m_\mathrm{F}B$ depends on the Zeeman state of the atom. As a consequence of the Maxwell equations, it is not possible to create a static magnetic field maximum in free space. Therefore, magnetic trapping is only possible for those states, which experience a minimizing of their energy for decreasing magnetic field (low field seekers) and can therefore be trapped in a field minimum [53]. For ^{87}Rb and ^{133}Cs, this is the case for states with $m_\mathrm{F} > 0$.

In the next step of the sequence, the UHV-MOT is switched off, and the Rb gas is optically pumped into the $|F = 2, m_\mathrm{F} = 2\rangle$ state. Subsequently, the sample is transferred into a magnetic quadrupole trap, which is then transformed into the QUIC. In this trap, forced evaporative cooling using a microwave transition is applied. Loading of the UHV-MOT requires about 30 – 40 s, the evaporative cooling

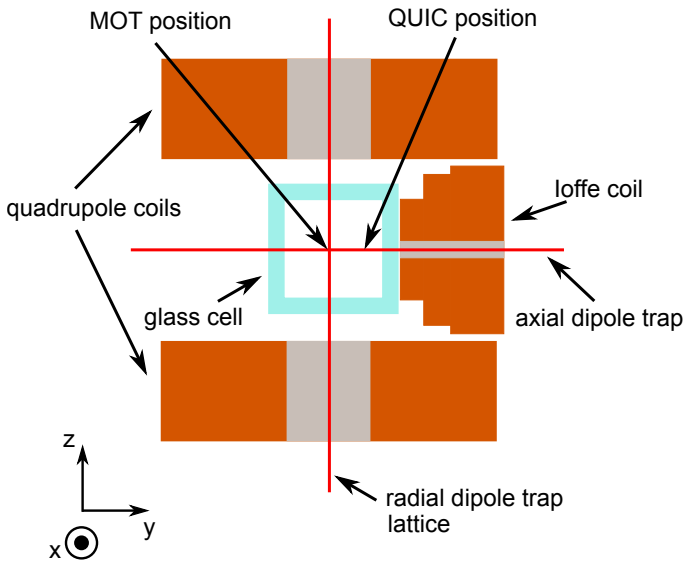

Figure 1.1: Schematic setup of the experiment. Single Cs atoms can be trapped in a high-gradient MOT at the center ($x = y = z = 0$) of the apparatus. Ultracold Rb clouds are prepared in the QUIC-type magnetic trap at a position about 7 mm apart from the center ($y \approx 7$ mm, $x = z = 0$). By the guided magnetic transport, the Rb gas is moved along the y-direction to the center in close vicinity to the single atom MOT.

in the QUIC takes about 20 s, so that one cycle of the experiment needs approximately one minute. A more detailed description of this part of the apparatus and the employed techniques is given in [54–58]. Fig. 1.1 shows a simplified sketch of the setup.

The Rb sample can be cooled to quantum degeneracy by evaporative cooling in this stage of the sequence. A typical time evolution of the phase-space density during the evaporative cooling is presented in Fig. 1.2(a). For probing the atomic sample, time-of-flight imaging is employed [59]. For this, the trap is switched off, the sample drops due to gravity and expands. After a certain time-of-flight, a resonant light pulse is applied to the sample and the shadow of the atoms is recorded on a CCD chip. From the determined optical density, the atomic density is calculated. The expansion of the gas maps the momentum distribution onto a spatial distribution and allows to extract the temperature. Due to the resonant photon scattering involved, this probing heats the sample and destroys the quantum state. Therefore, for each realization a new experimental shot is performed. In Fig. 1.2(b) time-of-flight absorption images of a BEC with $\approx 3 \times 10^5$ atoms coupled out of the QUIC are shown.

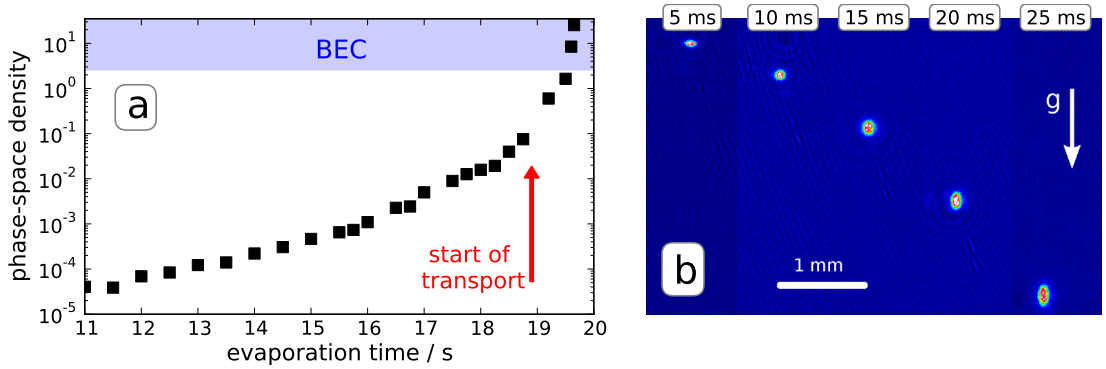

Figure 1.2: Ultracold Rb in the QUIC trap. **a**) Phase-space density during the last stage of evaporation in the QUIC trap. Errors are on the order of 10 % and left out for clarity. The red arrow indicates the point where typically the evaporation is stopped and Rb is moved to the center with the guided magnetic transport. **b**) Time-of-flight images of a BEC released from the magnetic QUIC trap, the temperature of the atoms is about 200 nK.

1.1.2 Magnetic transport

For the transport, the evaporative cooling of Rb in the QUIC is typically stopped before the phase-space density comes close to degeneracy, indicated by the red arrow in Fig. 1.2(a). In this way, more robust thermal clouds are moved which can be cooled further in the crossed dipole trap. The transport is accomplished by the controlled lowering of the magnetic trap described in the following.

In a QUIC trap, an Ioffe and quadrupole field nearly cancel at the trap center, which is in our case at a distance of about 7 mm from the zero-crossing of the quadrupole field (see Figs. 1.1 and 1.3). The magnetic field can be approximated by a combination of a quadrupole and a dipole field

$$\vec{B}_{\mathrm{QUIC}}(\vec{r}) = \vec{B}_{\mathrm{Q}}(\vec{r}) + \vec{B}_{\mathrm{I}}(\vec{r}), \tag{1.1}$$

where

$$\vec{B}_{\mathrm{Q}}(\vec{r}) = \xi(\vec{e}_x + \vec{e}_y - 2\vec{e}_z) \tag{1.2}$$

and

$$\vec{B}_{\mathrm{I}}(\vec{r}' = \vec{r} - y_{\mathrm{I}}\vec{e}_y) = \frac{3py'\vec{r}' - pr'^2\vec{e}_y}{r'^5}. \tag{1.3}$$

Here, $\xi \approx 6.2$ G/(A cm) is the gradient of the quadrupole coils, $p \approx 27.4$ G cm^3/A is the dipole moment of the Ioffe coil and $y_{\mathrm{I}} \approx 30$ mm is the distance between Ioffe and quadrupole coils.

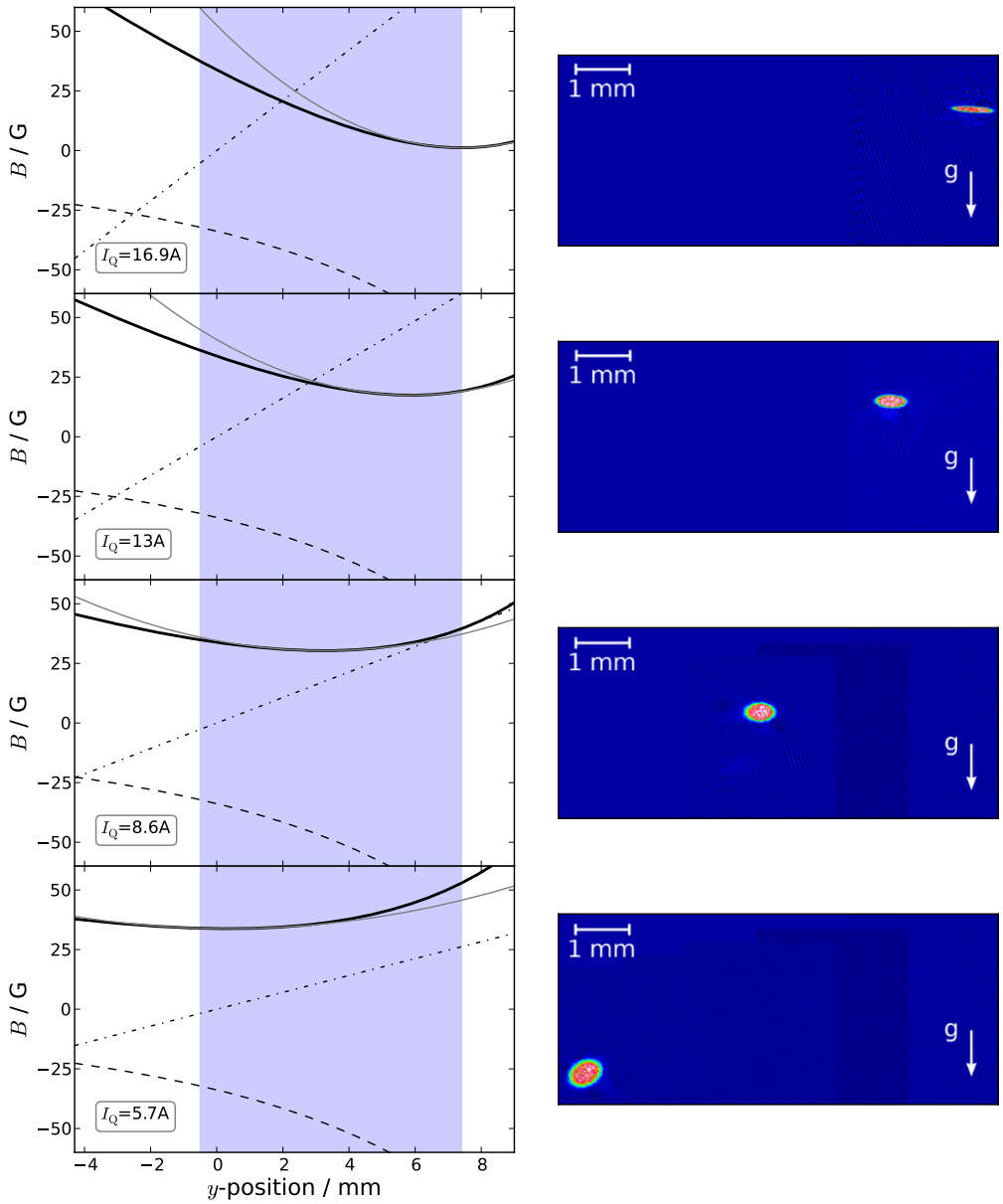

Figure 1.3: Purely magnetic transport at four different stages. From top to bottom: $I_Q = 16.9$ A, $I_Q = 13$ A, $I_Q = 8.6$ A, $I_Q = 5.7$ A. **Left column:** Cut through the magnetic field in y-direction at different transport stages. Shown are the Ioffe field (dashed line), the quadrupole field (dashed-dotted line) and the absolute value of the effective magnetic field $|\vec{B}_{\mathrm{QUIC}}|$, along with the harmonic approximation (light gray). The shaded region indicates the field of view of the absorption images shown in the right column. **Right column**: Absorption images of the Rb cloud in the magnetic trap corresponding to the field configuration shown in the left panel. Due to the gravitational sag g/ω_r^2, the center of the trap shifts also in x-direction. To cover the entire field of view of more than 7 mm, for this measurement the CCD camera is moved laterally several times. The position of each image is calibrated such that it can be displayed in a sufficiently large frame. The remaining part of the frame is filled with the color corresponding to the background.

The remaining offset field at the center of the trap is adjusted to $B_0 \approx 1$ G, in order to avoid Majorana losses due to spin flips [46]. By exciting the center of mass motion of trapped atoms we measured the trap frequencies in this compressed trap (at $I_\mathrm{Q} = I_\mathrm{I} = 16.9$ A) to be $\omega_\mathrm{r} = 2\pi \times [179 \pm 1]$ Hz ($\omega_\mathrm{a} = 2\pi \times [17.9 \pm 0.3]$ Hz) for the radial direction along x and z (axial direction along y), in good agreement with calculated values using ξ and p.

By decreasing the quadrupole field strength, the center of the trap moves towards the quadrupole field zero crossing at the center of the apparatus ($x = y = z = 0$). Using Eq. (1.1), the position of the trap center y_0 is calculated to be

$$y_0 = -\left(\frac{6 I_\mathrm{I} p}{I_\mathrm{Q} \xi}\right)^{\frac{1}{4}} + y_\mathrm{I}. \tag{1.4}$$

Here, I_Q is the current running through the quadrupole coil and I_I is the current of the Ioffe coil. In the left column of Fig. 1.3, the corresponding magnetic fields along the transport direction (y-direction, $x = z = 0$) are plotted, showing how the field components add up to the effective field for varying values of I_Q. In the right column of Fig. 1.3 absorption images of a few million atoms with a temperature of about 1 µK in the corresponding trap are presented. These images illustrate that, upon decreasing I_Q, the cloud moves towards the center of the apparatus ($y = 0$). At the same time, however, the confinement decreases, leading to a larger cloud and a larger gravitational sag.

Both observations, changing position and confinement, are quantified in Fig. 1.4. The atoms move along the y-direction as the quadrupole current I_Q is decreased (Fig. 1.4(a)), in good agreement with the expectation according to Eq. (1.4). It should be noted that the new trap center is given by the point where the slope of the quadrupole field starts to be larger than the slope of the Ioffe field rather than its absolute value. Therefore it is also possible to move the trap beyond the zero crossing of the quadrupole field.

Fig. 1.4(b) shows the measured radial trap frequency ω_r (along the x-direction) during the transport. We model this decay of ω_r as a function of quadrupole current I_Q. This is important in order to counteract the relaxing confinement by an optical guiding field, discussed in section 1.2. Knowing the expression for the magnetic field according to Eq. (1.1), ω_r can be calculated by a harmonic approximation in the center of the trap

$$B_{x,\mathrm{harmonic}} = B_0 + \frac{\partial^2 |\vec{B}_\mathrm{QUIC}|}{\partial x^2} x^2, \tag{1.5}$$

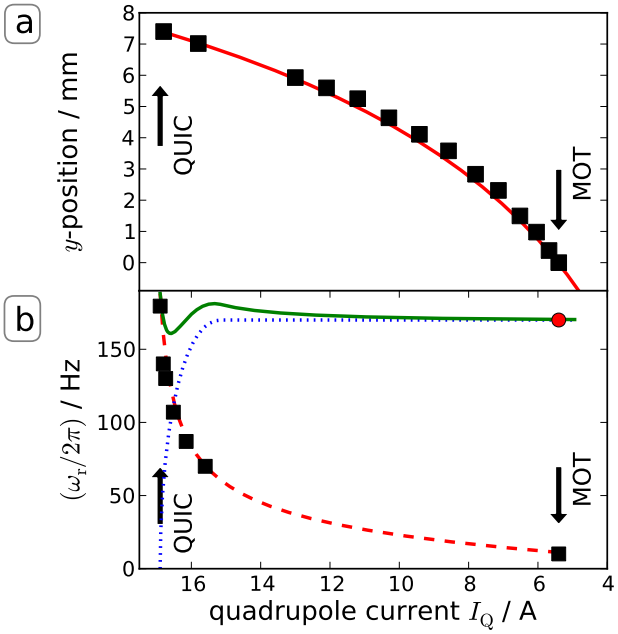

Figure 1.4: Magnetic transport of ultracold Rb. **a)** By ramping down the quadrupole current I_Q while keeping the Ioffe current I_I constant, the ultracold gas can be moved from the original QUIC position (left side, $I_Q = 16.9$ A) across a distance of about 7 mm to the center of the apparatus (Cs MOT position, $I_Q \approx 5$ A). The red solid line shows the expected position according to Eq. (1.4). **b)** Measured trap frequencies at different transport stages. The radial trap frequency in the QUIC trap of $\omega_r = 2\pi \times 179$ Hz is strongly decreased to about $2\pi \times 10$ Hz at the end of the purely magnetic transport. The dashed red line shows the expected trap frequencies according to Eq. (1.6). The decay of the trap frequencies is compensated for by using a dipole trap as guiding field (blue dotted line), see section 1.2. The effective trap frequencies of the guided magnetic transport are approximately constant (green solid line). The errorbars for the presented data are of a size comparable to the markersize and are therefore not shown.

where

$$\frac{\partial^2 |\vec{B}_{\mathrm{QUIC}}|}{\partial x^2} = \frac{1}{2}\left(\frac{(I_Q\xi y^4 - 3I_Q\xi y^3 y_I + 3I_Q\xi y^2 y_I^2 - I_Q\xi y y_I^3 + 2I_I p)^2}{(y_I - y)^6}\right)^{\frac{1}{2}} \times \frac{(I_Q\xi(y_I - y)^5 - 3I_I p y + 3I_I p y_I)^2}{(y_I - y)^4 (I_Q\xi y^4 - 3I_Q\xi y^3 y_I + 3I_Q\xi y^2 y_I^2 - I_Q\xi y y_I^3 + 2I_I p)^2}$$

and

$$B_0 = |\vec{B}_{\mathrm{QUIC}}(y_0)|.$$

The potential and, correspondingly, the radial trap frequency ω_r is then given by

$$V = \mu_\mathrm{B} g_\mathrm{f} m_\mathrm{F} B_{x,\mathrm{harmonic}} = \frac{m_\mathrm{Rb}}{2}\omega_\mathrm{r}^2 x^2. \tag{1.6}$$

Here, m_Rb is the mass of the ^{87}Rb atom. The measured values for ω_r presented in Fig. 1.4(b) are in good agreement with our model according to Eq. (1.6).

It should be noted that Eq. (1.5) approximates the field on the symmetry axis of the QUIC coils ($x = z = 0$). Due to the gravitational sag the atoms are shifted away from this axis ($x \neq 0$), which in turn leads to a change in the magnetic potential. This effect only becomes noticeable for very low trap frequencies, or long transport distances. The agreement with the experimental observation, however, is good for all parameters considered. Also, using the optical guiding field (see section 1.2), the cloud is forced to stay approximately on the symmetry axis, and the knowledge of trap frequency decay at the start of the transport is sufficient.

Since the goal of the transport is a Rb sample with high atomic density at the Cs MOT position at x = y = z = 0, both expansion and sag are not favorable.

1.2 Dipole trap as guiding field and spin-independent trap

Magnetic traps only allow the storing of low field seeking states, as has been discussed above. The study of spin dynamics in magnetic traps is therefore not with all spin states possible. In our experiment, it is required to transfer the Rb sample into spin states, which cannot be trapped in magnetic traps (high field seekers), as will be discussed later in this chapter (see section 1.3). These limitations of magnetic trapping can be overcome by employing a far detuned optical dipole trap. When the frequency is properly chosen, all hyperfine and Zeeman states of the atom experience approximately the same potential. Additionally, the limitations of the magnetic transport discussed above can be avoided partially by using an additional far detuned optical dipole trap as guiding field.

1.2.1 Optical dipole trap for ultracold Rb

Dipole traps are a well established technique employed in many ultracold atom experiments. Therefore, only the basic concept is briefly introduced and the required equations are given. A more thorough treatment can be found in [60, 61].

Dipole potential and spontaneous photon scattering

The mechanism of dipole traps relies on the interaction of the light field with the induced dipole moment of the atoms. Due to this interaction, the atoms experience

a potential, depending on the wavelength of the dipole trap, proportional to the intensity of the light field.

In general, all possible transitions of the atom contribute to the resulting potential. Therefore, the substructure of the atom, consisting of fine, hyperfine and Zeeman levels, has to be considered. However, for all dipole traps employed in our experiment, the detuning of the dipole trap is large compared to the hyperfine and Zeeman splittings. Therefore, only the finestructure transitions are considered by summing over the contributions of the D1 and D2 line. The corresponding potential is given by

$$U_{\mathrm{DT}} = -\frac{3\pi c^2 I}{2} \left[f_{\mathrm{osc,D1}} \frac{\Gamma_{\mathrm{D1}}}{\omega_{\mathrm{D1}}^3} \left(\frac{1}{\omega_{\mathrm{D1}}-\omega} + \frac{1}{\omega_{\mathrm{D1}}+\omega} \right) + f_{\mathrm{osc,D2}} \frac{\Gamma_{\mathrm{D2}}}{\omega_{\mathrm{D2}}^3} \left(\frac{1}{\omega_{\mathrm{D2}}-\omega} + \frac{1}{\omega_{\mathrm{D2}}+\omega} \right) \right] \tag{1.7}$$

where c is the speed of light, I the intensity of the dipole trap, ω_{D1} (ω_{D2}) the frequency of the D1- (D2-) transition, $f_{\mathrm{osc,D1}}$ ($f_{\mathrm{osc,D2}}$) the oscillator strength of the D1- (D2-) transition, Γ_{D1} (Γ_{D2}) the natural linewidth of the D1- (D2-) transition and ω the frequency of the dipole trap. Depending on the frequency of the dipole trap, the atom experiences either an attractive (red detuned) or a repulsive (blue detuned) potential.

All dipole traps employed in this thesis are red detuned, so that the atoms are always attracted into the regions of high intensity. In the case of the running wave dipole trap introduced in this chapter, the trap is formed by a focused Gaussian beam.

The trapping potential in a MOT is based on the interaction with near resonant light, therefore the atoms scatter photons with a high rate in this dissipative trap. Optical dipole traps, in contrast, rely on the dispersive interaction, the created potential is nearly conservative. Depending on the detuning of the dipole trap, photon scattering can strongly by suppressed.

The total photon scattering rate, including Rayleigh and Raman scattering, can be written as

$$\Gamma = -\frac{3\pi c^2 I}{2\hbar} \left[f_{\mathrm{osc,D1}} \frac{\Gamma_{\mathrm{D1}}^2 \omega^3}{\omega_{\mathrm{D1}}^6} \left(\frac{1}{\omega_{\mathrm{D1}}-\omega} + \frac{1}{\omega_{\mathrm{D1}}+\omega} \right)^2 + f_{\mathrm{osc,D2}} \frac{\Gamma_{\mathrm{D2}}^2 \omega^3}{\omega_{\mathrm{D2}}^6} \left(\frac{1}{\omega_{\mathrm{D2}}-\omega} + \frac{1}{\omega_{\mathrm{D2}}+\omega} \right)^2 \right]. \tag{1.8}$$

The spontaneous photon scattering rate scales with I/Δ^2, whereas the dipole po-

tential scales with I/Δ, where Δ is the detuning. For a sufficiently far detuned dipole trap, the spontaneous scattering rate can be minimized. To provide a sufficiently strong potential, the intensity has to be increased correspondingly. Typical values for Rb stored in the running wave dipole trap, introduced in the following, are $U_{\mathrm{DT}} \approx h \times 1$ MHz and $\Gamma_{\mathrm{DT}} \approx 1\ \mathrm{s}^{-1}$.

Dipole trap in the experiment

For the dipole trap, a Nd:YAG laser at 1064 nm boosted by a fibre amplifier is used. The power is divided to provide two beams to eventually form a crossed dipole trap. Both beams intersect at right angle at the center of the apparatus, so that a good three dimensional confinement is achieved. One beam is propagating in the axial (y) direction through a hole in the Ioffe coil (see also Fig. 1.1), forming the "axial" optical trap. The other beam propagates along the radial (z) direction, forming the "radial" trap. The power of each of the beams is stabilized by a home-built servo loop (see [57]) to a maximum power of 3 W (axially) or 0.6 W (radially). Table 1.1 summarizes the beam and trap parameter.

1.2.2 Guided magnetic transport

The axial dipole trap propagates along the transport direction. The parameters of this trap are chosen such, that it forms a nearly cylindrical potential with a radius of $w_{\mathrm{axial}} \approx 100$ µm on the distance from the QUIC center to a position in close vicinity of the Cs MOT about 7 mm apart. Through this guiding potential the atoms are moved by the magnetic transport.

For this, the power for the axial dipole trap is ramped up during the magnetic transport, such that $\omega_{\mathrm{r}} = \sqrt{\omega_{\mathrm{QUIC}}^2 + \omega_{\mathrm{dipole}}^2}$ is kept approximately constant in the combined magnetic and optical potential (see Fig. 1.4(b)), calculating ω_{QUIC} using Eq. (1.6). In this way, a "mode matching" of the cloud into the dipole trap is achieved. The magnetic transport then shifts the atomic cloud along the guiding dipole field. This gradual transfer also makes the transport and the loading into the dipole trap less sensitive to imperfections. For a reasonable range of positions of the axial dipole trap around the center of the apparatus, the transport works without noticeable degradation in phase-space density. This is important because later on this position of the axial dipole trap will be used to change the relative positions of Rb gas and single atom Cs MOT.

To provide a reasonable confinement also along the third direction (y-direction) for the final experiments with the single atom Cs MOT, the radial dipole trap is ramped up within 200 ms while the Rb is stored in the combined magnetic and

λ_{axial}	1064 nm
w_{axial}	100 µm
z_{axial}	30 mm
$P_{\text{max,axial}}$	3 W
λ_{radial}	1064 nm
w_{radial}	48 µm
z_{radial}	7 mm
$P_{\text{max,radial}}$	0.6 W

Cs		Rb	
Γ_{axial}	$0.7\ \text{s}^{-1}$	Γ_{axial}	$0.2\ \text{s}^{-1}$
U_{axial}	54 µK	U_{axial}	30 µK
Γ_{radial}	$0.6\ \text{s}^{-1}$	Γ_{radial}	$0.2\ \text{s}^{-1}$
U_{radial}	49 µK	U_{radial}	27 µK

Table 1.1: Beam parameter of the running wave dipole trap and deduced properties of the corresponding potentials.

optical potential in the center of the apparatus at $x \approx y \approx z \approx 0$. Then, the magnetic fields of the QUIC are quickly switched off (within 1 ms), leaving the sample stored in the purely optical trap. Immediately after switching off the QUIC field, a homogeneous offset field is switched on to provide a quantization axis.

At the end of the transport, the Rb gas is typically cooled by evaporation in the crossed dipole trap. With this final evaporative cooling an optically trapped BEC with atom numbers in the range of $10^4 \ldots 10^5$ atoms can be produced in the center of the apparatus. The advantage of evaporative cooling in the dipole trap rather than transporting a BEC is a significantly higher stability. Small imperfections in the transport that lead to heating can be compensated for by evaporative cooling after the transport. The high trapping frequencies provided by the crossed dipole trap support efficient cooling. Starting the transport with a Rb gas at about 1 µK in the QUIC trap and further evaporating after the transport is experimentally identified as the optimal strategy to produce a BEC after transport.

Thus, the guided transport provides a means to prepare ultracold Rb clouds in the crossed dipole trap at a position that can be chosen in a large parameter range, in particular in the vicinity of the single atom MOT.

1.2.3 Characteristics of the running wave dipole trap

For a precise characterization of the crossed dipole trap realized in the experiment, the trap frequencies are measured.

Trap frequencies

A sample of about 2×10^5 Rb atoms with a temperature of typically 500 nK is produced in the crossed dipole trap with the guided magnetic transport. After that, the trap is adiabatically compressed. This provides atomic samples cooled deep into the trap and facilitates characterizing the trap at different depths, allowing a more precise determination of the parameters. After compression, the intensity of the axial (radial) trap is sinusoidally modulated for a time of typically 200 ms. By parametric excitation the atoms are heated and eventually leave the trap. One way of measuring the trap frequencies is therefore to monitor the loss of atoms for varying modulation frequencies. Alternatively, the heating can directly be observed by measuring the temperature using time-of-flight velocimetry. Especially for atoms cooled deep into the trap like in our case this method is more sensitive, as atoms can significantly be heated before leaving the trap.

In Fig. 1.5 the obtained excitation spectrum is shown for the radial and the axial dipole trap. The behavior is as expected. When the modulation frequency is resonant to the parametric excitation frequency, the temperature of the gas is increased typically by more than a factor of two.

When the axial trap intensity is modulated, an additional peak arises at a frequency of about 650 Hz. This peak stays constant for all values of the laser power of the axial dipole trap beam, its frequency corresponds to the frequency of the radial dipole trap beam for the power used ($I_{\mathrm{radial}} = 0.6$ W). Therefore this peak can be attributed to cross talk between axial and radial trap, when the axial trap is modulated. A similar second peak is observed when modulating the radial dipole trap at low ($I_{\mathrm{radial}} = 0.2$ W) overall power. The frequency of this peak again roughly corresponds to the axial trap at the power used ($I_{\mathrm{axial}} = 2.5$ W). Reasons for this observed cross talk could be a small deviation of the cross angle of 90° between the dipole trap beams, non-harmonic distortion of the trap or symmetry breaking by

modulated beam	power (W)		trap frequency (Hz)	
	radial	axial	theory	experiment
radial	0.6	2.5	326	322 ± 3
radial	0.3	2.5	231	224 ± 3
radial	0.2	2.5	188	191 ± 7
axial	0.6	2	138	128 ± 2
axial	0.6	1	98	93 ± 2
axial	0.6	0.5	69	70 ± 2

Table 1.2: Trap frequencies of the axial and radial dipole trap.

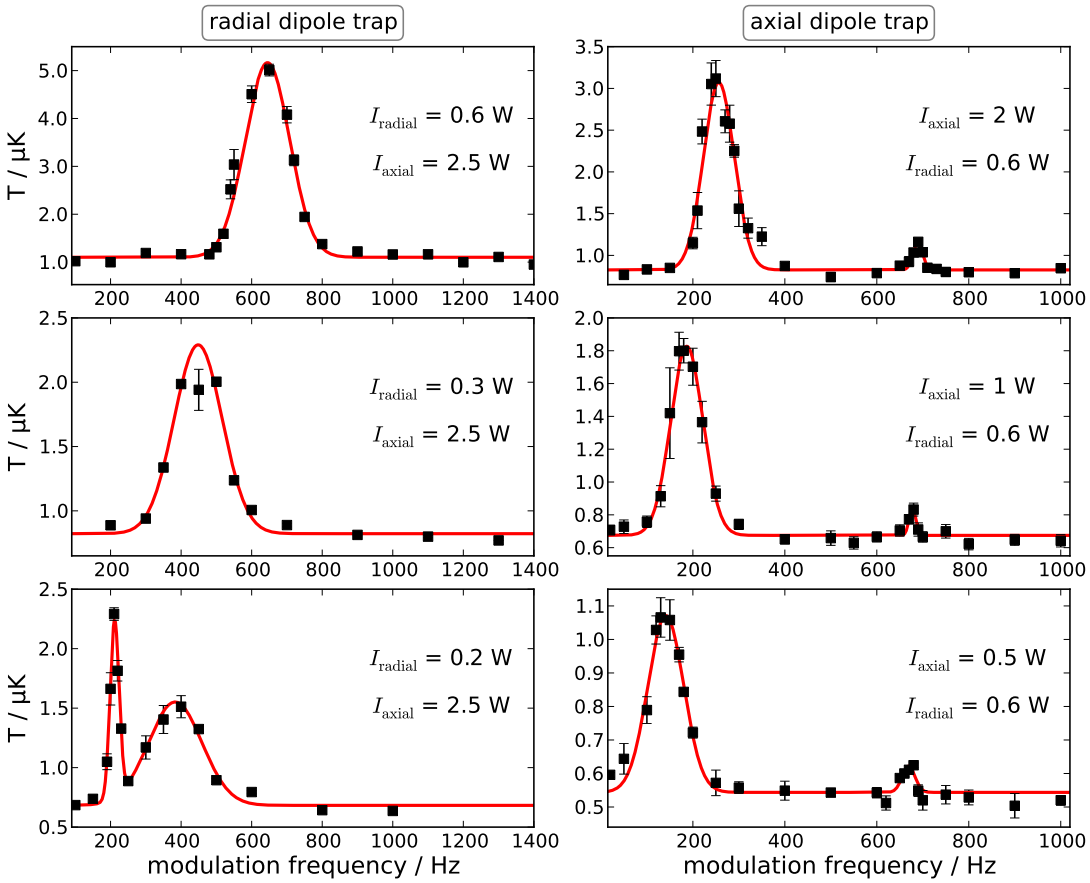

Figure 1.5: Trap frequencies of Rb in the crossed dipole trap. The intensity of either the radial (**left row**) or axial (**right row**) dipole trap beam is modulated. The rise in temperature reveals the trap frequencies for different trap depths. The solid red line is a fit of a sum of two Gaussians.

gravity. The effect is, however, quite small and does not pose any limit.

For a quantitative estimation, the parametric resonance frequencies are obtained from the fits shown in Fig. 1.5. The inferred trap frequencies are listed in Table 1.2, the error indicated are one sigma uncertainties derived from the fits. The expected radial trap frequency can be calculated in harmonic approximation to

$$\omega_r = \sqrt{\frac{4U_0}{m_{Cs} w_0^2}} \tag{1.9}$$

where U_0 is the depth of the potential and w_0 the waist of the focus. In Table 1.2 the expected trap frequencies are listed, showing a reasonable agreement with the measured values. The square root scaling according to Eq. (1.9) is reproduced.

1.3 Manipulation of the internal degrees of freedom

For the insertion of single Cs atoms into the Rb gas discussed in chapter 3, Rb needs to be prepared in a magnetic insensitive $m_F = 0$ state. For experiments dealing with the interspecies interaction, Rb is prepared in the absolute ground state $|1, 1\rangle$. Both states cannot be trapped magnetically. In this section, the manipulation of the internal degrees of freedom of Rb, stored in the crossed dipole trap, is introduced. This manipulation allows the transfer of Rb from the initial $|2, 2\rangle$ state into these target states.

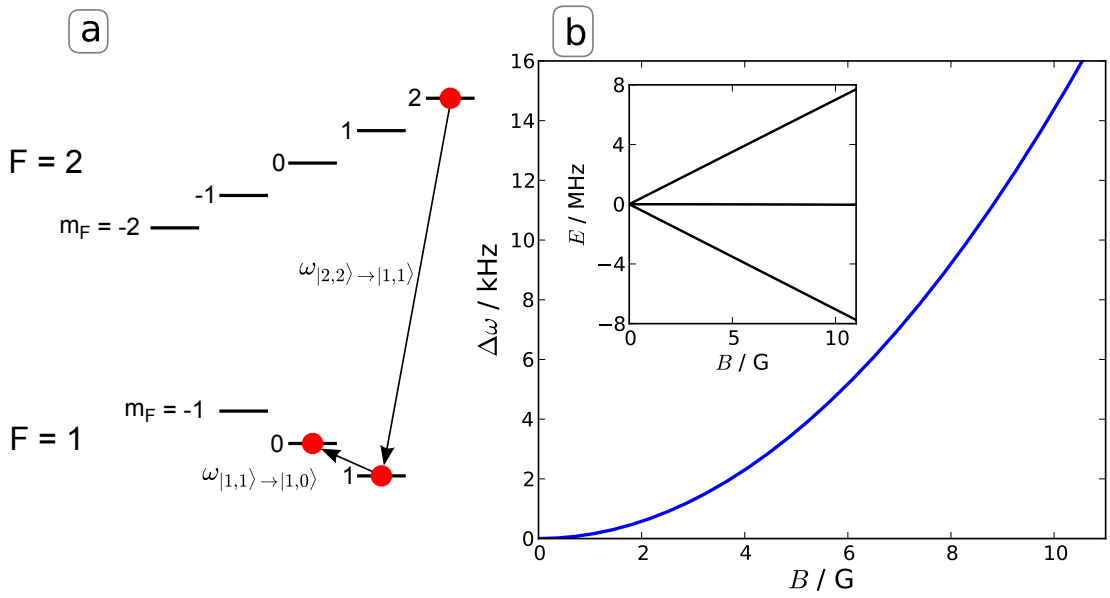

Figure 1.6: Adressing of hyperfine and Zeeman states of Rb. **a)** Level scheme of Rb ground states. The states used in this thesis are marked by red circles. **b)** Non-linear splitting of the Zeeman sublevels of the $F = 1$ hyperfine manifold of Rb. The inset shows the splitting according to Eq. (1.10). In the main graph, the difference $\Delta\omega = \omega_{|1,0\rangle\to|1,1\rangle} - \omega_{|1,0\rangle\to|1,-1\rangle}$ between the two transitions with $F = 1$ is plotted. This difference allows the adressing of a single transition within the hyperfine manifold.

The energy dependence of atoms that experience small magnetic fields can be calculated according to Eq. (1.6) by a simple linear scaling. This is sufficient to model the magnetic trapping potential discussed above. A more precise model is provided by the Breit-Rabi formula [62]

$$E(F, m_F) = \frac{\Delta E_{hf}}{2(2I+1)} + B m_F \mu_B g_N \pm \frac{\Delta E_{hf}}{2}\sqrt{1 + \frac{4m_F}{2I+1}x + x^2} \qquad (1.10)$$

with

$$x = \frac{\mu_B(g_e - g_N)}{\Delta E_{hf}} B. \tag{1.11}$$

Here, ΔE_{hf} is the hyperfine splitting of Rb, g_N and g_e are the nuclear and electronic Landé factors and I is the nuclear spin. The non-linear splitting described by Eq. (1.10) lifts the degeneracy between the different Zeeman sublevels of a hyperfine state.

Fig. 1.6 shows the calculated level shift corresponding to Eq. (1.10) in the range of magnetic fields of up to 10 G. In the inset, the energy shift of all Zeeman sublevels of the lowest Rb hyperfine state $F = 1$ are plotted. The increase in energy is nearly linear and in the range of several MHz. In the $F = 1$ hyperfine state two transitions are possible, $m_F = 0 \rightarrow m'_F = 1$ with transition frequency $\omega_{|1,0\rangle \rightarrow |1,1\rangle}$ and $m_F = 0 \rightarrow m'_F = -1$ with transition frequency $\omega_{|1,0\rangle \rightarrow |1,-1\rangle}$. To drive only one of these transitions, the difference of the frequency $\Delta\omega = \omega_{|1,0\rangle \rightarrow |1,1\rangle} - \omega_{|1,0\rangle \rightarrow |1,-1\rangle}$ caused by the quadratic Zeeman effect needs to be sufficiently large. $\Delta\omega$ is plotted in the main graph of Fig. 1.6, it increases to a value of about 14 kHz at 10 G. This allows the addressing of a single Zeeman sublevel inside the hyperfine manifold, discussed below.

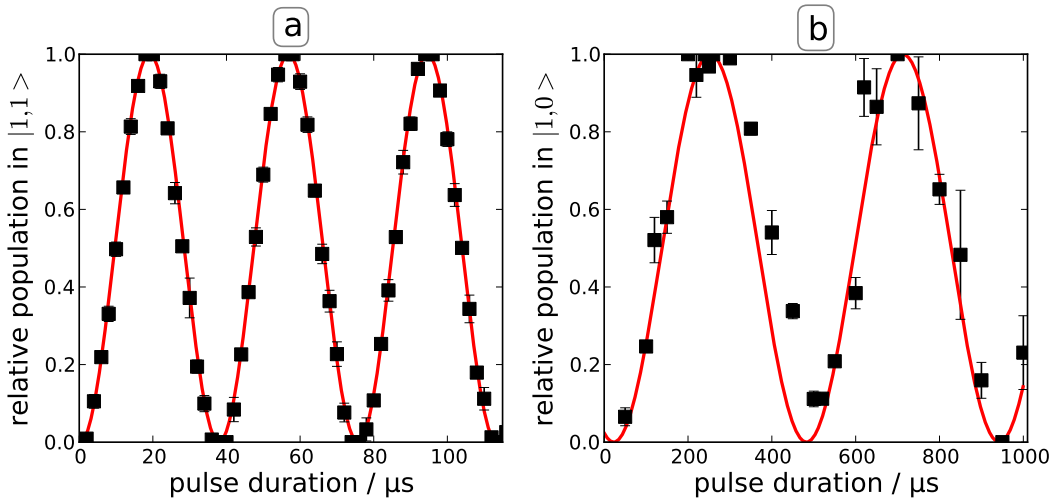

Figure 1.7: Rabi flopping of Rb atoms. **a**) Transition between the two hyperfine states, showing a Rabi frequency of $\omega_{\text{Rabi},|2,2\rangle \rightarrow |1,1\rangle} \approx 2\pi \times 26.5$ kHz. **b**) Transition between two Zeeman sublevels inside the $F = 1$ hyperfine state with $\omega_{\text{Rabi},|1,1\rangle \rightarrow |1,0\rangle} \approx 2\pi \times 3.1$ kHz.

After the guided magnetic transport and the transfer of the sample into the crossed dipole trap, the magnetic trap is switched off suddenly (in less than 1 ms). With a homogeneous offset field of about 10 G applied, a transition between the two hyperfine states of Rb is driven. In this case, the levels are non-degenerate, so that the problem is well described by a two level model. A π-pulse at a frequency around 6.8 GHz transfers the Rb sample from the initial $|2,2\rangle$ state to the the $|1,1\rangle$ state, with a pulse duration of about 19 µs, corresponding to a Rabi frequency of $\omega_{\mathrm{Rabi},|2,2\rangle\rightarrow|1,1\rangle} \approx 2\pi \times 26$ kHz. The population of the different states is determined by a Stern-Gerlach experiment similiar to [63], where a magnetic field gradient is applied to the sample during time-of-flight, separating the states corresponding to their magnetic moment (for details see [58]). Fig. 1.7(a) shows the corresponding Rabi oscillation.

Accordingly, a rf π-pulse around 7 MHz transfers the atoms from the $|1,1\rangle$ state to the $|1,0\rangle$ state. In this case, the pulse duration is about 160 µs, corresponding to a Rabi frequency of $\omega_{\mathrm{Rabi},|1,1\rangle\rightarrow|1,0\rangle} \approx 2\pi \times 3.1$ kHz. The respective experimental data is presented in Fig. 1.7(b). This transition behaves as a two level system due to the non-linear level splitting described above. The efficiency of both transfers is typically better than 95%.

1.4 Conclusion

In this chapter, the necessary techniques to prepare ultracold Rb gases were introduced. Ultracold clouds are produced in a standard magnetic trap. The guided magnetic transport allows to choose the final position of the Rb sample in a range of several hundred µm around the trapping position of the single Cs atoms, without significant degradation in phase-space density. Using microwave and radiofrequency fields, Rb can be transferred into the magnetic field insensitive $|1,0\rangle$ state while being stored in the dipole trap. This enables the use of the magnetic field for the high-gradient MOT to capture single Cs atoms without affecting Rb.

Chapter 2

Single Cs atoms in a species-selective lattice

This chapter deals with the second constituent of the envisioned hybrid system, the neutral impurity atoms. A high-gradient Cs MOT serves as a source for single and few atoms [64–66]. Due to the random loading of atoms from the background gas, the number of atoms captured in the MOT features a Poissonian distribution. In some experiments, the deterministic preparation of a small number of atoms was demonstrated [67–69]. However, we are interested in all atom numbers from one to about ten. This can be achieved by adjusting the Poissonian expectation value of the MOT. By post-selecting experimental shots, experiments with a precisely determined number of atoms can be realized, so that the random loading does not pose any limit in our case.

A MOT is a dissipative trap, atoms scatter photons at a high rate, impeding further cooling and control of the internal state. Furthermore, when interacting with ultracold Rb, interactions are dominated by inelastic light-induced collisions, that lead to a rapid loss of Cs from the trap [58]. For the envisioned experiments, ground state interactions "in the dark" of the impurity atom with the buffer gas are required. Therefore an optical lattice is added, that provides a conservative potential. Furthermore, the trap for Cs has to be compatible with the ultracold Rb sample. This is facilitated by choosing an appropriate wavelength for the optical lattice, that creates a species-selective trapping potential. For the experiments with ultracold Rb, the temperature of the impurity atom needs to be determined. Two different methods to measure the temperature of single Cs atoms in the optical potential of the lattice are presented.

2.1 Experimental setup

In most experiments, MOTs are used as a precooling stage to capture many atoms, with atom numbers in excess of 10^{10}. Two MOTs in this regime are also used in

our experiment for the preparation of Rb. By choosing lower laser intensities and a high magnetic field gradient, the MOT can drastically be altered to trap single and few atoms. The setup of the single Cs atom MOT in our experiment is described in detail in [57, 58, 70–72].

To observe this small amount of atoms, a sensitive detection system is required. The main demand in our case is a reasonably simple setup, compatible with the existing BEC experiment, that is capable to resolve single atoms. This is accomplished by employing a standard high aperture laser collimation objective as first imaging lense. The width of the point-spread function of the complete detection setup is about 7 µm, due to the aberration of the glass cell which is not compensated for [70]. A spatially resolved imaging by a CCD camera would therefore only provide limited information. Consequently, the collected photons are counted by an avalanche photodiode after spectral and spatial filtering. In this way, the exact number of Cs atoms can be counted without gaining spatial information, which is sufficient for all experiments presented in this thesis.

The optical lattice is created by two counterpropagating beams that are focused to a waist of $w_{\mathrm{lattice}} \approx 31$ µm with a maximum power of 100 mW in each beam at a wavelength of $\lambda_{\mathrm{lattice}} = 899.93$ nm. The intensity of each beam is controlled individually by a home-built servo loop of the same type like employed for the running wave dipole trap [57]. In Fig. 1.1, the basic setup of the lattice in our experiment is sketched, details are given in [72].

2.2 MOT as source and detection tool for single Cs atoms

For all experiments throughout this thesis, the high-gradient MOT serves as preparation and detection tool for single Cs atoms.

2.2.1 Source for single Cs atoms

From the detected fluorescence, the number of atoms in the MOT is inferred. Typical time traces and a corresponding histogram of a few hundred shots are presented in Fig. 2.1.

The number of atoms captured into the MOT from the background gas follows a Poissonian distribution (see also Fig. 2.1). This reflects the random loading of background gas atoms. Here, the probability to capture n atoms is given by

$$P_{\bar{N}}(n) = \frac{\bar{N}^n e^{-\bar{N}}}{n!} \tag{2.1}$$

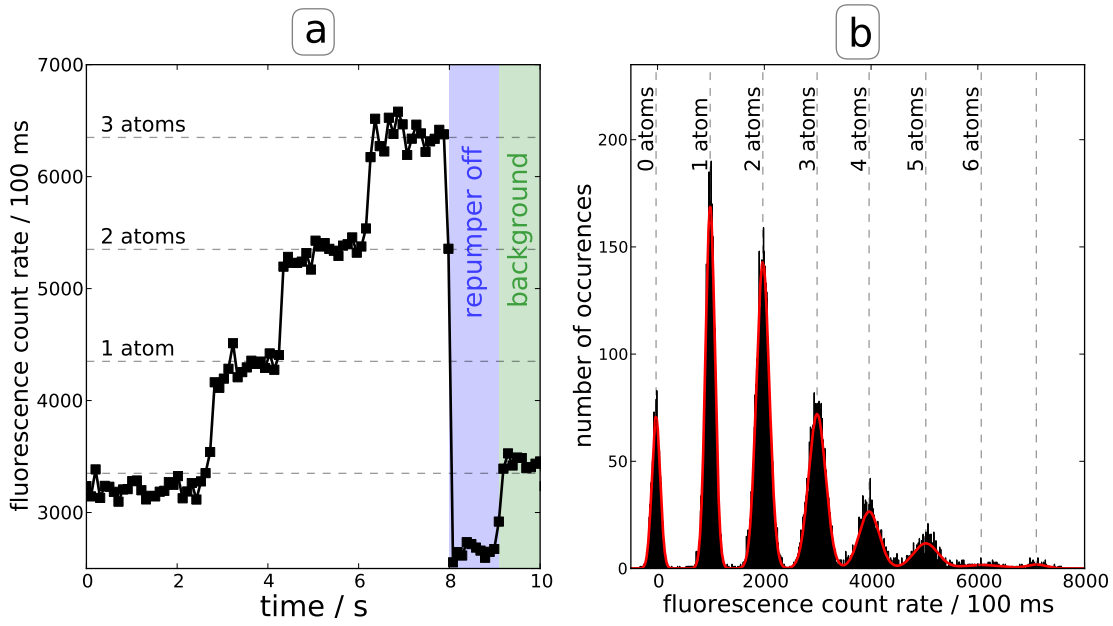

Figure 2.1: Single Cs atom MOT. **a)** Fluorescence of Cs trapped in the MOT, showing distinct steps corresponding to single atoms. **b)** Histogram of a few hundred time traces. The envelope of the histogram is fitted with a Poissonian distribution according to Eq. (2.1).

where $\bar{N}$ is the mean atom number. To adjust the number of loaded Cs atoms, the MOT is operated for a time of typically 150 ms with a lower gradient (typically 60 G/cm). In this way we adjust the Poissonian expectation value $\bar{N}$ of the Cs atom number, typically to a value around two atoms. After this loading stage, the MOT is compressed by ramping up the gradient in a few ms to 300 G/cm, leading to a tighter MOT with a diameter of approximately 30 µm. In this high-gradient MOT, the loading rate is typically below one atom per second. Hence, we keep the number of initially trapped atoms in the MOT for a sufficiently long time to reliably count them.

2.2.2 MOT as detection tool

At the end of each experiment, Cs is recaptured in the high-gradient MOT and the number of remaining Cs atoms is counted. For the recapture, at first the lattice is ramped up. This allows to switch on the magnetic field gradient in the next step, because the lattice provides a sufficiently deep potential to trap atoms also in high field seeking states, that experience a repulsive potential due to the magnetic field gradient. Finally, the MOT lasers are switched on, the lattice is extinguished and the fluorescence of the atoms is detected to determine the atom number. Switching

on the MOT lasers after applying the magnetic gradient ensures that the probability to load atoms from the background gas during recapture is smaller than one percent and can be neglected.

Bayes analysis of fluorescence data

For suffieciently long binning times and low atom numbers, the distinctive peaks corresponding to single atoms are well separated in the histogram. In these cases, a simple threshold analysis can be used to deduce the atom number from the observed fluorescence, as is evident in the data presented in Fig. 2.1(b).

For some experiments, however, it is advantageous to be able to determine the atom number with a shorter binning time. Furthermore, the noise increases for higher absolute photon counts due to shot noise [57], which leads to a broadening of the peaks corresponding to higher atom numbers. Both effects cause a gradual overlap of the peaks, impeding a simple threshold analysis.

Therefore, alternatively a Bayesian approach based on inductive reasoning is employed [73]. The quantity of interest is the posterior probability $p(H|D)$, the probability that the hypothesis H is true, under the condition that the experiment yielded the data D. Usually, the likelihood function $p(D|H)$, the probability of observing the data D when the hypothesis H is true, can be assigned in an experiment. Bayes theorem relates these conditional probabilities. It can be written as

$$p(H|D) \propto p(D|H) \times p(H) \tag{2.2}$$

where $p(H)$ is the prior probability, reflecting the initial knowledge of the hypothesis.

This reasoning can be applied to our case. The fluorescence traces consists of discrete, binned time intervals (see Fig. 2.1(a)). Initially, the probability for each atom number that occurs in the histogram is set equal, since we do not have any information yet. In the next time intervall, we gain information in the form of the number of counted photons. With the corresponding histogram (see Fig. 2.1(b)), the likelihood function $p(D|H)$ can be calculated, the probability to observe a number of photons given a certain atom number. With Bayes theorem, the posterior probability $p(H|D)$ is calculated, yielding the probability for each atom number.

The resulting posterior probability is used in the next time step as prior probability, reflecting the increased knowledge about the atom number. Additionally, the independently measured loading and loss rates of atoms in the MOT can be included in the analysis. This adjusts the "willingness" of the algorithm to detect loading or loss events. Finally, with the photon number measured in the next binning interval,

the new posterior probability is calculated. This is repeated for the complete fluorescence trace. The result is a time trace, where a probability is assigned to each atom number. Therefore the most probable atom number is known, along with a measure for the confidence. In our case, one certain atom number typically has a probability close to unity, so that the Bayes algorithm works very reliably.

With the methods introduced, single atoms can be prepared, recaptured and detected in the MOT. This is the prerequisite to perform experiments in the conservative lattice potential, described in the following.

2.3 Species-selective optical lattice

The lattice potential has to be sufficiently deep to load a laser cooled Cs atom directly from the MOT. At the same time, the lattice should be reasonably shallow for Rb, to facilitate the adiabatic loading of ultracold Rb and to keep the density as low as possible to prevent high collisional losses. In addition, the limited laser power has to be taken into account. To fulfill these requirements, the employed Ti:Sa laser is tuned to 899.93 nm, which is roughly 5 nm to the red of the D1-transition of Cs at about 894.59 nm [74]. This leads to a relatively high off-resonant photon-scattering which limits the lifetime of the spin polarization, discussed in detail below. Accordingly, the lattice creates a significantly shallower potential for Rb than for Cs.

2.3.1 Optical lattice parameter

In an optical lattice, two counterpropagating beams create an interference pattern with a periodicity of $\lambda/2$. The corresponding intensity can be described by

$$I(x, y, z) = I_0 \cos^2(kz) \exp(-2(x^2 + y^2)/w_{\text{lattice}}^2) \tag{2.3}$$

where k is the wavevector of the lattice. From this intensity, the corresponding potentials for Rb and Cs are calculated.

Like in the case of the running wave dipole trap, the detuning is large compared to the hyperfine and Zeeman splitting. Therefore it is sufficient to sum over the contributions of the D1 and D2 line. In Table 2.1 the trap parameters obtained with Eq. (1.7) and Eq. (1.8) are listed. As intended, the trap depth for Rb is significantly lower than for Cs, the difference is about one order of magnitude.

These parameters are theoretical and do not take into account experimental imperfections and uncertainties of the initial beam characteristics. In the following, the trap is characterized experimentally, providing a way to check these parameters.

λ_{lattice}	899.93 nm
w_{lattice}	31 µm
z_{lattice}	3 mm
$P_{\text{max,lattice}}$	100 mW
$I_{\text{max,lattice}}$	0.27×10^9 W / m^2

Cs		Rb	
Γ_{Cs}	426 s^{-1}	Γ_{Rb}	1.8s $^{-1}$
$U_{0,\text{Cs}}$	900 µK	$U_{0,\text{Rb}}$	84 µK

Table 2.1: Beam parameters of the optical lattice and deduced properties of the corresponding potential.

2.3.2 Typical sequence and statistical uncertainty

Before starting with the experimental characterization of the lattice, some essential experimental techniques are introduced in the following. A typical sequence starts with the preparation of a precisely known number of Cs atoms in the MOT. Subsequently, the atoms are transferred to the lattice, the efficiency of this transfer is close to unity. The MOT is switched off and an experiment is performed with the atom stored in the conservative potential in the dark. Because of the low atom number, the probability to load two atoms into the same potential well can be neglected, so that each individual atom is stored in an isolated well of the lattice. In a typical experiment, the quantity to be measured (e.g. trap frequency, lifetime, ...) is mapped onto the survival probability of the Cs atom. Finally, the remaining atoms are recaptured in the MOT and counted. In Fig. 2.2 a basic sequence is presented.

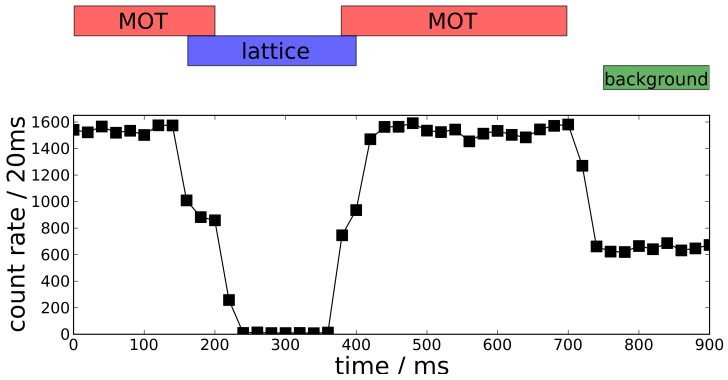

Figure 2.2: Typical sequence. Single or few Cs atoms are trapped in the MOT and transferred to the lattice. Cs is stored in the optical lattice "in the dark" and then recaptured in the MOT.

For a single atom, the outcome is either the survival or the loss of the atom. The statistical uncertainty for an experimentally determined survival probability $p = m/N$ with N trials with single atoms and, correspondingly, m surviving atoms, is given by a binomial distribution

$$P(N, m, p) = p^m (1-p)^{N-m} \frac{N!}{m!(N-m)!}. \tag{2.4}$$

From this relation the confidence intervals are calculated. A detailed derivation can be found in the PhD thesis of Stefan Kuhr [75]. In general, the derived errors are asymmetric. For all single atom survival probability measurements throughout this thesis, the statistical uncertainty is given within this framework, unless stated otherwise.

Adiabatic lowering of the optical lattice

For most experiments with single Cs atoms in the lattice, the potential depth is lowered adiabatically. For the criteria for adiabaticity, the reasoning in the thesis of Wolfgang Alt is followed [76]. The waveform used is given by

$$U(t) = \begin{cases} U_0 & \text{for} \quad t \leq t_0 \\ U_0 \left(1 - \frac{t^2}{4T_c^2}\right) & \text{for} \quad 0 < t \leq T_c\sqrt{2} \\ U_0 \frac{T_c^2}{t^2} & \text{for} \quad t > T_c\sqrt{2} \end{cases}$$

where U_0 is the initial potential depth and T_c is the time constant for the waveform.

The radial motion of atoms in the trap defines the characteristic timescale, given by the radial trap frequency of $\omega_r \approx 2$ kHz (see section 2.3.3). The characteristic timescale is therefore set to $T_c = 5$ ms to fulfill the criteria for adiabaticity. This also defines the duration of the ramp; lowering the trap to 1% of the initial trap depth takes 50 ms. In Fig. 2.3 the lowering of the potential with a duration of 50 ms is plotted.

2.3.3 Trap frequencies

The characterization of the lattice potential starts with the determination of the trap frequencies. The axial ω_z and radial ω_r trap frequencies are given by

$$\omega_z = 2\pi \sqrt{\frac{2U_0}{m_{Cs}\lambda_{lattice}}} \tag{2.5}$$

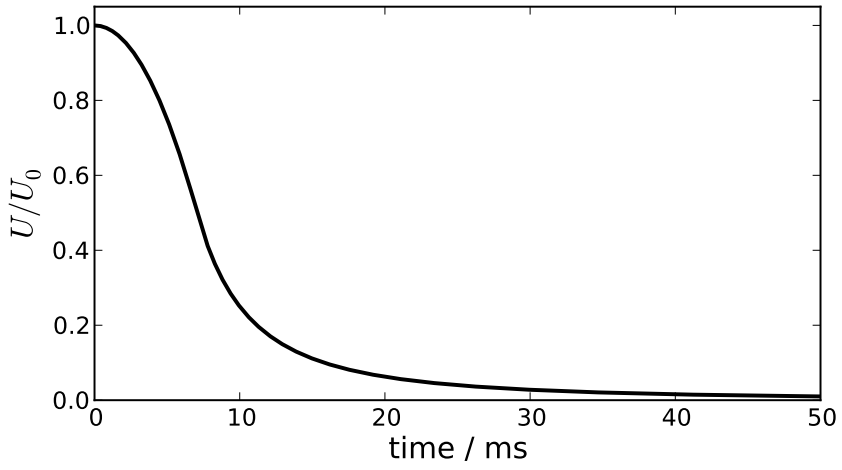

Figure 2.3: Adiabatic lowering of a potential to 1% of the initial trap depth, according to the waveform described in the text.

and

$$\omega_\mathrm{r} = \sqrt{\frac{4U_0}{m_\mathrm{Cs} w_\mathrm{lattice}^2}} \tag{2.6}$$

where λ_lattice is the wavelength and w_lattice the waist of the lattice beams. With the potential depth $U_0 = 900$ µK, this yields theoretical values of $\omega_\mathrm{r} = 2.3$ kHz for the radial trap frequency and $\omega_\mathrm{z} = 345$ kHz for the axial trap frequency for Cs atoms.

To compare this calculated values with the realization in the experiment, the trap frequencies are measured. For this, the trap intensity is modulated for 200 ms with an amplitude of typically 20% of the total trap depth. Then the trap is adiabatically lowered to about half the initial trap depth to allow heated atoms to escape. This transforms the determination of the survival probability to a temperature measurement in the framework of adiabatic lowering (as discussed below in section 2.4.1). This leads to a much higher sensitivity, like discussed above for Rb, see section 1.2.3. Finally, the number of surviving atoms is measured.

The result is shown in Fig. 2.4. For the radial trap frequency, two loss dips are observed. The dip at about 2 kHz probably corresponds to resonant heating. However, it only consists of a single data point, so that the it cannot be employed for a reasonable analysis and is therefore ignored. Instead, the radial trap frequency is determined from the second dip at $\omega_\mathrm{r,parametric} = (4.2 \pm 0.1)$ kHz, that corresponds to parametric heating, to be $\omega_\mathrm{r} = (2.1 \pm 0.1)$ kHz. The axial frequency is determined from the fit of Fig. 2.4 to be $\omega_\mathrm{z} = (311 \pm 1)$ kHz. Both radial and axial frequency

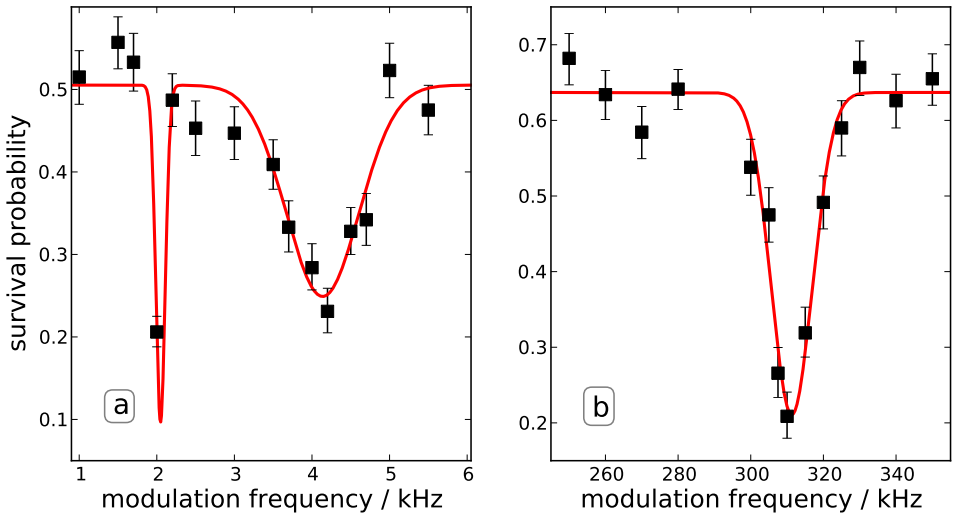

Figure 2.4: Measurement of trap frequencies of Cs stored in the lattice. When the modulation frequency is resonant to the parametric excitation frequency, the atoms are heated out of the trap. **a)** Radial trap frequency. **b)** Axial trap frequency.

are found to be reduced by about 10% compared to the theoretical expected values. The deviation can be explained by experimental imperfections like aberrations in the focusing optics, limited aperture of the optics that leads to diffraction and thus reduced intensity in the focus, and loss of intensity by reflection off the glass cell. Since both radial and axial trap frequencies are lower by the same factor, a possible loss in contrast due to polarization impurity seems not to play a role here. For the analysis in the rest of this thesis, the trap parameters deduced from the measured trap frequencies are used. The resulting trap depth is therefore $U_{\text{lattice}} \approx 720$ µK, since $\omega \propto \sqrt{U}$ (see Eq. 2.4).

2.3.4 Off-resonant photon scattering rate

The disadvantage of the high selectivity of the lattice for Cs compared to Rb is a small detuning of only 5.3 nm to the Cs D1-line. This causes a relatively high off-resonant scattering rate of lattice photons. This scattering consists of elastic Rayleigh scattering ($F = F'$) and inelastic Raman scattering ($F \neq F'$). Both processes transfer energy to the atom (see section 2.3.5); Raman scattering events in addition change the (hyperfine and Zeeman) state of the atom. This limits the time scale on which manipulations of the internal degree of freedom are possible with the atom stored in the lattice.

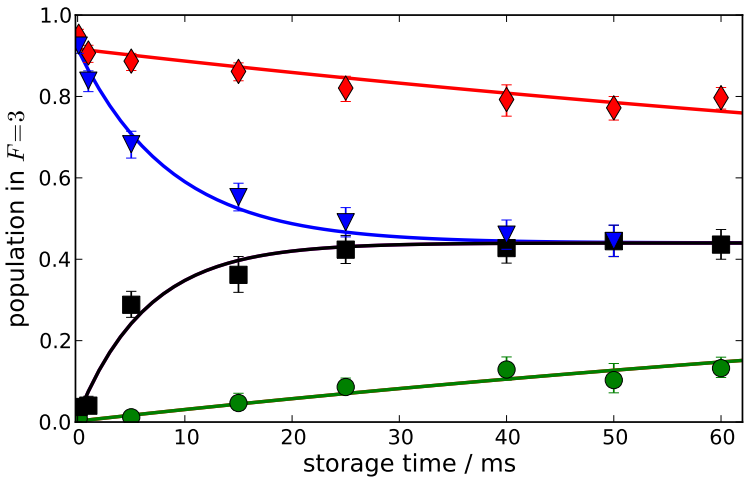

Figure 2.5: Decay of the spin polarization due to off-resonant photon scattering, for both hyperfine states and different lattice intensities. At full lattice intensity, the spin polarization is lost within a few ms (▼: $F = 3$, $P_{\text{lattice}} = 100$ mW and ■: $F = 4$, $P_{\text{lattice}} = 100$ mW). For lower lattice intensity, the decay is accordingly slower (♦: $F = 3$, $P_{\text{lattice}} = 8$ mW and ●: $F = 4$, $P_{\text{lattice}} = 8$ mW).

When loaded from the MOT, the Cs atoms have arbitrary F and m_{F} quantum numbers. A simple way to control the hyperfine state is to leave on the repumper (cooler) of the MOT laser, thereby pumping the Cs atom into the $F = 4$ state ($F = 3$ state).

In order to determine the hyperfine state, a Stern-Gerlach type experiment, as applied for ultracold Rb clouds in this thesis, is not suitable because time-of-flight imaging is not possible. Instead, a (hyperfine) state-selective push out is used [75, 77]. For this purpose, a laser is locked to the $F = 4 \rightarrow F' = 5$ transition. This transition is nearly closed, so that enough photons are scattered before the atom is transferred into the $F = 3$ state. By using a sufficiently high intensity, the atoms are pushed out of the trap in less than one oscillation period. This ensures that the push out mechanism relies on the transfer of momentum, rather than energy. In this way, a good selectivity close to unity is achieved.

To quantify the off-resonant photon scattering of the Cs atoms by the lattice light, the decay of the spin polarization of the Cs atoms is measured. For this Cs is loaded into the lattice and subsequently the lattice depth is lowered adiabatically to the desired value. The atoms are then optically pumped either into the $F = 3$ or the $F = 4$ state. After a variable storage time, the push out laser is applied to the sample, removing atoms in the $F = 4$ state. Finally, the fraction of atoms in the $F = 3$ state is determined.

In Fig. 2.5 the experimental results are presented. At maximum lattice intensity ($P_{\text{lattice}} = 100$ mW), atoms initially prepared in the $F = 3$ state decay into an equal spin mixture with a time constant of (8.6 ± 1.1) ms. Correspondingly, atoms initially prepared in $F = 4$, decay within (6.5 ± 1.3) ms. For a lower lattice power of $P_{\text{lattice}} = 8$ mW, the time constants are determined to be (155 ± 26) ms for the $F = 3$ state and (149 ± 19) ms for the $F = 4$ state.

From the calculated scattering rate at full lattice power, an off-resonant photon scattering rate, including both Raman and Rayleigh scattering, of about 340 s^{-1} is expected. The Raman scattering is reduced by a factor that depends on the wavelength [78]. The measured decay time on the order of 100 – 200 s^{-1} seems to be in agreement with the expectation. The scaling of the decay rate should scale linearly with the lattice power. This is also roughly confirmed by the measured time constants for $P_{\text{lattice}} = 8$ mW.

2.3.5 Lifetime

To determine the lifetime of an atom stored in the lattice experimentally, Cs is loaded into the lattice and stored for varied time intervals. After the storage time, the remaining atoms are counted. Fig. 2.6 shows the result. With a time constant of about 6 seconds, atoms are lost from the trap.

The lifetime of a Cs atom stored in the lattice is given by several fundamental and technical loss and heating processes. A fundamental loss mechanism are collisions with high temperature background gas atoms, that lead to an immediate loss of atoms from the trap. However, at the UHV conditions (pressure of about 10^{-11} mbar) in our apparatus, the lifetime due to these collisions was measured to be about 160 s for Rb stored in the magnetic trap and can be completely neglected here.

The dominant fundamental loss process in the lattice is the recoil heating of atoms out of the trap due to off-resonant photon scattering from the lattice beams. Each scattered photon increases the energy of the atom by twice the recoil energy

$$E_{\text{rec}} = \frac{\hbar^2 k^2}{2m_{\text{Cs}}} \tag{2.7}$$

where k is the wavevector of the lattice laser. Assuming the total photon scattering rate to be $\Gamma_{\text{Cs}} \approx 340$ s^{-1}, the heating rate P_{heat} can be calculated [61, 79] from this

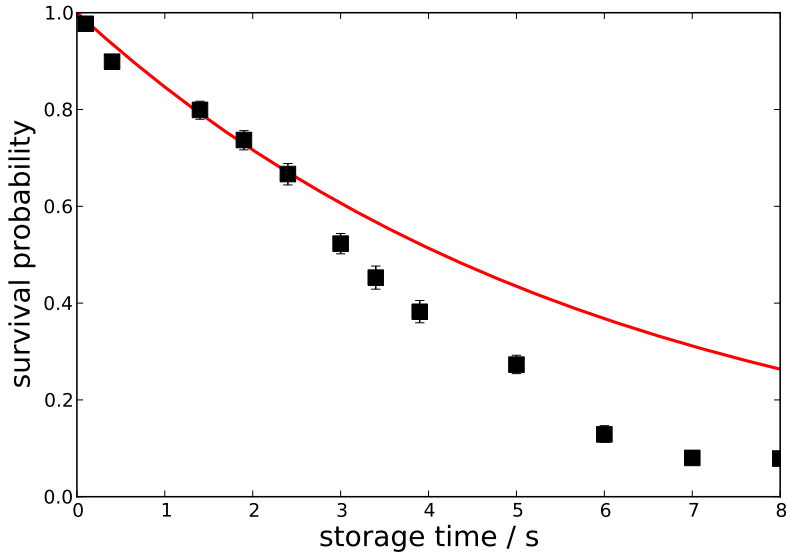

Figure 2.6: Lifetime of single Cs atoms stored in the lattice at full intensity ($P_{\text{lattice}} = 100$ mW). The red line indicates the expected loss rate due to heating by lattice photons.

to be

$$P_{\text{heat}} = 2E_{\text{rec}}\Gamma_{\text{Cs}}. \tag{2.8}$$

In our case the recoil energy amounts to $E_{\text{recoil}} = 89$ nK, yielding a heating rate of 76 µKs^{-1} at full lattice power ($P = 100$ mW). The lifetime τ_{lattice} of the atoms due to recoil heating is hence given by

$$\tau_{\text{lattice}} = \frac{U_{\text{lattice}}}{2P_{\text{heat}}} \tag{2.9}$$

where U_{lattice} is the depth of the lattice potential for Cs [79]. Assuming $U_{\text{lattice}} = 720$ µK, the time constant for the lifetime equals to $\tau = 6.0$ s. A plot of an exponential decay with this time constant presented in Fig. 2.6, along with the experimental data shows a reasonable agreement for small storage times ($t \leq 3$ s). For longer times, however, a faster, non-exponential loss is observed, pointing to an additional heating mechanism.

A technical source of heating in the trap is optical phase noise, caused by electronic phase noise of the driving electronics of the acousto-optical modulators used for power stabilization. Any relative shift of the phase of the two lattice beams leads

to fluctuations of the position of the lattice potential wells. This can lead to rather high heating rates on the order of several hundred μKs^{-1} [76]. To avoid any phase noise in our setup, the rf driving signal for the acousto-optical modulators is derived from the same voltage-controlled oscillator. Hence, phase noise should not play a role in our setup.

Since all experiments in the lattice take only few tens of milliseconds, the photon scattering does not limit the survival probability of Cs. The relatively high heating rate of 76 μKs^{-1} holds for full lattice power. For most experiments, the lattice is ramped down adiabatically directly after the transfer of the atom from the MOT within milliseconds to a few percent. The heating rate is proportional to the scattering rate which is proportional to the lattice intensity. Thus the overall heating in the lattice in a typical experiment can be estimated to be below 1 µK. This has to be compared to the temperature of the atom when loaded from the MOT of about 30 µK, see next section. Hence, the heating is on the order of a few percent and can be neglected here.

2.4 Temperature measurements of single atoms

Time-of-flight velocimetry with absorption imaging is a standard tool of cold atom experiments and is also used in this experiment with ultracold Rb gases. For single atoms, it cannot be applied since absorption imaging is not possible. Employing fluorescence imaging, the temperature of single atoms has been obtained from time-of-flight measurements [80]. However, this approach needs an inappropriate technical effort for our purpose. Techniques relying on microwave spectroscopy require the motional sidebands to be resolvable [81]. In the lattice, this is possible only in the axial degree of freedom with a trap frequency of hundreds of kHz. For the interaction experiments with Rb in chapter 4, both species are stored in a running wave trap with trap frequencies of few hundred Hz, which impedes the use of this technique.

Instead, two simple methods that rely on the thermal distribution in the trap are applied here. In the first method, the trap depth is lowered adiabatically. From the survival probability for different trap depth at the end of the lowering, the thermal distribution of the atoms can be inferred. This technique was employed in our group earlier [76]. In a second approach, the trap is switched off non-adiabatically for a short time Δt, allowing hotter atoms to escape with higher probability. The survival probability in dependence on the release time Δt can be analyzed to extract the temperature. This method is particularly useful for lower temperatures, as will be discussed in the following.

2.4.1 Adiabatic lowering

The basic adiabatic lowering experiment is illustrated in Fig. 2.7. An atom with initial energy E_0 is prepared in the trap (Fig. 2.7(a)). Then, the trap is lowered adiabatically (Fig. 2.7(b)). During the adiabatic lowering, the initial energy E_0 of the atom is lowered, the conserved quantity here is the action. The energy $E(t)$ of the atom decreases more slowly than the trap depth $U(t)$, causing the atom to leave the potential at some finite escape energy U_{esc} (Fig. 2.7(c)).

The atoms in the trap have a thermal distribution, so that the initial energy E_0 for each atom is different. The survival probability for an ensemble of single atoms for a certain, fixed lowered energy U_{low} determines the fraction of atoms above a certain level of initial energy E_0. Hence, the measurement of the survival probabilities in dependence on the lowered energy U_{low} allows to extract the temperature and, furthermore, the energy distribution of the atoms, providing a consistency check for this technique. Additionally, the energy distribution needs to be known to model the release and recapture technique, discussed later in this section.

Theory and simulation of adiabatic lowering

For a quantitative analysis, the escape energy U_{esc} has to be connected to the initial energy E_0 of the atom in the trap. To model the adiabatic lowering, the equations of motion have to be solved for atoms in the lattice potential. The lattice potential is given by

$$V(x,y,z,t) = U_{\mathrm{lattice}}(t)\cos^2(kz)\exp(-2(x^2+y^2)/w_{\mathrm{lattice}}^2) + m_{\mathrm{Cs}}gx \tag{2.10}$$

where $U_{\mathrm{lattice}}(t)$ is the time-dependent potential depth and w_{lattice} the waist of the lattice. There is no analytic solution for the equations of motion given by this potential. The treatment within a harmonic approximation is not sufficient, since the atom experiences the full volume of the trap during the lowering sequence. Gravity plays an important role especially for low traps and needs to be included. The trajectories of the atom are therefore in general strongly non-harmonic. Additionally, gravity leads to a coupling of the perpendicular degrees of freedom. To obtain realistic trajectories of the atoms in this potential, the equations of motion where numerically solved. For all simulations in this thesis, the `scipy` and `numpy` libraries of `python` are employed [82, 83].

The general approach of the simulation follows the steps taken in [76]. First the initial energy E_0 of the atom is fixed. Then this energy is randomly distributed among the three degrees of freedom. Now the equation of motion for one degree

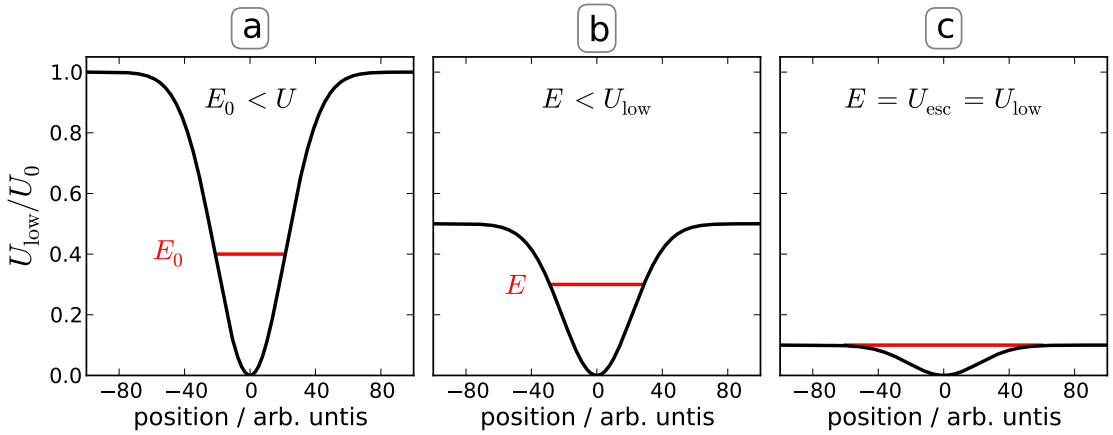

Figure 2.7: Adiabatic lowering of a potential. **a)** Initially, the atom is stored in the potential with an energy E_0. **b)** The energy of the trapped atom E decreases more slowly than the potential depth U of the potential. **c)** At some potential depth U_{esc} the energy of the atom equals the potential depth and the atom escapes.

of freedom is integrated for a random fraction of the one-dimensional oscillation. By this means one-dimensional spatial coordinates and velocities are generated, combining these gives a set of three-dimensional phase-space coordinates. Since the potentials are non-linear, this can lead to a slightly different energy. To compensate for this, the atom is slightly moved in the three-dimensional potential towards the center (away from the center) and the velocities are slightly decreased (increased) in order to decrease (increase) its energy. In this way, the energy is adjusted to a precision of better then 0.1% of the initial value. Overall this approach ensures that the phase-space for the initial conditions is populated equally.

With these initial conditions the three-dimensional equations of motion given by Eq. (2.10) are integrated for a given time interval, in this case on the order of several ten ms. During this evolution, the potential is ramped down according to Eq. (2.3) to a value U_{low}. The trap depth is then held constant at U_{low} for 20 ms, to allow the atom to escape from the recapture region of the MOT. After this, the distance of the atom to the center (MOT-position) is measured. If this distance is more than 100 µm, the atom is counted as lost.

This procedure is repeated at least 200 times for a given E_0, such that the statistic uncertainty is reasonably small. The result of a run for a given E_0 is the evolution of surviving probability with the lowered trap depth U_{low} at the end of the lowering. For a quantitative determination of the escape energy U_{esc} and the energy selectivity ΔU_{esc} from this data, the decay of the survival probability around U_{esc} is fitted with

an error function

$$\mathrm{erf}(U_{\mathrm{low}}) = \frac{2}{\sqrt{\pi}} \int \exp\left(-\frac{(U_{\mathrm{low}} - U_{\mathrm{esc}})}{\Delta U_{\mathrm{esc}}}\right) dx. \tag{2.11}$$

In this way, for each initial energy E_0 the escape energy U_{esc} and the energy selectivity ΔU_{esc} is found. The final result of the simulation of adiabatic lowering is shown in Fig. 2.8. The data points indicate the escape energy U_{esc}, the bars correspond to the energy selectivity ΔU_{esc}.

For an experimentally measured escape energy U_{esc}, the initial energy of the atom in the trap E_0 can now be inferred. For this purpose, an empirical function of the form

$$E_0(U_{\mathrm{esc}}) = a\sqrt{(U_{\mathrm{esc}} - b)} - c - dU_{\mathrm{esc}} - eU_{\mathrm{esc}}^2 - fU_{\mathrm{esc}}^3 \tag{2.12}$$

is fitted to the simulated data. With the obtained parameters, the experimental data is scaled to extract the temperature.

Experimental results of adiabatic lowering

The experiment contains the same steps discussed above for the theoretical modeling. Cs is prepared in the lattice at full power, subsequently the lattice is lowered adiabatically to a value between 0.5% - 8% of the initial trap depth. The remaining number of atoms is counted.

The result of this measurement is shown in Fig. 2.9. At trap depths U_{low} below about 4%, the atoms start to leave the trap. The total transfer efficiency is about 97% in this measurement. By scaling this data according to Eq. (2.12) with the parameters obtained by the simulation, the energy distribution is calculated. It is shown in Fig. 2.10. To extract a temperature, a Maxwell-Boltzmann distribution of the form

$$p_{\mathrm{MB}}(\vec{v}) = (m_{\mathrm{Cs}}/2\pi k_{\mathrm{B}}T)^{\frac{3}{2}} \vec{v}^{\,2} \exp(-m_{\mathrm{Cs}}\vec{v}^{\,2}/2k_{\mathrm{B}}T) \tag{2.13}$$

is assumed. The cumulative probability distribution according to Eq. (2.13) is used to fit the data, the fitted function is shown in Fig. 2.10. The agreement between experimental data and the fit is reasonable. Additionally, in Fig. 2.10 the corresponing probability density for the data is shown. The fit yields a temperature of 27 µK, where the error is estimated by the uncertainties of the trap parameters to be about 20%. The measured temperature is considerably below the Doppler

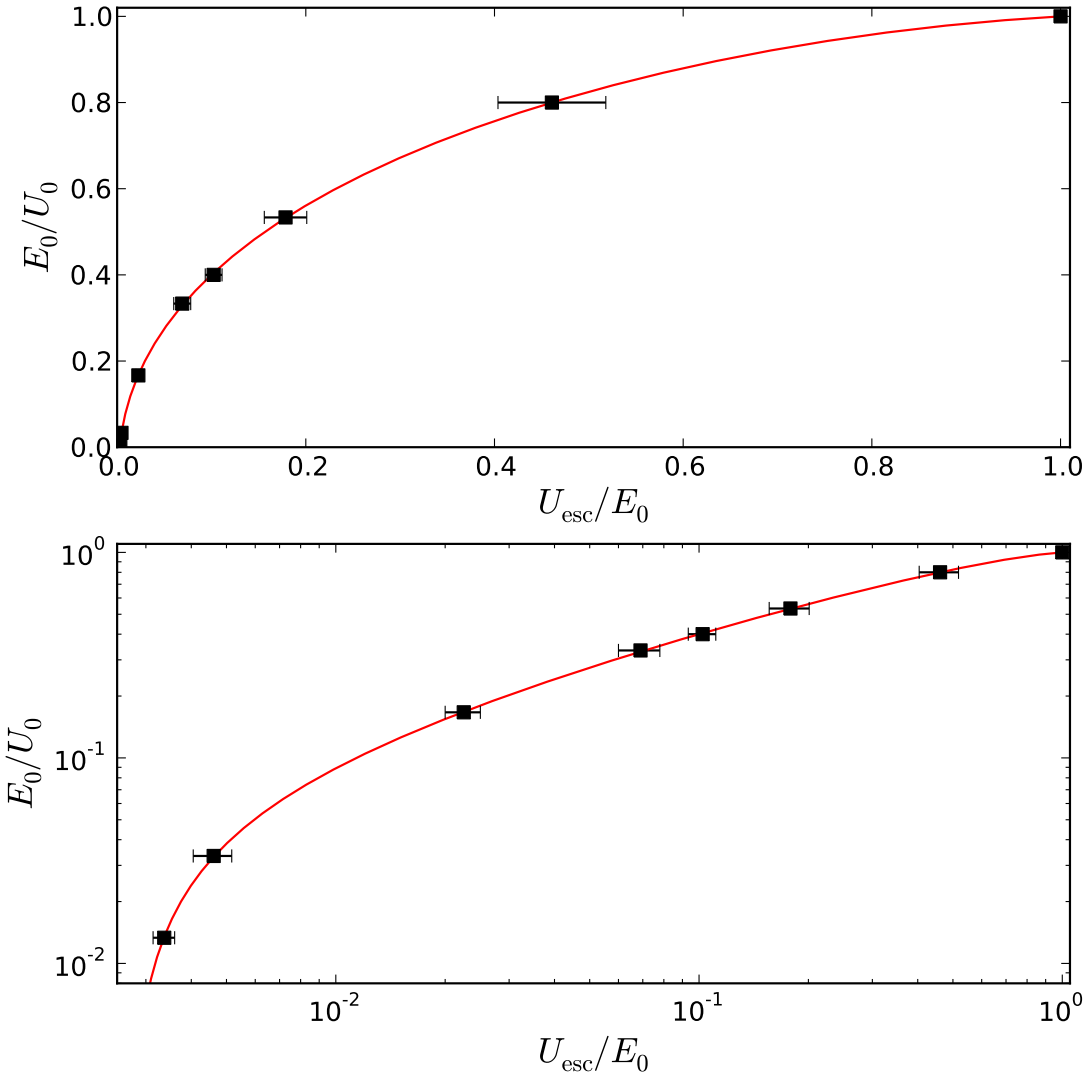

Figure 2.8: Initial energy of the atom E_0 versus escape energy U_{esc} obtained from the simulation, in linear scale (upper panel) and logarithmic scale (lower panel). An atom with an initial energy E_0 of for example 0.8 U_0 will escape from the potential at lower potential depth, in this case approximately 0.5 U_0. The experimentally determined entity is the escape energy U_{esc}, that can be translated into the initial energy of the atom E_0 by the fit with an empirical function given by Eq. (2.12) (red line). For details see text.

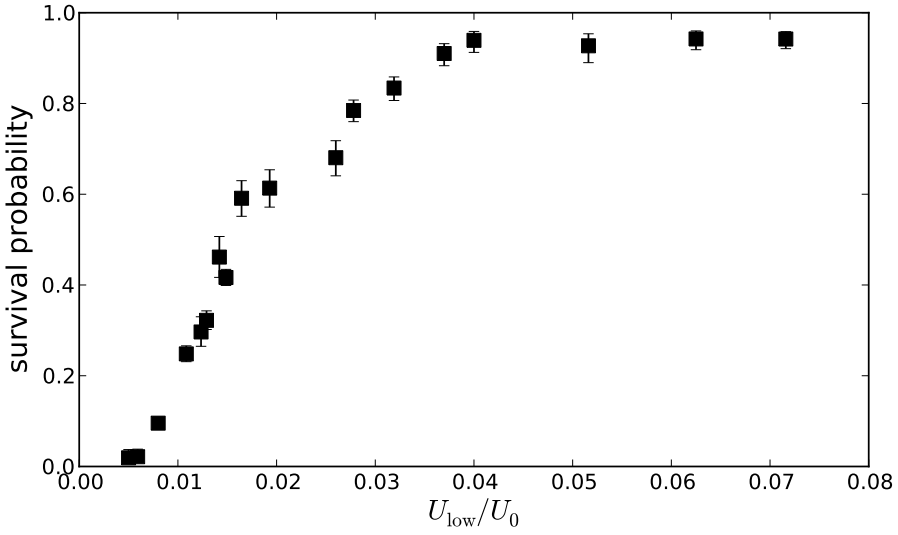

Figure 2.9: Survival probability of single atoms in the lattice versus reduced trap depth U_{low} at the end of adiabatic lowering.

limit of 125 µK, indicating sub-doppler cooling in the MOT during transfer. This temperature is comparable to the results of another experiment in our own group [76] and with experiments performed in the group of P. Grangier with single Rb atoms [84]. Furthermore, the atoms are observed to obey a Maxwell-Boltzmann energy distribution.

The disadvantage of the technique of adiabatic lowering is the low sensitivity for colder atoms as for instance prepared by sympathetic cooling of Cs in ultracold Rb in chapter 4. This can be seen in Fig. 2.8. For lower initial energies E_0, the slope of the empirical fit function becomes steeper, such that a small error in the measured escape energy causes a drastic change in the extracted initial energy of the atom. Furthermore, for smaller trap depth, gravity plays an increasingly important role and can lead to deviations that are not reflected by the simulation, as for example a non-perfect perpendicular alignment of the trap with respect to gravity. For lower temperatures the release and recapture technique is a good alternative, as discussed in the next section.

2.4.2 Release and recapture

The release and recapture technique is one of the most basic and earliest temperature measurements performed with cold atoms [59]. The basic idea is shown in Fig. 2.11. The trap is switched off in a non-adiabatic way. The atoms experience a short time

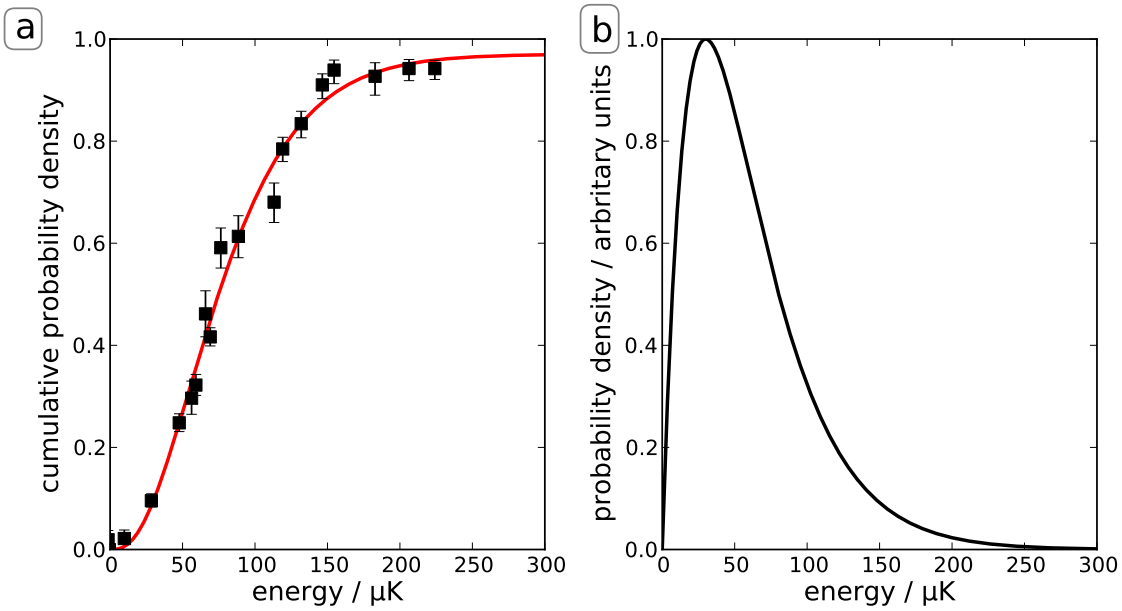

Figure 2.10: Energy distribution of single atoms measured by the adiabatic lowering of the potential. **a)** Cumulative energy distribution, yielding a temperature of $T = 27$ µK. **b)** Corresponding probability density.

of free expansion Δt, after which the trap is switched on, again in a non-adiabatic way. The probability to recapture an atom in the trap is the higher, the lower the kinetic energy was.

The criterion for a non-adiabatic extinguishing of the lattice light is again (like the criterion for adiabaticity in section 2.3.2) determined by the trapping frequencies. Due to the limited bandwidth of the power stabilization servo loop of at most 100 kHz, switching off the lattice takes a finite time. Therefore the trap is switched off in a non-adiabatic way for the two radial degrees of freedom ($\omega_{\mathrm{radial}} \approx 2$ kHz), but for the axial degree of freedom any switching using the servo loop is an adiabatic process ($\omega_{\mathrm{axial}} \approx 311$ kHz). In the simulation introduced in the following, this is modeled by an exponential decay with a time constant $\tau = 13$ µs, that was measured experimentally for the specific experimental parameters.

In order to extract a temperature from the experimental data, a realistic simulation is necessary. The trap potential is again given by Eq. (2.10). The aim of the simulation is now to reproduce a release and recapture experiment for a given temperature of the atom. This is done for a set of different temperatures. Then, for an experimental data set, the simulation with the least squared deviation is determined to find the best estimate of the temperature.

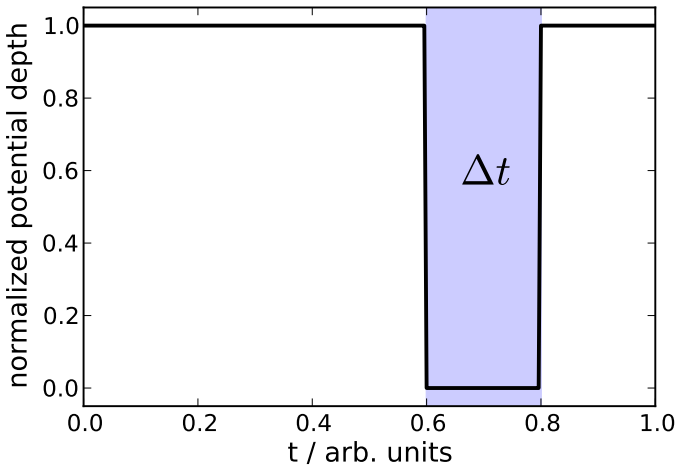

Figure 2.11: Schematic release and recapture sequence. The potential is switched off non-adiabatically. For a time Δt the atomic sample is allowed to expand freely. Then the trap is switched on non-adiabatically and the number of surviving atoms is counted.

Since it is now the temperature of the atom that is fixed, and not the energy like in the simulation of the adiabatic lowering, an energy distribution has to be assumed. From the adiabatic lowering this distribution is known to be well described by a Maxwell-Boltzmann distribution. Therefore, for a given temperature the initial energy of the atom is randomly chosen with a Maxwell-Boltzmann probability function given by Eq. (2.13). In Fig. 2.12 the resulting energy distribution for one typical simulation run consisting of 2000 shots is shown.

For a certain energy in one shot, a random position and kinetic energy in the potential are chosen, along the lines of the simulation of the adiabatic lowering. The equations of motion are then integrated numerically to determine the trajectory of the atom, with the release and recapture sequence (see Fig. 2.11) included into the simulation after a certain time. Finally, the distance of the atom to the MOT position is calculated. If the atom has departed more than 100 µm from the MOT, the atom is count as lost. For each temperature, the release time is varied to reproduce a complete experimental run.

Experimental results

The experimental run consists of the same steps like discussed for the simulation. Few Cs atoms are transferred into the lattice, the trap is switched off for a time Δt between 0 – 3 ms, and the remaining fraction of atoms is determined. For each

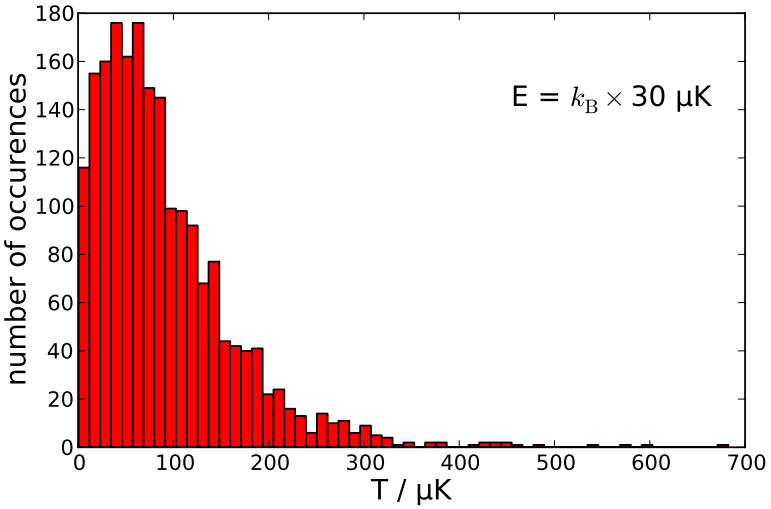

Figure 2.12: Energy distribution of an ensemble of single atoms with a temperature of $T = 30$ µK, as calculated by the simulation. For details see text.

data point about 200 shots are taken. Fig. 2.13 shows the results. For very short expansion times Δt, basically no atoms are lost. With increasing release time, the survival probability drops further with the highest slope at about 500 µs. After 3 ms, the survival probability is less than 10%.

This characteristic shape is reproduced by the numerical simulation. To find the best estimate for the temperature, a least squared analysis is performed for simulation runs of different temperature. The experimental data is fitted with the simulation of all simulated temperatures. The only fit parameter is the overall loading efficient, which is very close to unity and thus has only little influence. In Fig. 2.13 the simulation with $T = 30$ µK, that reproduces the experimental data best, is presented. The simulation agrees well with the experimental data. As an estimate of the uncertainty, the simulation corresponding to a temperature of $T = 20$ µK and $T = 40$ µK is plotted in Fig. 2.13, showing a significant deviation. Within the uncertainty, the temperature measured with the release and recapture method is equal to the one determined from the adiabatic lowering.

2.5 Conclusion

In this chapter, all necessary methods dealing with the impurity atoms were introduced. The analysis of the trap parameters shows a reasonable agreement with theory. The temperature of single Cs atoms is determined, the two employed methods provide a consistent quantitative understanding also in terms of the energy

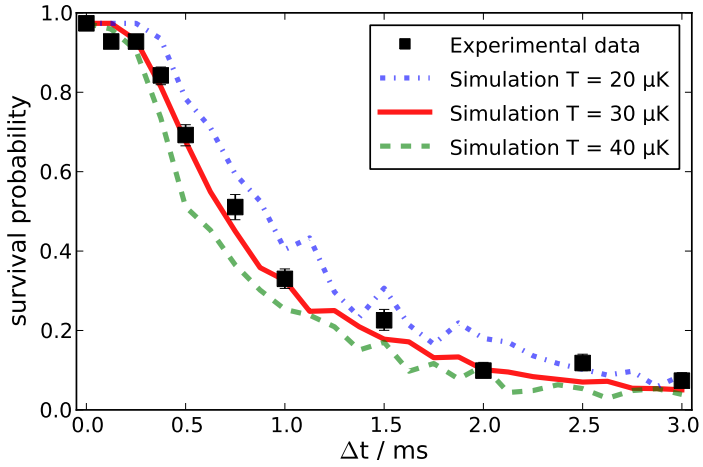

Figure 2.13: Temperature measurements of single Cs atoms in the lattice by a release and recapture experiment. The survival probability decays with a characteristic shape, that is reproduced by the numerical simulation. The simulation with $T = 30$ µK describes the experimental data best, for comparison the simulation for $T = 20$ µK and $T = 40$ µK is plotted.

distribution. With the release and recapture technique, a way to measure the temperature of atoms cooled deep into the trap is introduced. The understanding of the two sub-systems gathered in the last two chapters opens the way for the immersion of single and few Cs atoms into the ultracold Rb gas.

Chapter 3

Inserting single Cs atoms into an ultracold Rb gas

In the preceding chapters, the two different cooling and trapping schemes for laser-cooled single Cs atoms and ultracold Rb gases were introduced. These systems represent two different regimes. Single Cs atoms are loaded directly from a MOT and have therefore a relatively large temperature of about 30 µK. Rb, in contrast, is prepared by evaporative cooling with a temperature of about hundred nK and high atomic densities. These distinct properties lead to correspondingly different trapping potentials. The trap for single Cs atoms is stiff and deep, compared to the rather soft and shallow large volume trap employed for ultracold Rb.

The challenge here is to transfer single Cs atoms into the Rb cloud with a reasonable efficiency without affecting the ultracold Rb sample. In the following, a sequence is presented combining the traps of both subsystems in a way that allows the doping of the ultracold gas with impurity atoms.

3.1 Species-selective trapping and doping of Rb with Cs

To cool and trap two different atomic species in close proximity, a species-selective trap is necessary, for example by the choice of the dipole trap wavelength [85]. In our case the selectivity is created by operating a high-gradient MOT for Cs while Rb is optically trapped in a $m_{\mathrm{F}} = 0$ Zeeman sublevel. Due to the large difference in wavelengths of the D2-transitions of Rb and Cs (780 nm versus 852 nm), Rb atoms are not affected by the Cs MOT laser. For the Cs MOT, in turn, the dipole trap is a small perturbation (energy shift of $\approx k_{\mathrm{B}} \times 100$ µK $\approx \mathrm{h} \times 2$ MHz at full intensity) causing a light shift which does not impede the operation of the MOT.

The sequence starts by producing an ultracold Rb cloud in the running wave crossed dipole trap. Then, Rb is transferred into the magnetic-insensitive $|F = 1, m_{\mathrm{F}} = 0\rangle$

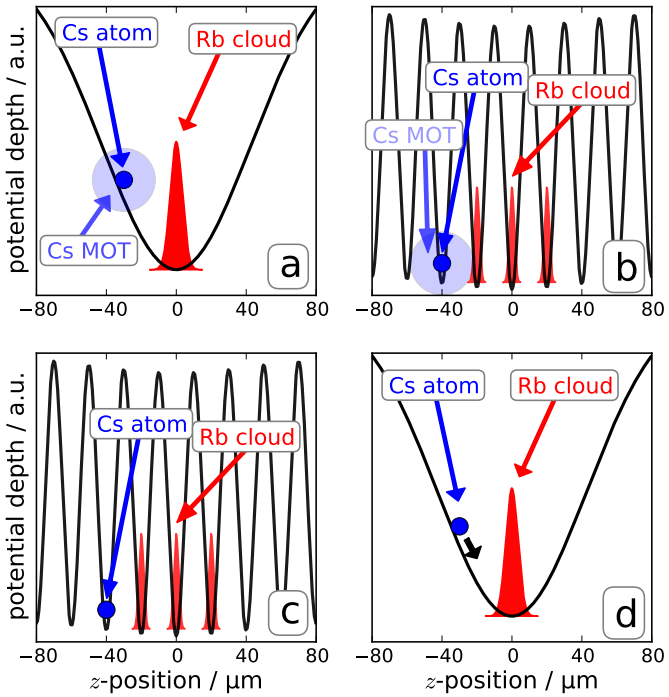

Figure 3.1: Schematic sequence to insert a single Cs atom into a Rb gas (not to scale). **a)** An ultracold Rb gas (red) is prepared in the crossed dipole trap in the $|1,0\rangle$ state, with a high-gradient MOT in close vicinity. Single Cs atoms are captured from the background gas. **b)** A lattice is adiabatically ramped up, confining both species in its optical potential. **c)** After switching off the Cs MOT, both species are stored in the conservative lattice potential in separated lattice sites. **d)** The lattice is ramped down (to zero intensity) adiabatically, thereby transferring both species into the original crossed dipole trap.

state, as discussed in section 1.3. Subsequently, the Cs MOT is switched on, with its center slightly offset from the Rb gas (in z-direction at $z \approx 30$ µm, Fig. 3.1(a)). Rb atoms remaining in a $m_F \neq 0$ state due to an imperfect pulse efficiency are removed from the trap by the gradient of the Cs MOT. During the low gradient loading stage (see 2.2.1), the geometrical size of the Cs MOT is large and the Cs density is low, so that strong light-induced Rb-Cs collisions are avoided. This ensures that a sufficient number of Cs atoms can always be trapped, independent of the relative position of Cs MOT and Rb gas. In the high-gradient stage, the density increases, the volume shrinks, and the loss rate can be employed for a precise relative positioning as explained below. The waist of the axial dipole trap is chosen to be $w_{\text{axial}} = 100$ µm, a few times larger than the diameter of the high-gradient Cs MOT of about 30 µm.

With the Cs MOT running, we transfer both species into the one-dimensional lattice (Fig. 3.1(b)). After switching off first the MOT laser and then the magnetic quadrupole field, both species are stored in purely optical potentials while being still separated (Fig. 3.1(c)). Then, Cs is optically pumped into the desired target state, described in more detail in section 3.3.2. Optionally, the internal state of Rb can as well be manipulated by rf/microwave radiation.

In the last step of the sequence, the lattice is ramped down adiabatically and the potential is transformed back into a running wave (Fig. 3.1(d)). Cs is cooled by this adiabatic expansion from a temperature of initially about 30 µK to a temperature of about 5 µK, discussed below in section 4.2. At some lattice depth, the Cs atom leaves its lattice site and is trapped in the running wave dipole trap together with the Rb gas. This process is discussed in more detail in the next section. From this point on, Rb and Cs interact in the conservative potential of the running wave dipole trap. In this chapter, however, we restrict the discussion to the transfer process and the fine positioning employing light-induced collisions of the two species. The understanding of these technical issues paves the way to study ground state interactions between single Cs atoms and the ultracold Rb gas presented in chapter 4.

3.2 Light-induced collisions and fine positioning

During the operation of the Cs MOT, the Cs atom scatters photons with a rate on the order of MHz. If in contact with the Rb cloud, the presence of near resonant light causes interspecies light-induced collisions [58, 71, 86]. These collisions provide a strong inelastic loss channel, causing Cs loss in a short time from the MOT if overlapped with Rb. In this regard a clear separation of the Cs MOT from the Rb cloud is favorable. To transfer the Cs atom into the running wave dipole trap, in contrast, the MOT should be as close as possible to the center of the trap, where the Rb is stored. A compromise between these two requirements allows to find an optimal position with a transfer efficiency of about 80%.

In order to find this optimal position, we first determine the transfer efficiency of Cs atoms into the running wave trap without Rb present. By superimposing the spatial modes of radial dipole trap and the lattice beams we ensure a good alignment for the radial dipole trap. This leaves the z-direction as the only free parameter influencing the transfer efficiency, which can be adjusted by the axial dipole trap. In Fig. 3.2 we measured this transfer efficiency as the survival probability of Cs in the running wave dipole trap using the sequence introduced above for different relative z-positions of the axial dipole trap without Rb present. We obtain a maximum survival probability after a storage time of one second of about 90%, where

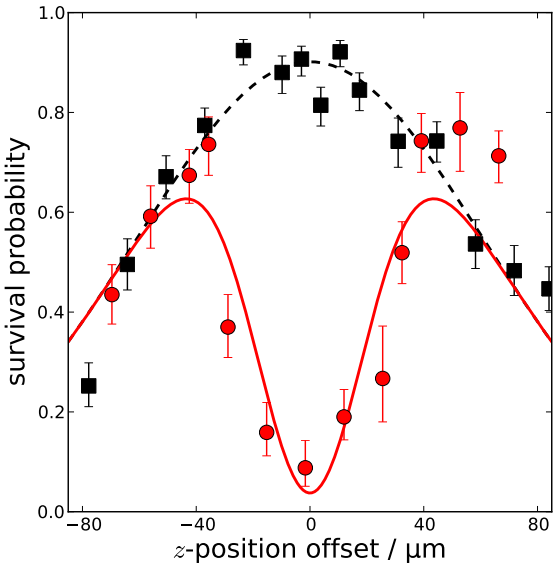

Figure 3.2: Fine tuning the relative distance of Cs single atom MOT and Rb cloud using light-induced collisions. Without Rb stored in the trap (■), the survival probability of Cs transferred to the crossed dipole trap is measured for different positions of the axial dipole trap in z-direction. The same measurement with a Rb gas stored in the crossed dipole trap shows a loss feature (●), indicating interspecies light-induced collisions that map out the density overlap of both species.

we attribute the slight reduction in survival probability to transfer loss. For an intentional misalignment, the survival probability decreases: For a displacement of about 50 µm, the survival probability is reduced roughly by a factor of two. The data of this experiment is fitted with a Gaussian profile $p_\mathrm{s}\exp(-z^2/w_\mathrm{YAG}^2)$, where p_s is the amplitude of the survival probability and w_YAG the waist of the Gaussian. The fit shows a reasonable agreement. As expected, the obtained width $w_\mathrm{YAG} = 86$ µm roughly corresponds to the waist of the axial dipole trap of 100 µm.

In a second step, we store Rb in the trap, which drastically changes the situation. In a typical sequence, we cool Rb by evaporation in the dipole trap to a temperature of 100 – 200 nK, with Rb atom numbers of a few 10^4. To decrease the size of the Rb gas and to provide a sufficient trap depth for the Cs atom, the trap is adiabatically compressed by ramping up the power of the dipole traps again. The temperature of the Rb gas rises due to this compression to several hundred nK, the size of the Rb cloud is about (7,7,14) µm and the density is in the low $10^{13}/\mathrm{cm}^3$ range. Then the Cs MOT is switched on (Fig. 3.1(a)) and the lattice is ramped up (Fig. 3.1(b)). Here, any overlap between the two species will lead to loss due to light-induced

collisions. Hence, upon varying the relative position between Cs MOT and Rb gas by changing the axial dipole trap position, the fraction of surviving Cs atoms will map out the effective interspecies overlap.

To prevent ground state interspecies collisions in the dark for this positioning measurement, we push Rb out off the trap immediately after loading into the lattice with a short resonant light pulse, directly after switching off the Cs MOT (Fig. 3.1(c)) and before ramping down the lattice (Fig. 3.1(d)). We have verified that this pulse does not affect the Cs atoms. This push out ensures that the two species are interacting via light-induced collisions only. Light-induced collisions during recapture of Cs are thus also avoided.

Assuming inelastic Cs-Rb two-body collisions as the dominant loss mechanism, the loss probability of Cs atoms is directly proportional to the density-density overlap of Rb and Cs. The density distributions for a thermal Rb cloud as used in this experiment as well as for the compressed Cs MOT can be described by a Gaussian with widths of $w_{\mathrm{Rb}} \approx 14$ µm (Rb gas) and $w_{\mathrm{Cs}} \approx 15$ µm (Cs MOT). To provide a model for this loss, a Gaussian $p_{\mathrm{loss}} \exp(-z^2/w_{\mathrm{loss}}^2)$ is subtracted from the survival probability of Cs without Rb. The measurement presented in Fig. 3.2 shows the experimental data and a fit with a function corresponding to this model. For distances of more then about 40 µm between Cs MOT and the center of the trap, the survival probability is the same as without Rb present. For smaller distances, however, the survival probability is reduced. With the MOT in the center of the trap, essentially no Cs atom survives, indicating a matched overlap between Cs and Rb.

The agreement between our model (Fig. 3.2, red solid line) and the data is reasonable. The width w_{loss} of the "loss feature" is given by the convolution of the density profiles of both species and thus expected to be $w_{\mathrm{loss,theo}} = \sqrt{w_{\mathrm{Cs}}^2 + w_{\mathrm{Rb}}^2} \approx 21$ µm, close to the value of $w_{\mathrm{loss}} = 27$ µm obtained from the fit. However, there are significant deviations. The slope of the loss feature ($0 < |z| \approx \pm\ 40$ µm) appears to be steeper than expected from our simple model. A reason for this could be the onset of Cs-Rb-Rb three-body losses for higher Rb densities in the center of the trap. For our purpose, however, it is sufficient to experimentally determine the point of highest survival probability for Cs with Rb present, at $z \approx \pm\ 30$ µm. At this point, the insertion of single Cs atoms into the Rb cloud has an efficiency of close to 80%.

3.3 Analysis and simulation of the transfer

For the study of ground state collisions, the time t_{T} when Cs is transferred from its lattice site to the running wave dipole trap defines the start of interspecies interaction. Therefore, the knowledge of t_{T} is crucial. Because of the thermal energy

distribution of the atoms, there is a finite probability for a Cs atom to leave the lattice already during the adiabatic lowering, before the lattice is extinguished completely. This effect analogous to evaporation is analyzed in the following.

The adiabaticity in the transformation from the running wave to the lattice and back is necessary to adiabatically cool Cs and to prevent excessive heating of the ultracold Rb cloud. On the other hand, this approach inevitably smears out the point in time at which Cs leaves its lattice site and is trapped in the running wave trap. Hence, a trade-off between these two requirements is necessary here. In the experiments, the lattice is ramped down in an adiabatic way for Cs to a finite value below 1% and then non-adiabatically switched off. Due to the smaller trap frequencies for Rb, the condition for adiabaticity is not strictly fulfilled for Rb. The heating of Rb caused by the adiabatic lowering and the non-adiabatic extinction of the lattice is included in all measurements by monitoring the temperature always after inserting Cs. To address the question of the transfer time of Cs, simulations of the experiments are performed, discussed in the following.

The transformation from the lattice to the running wave crossed dipole trap introduced in the preceding section (see Fig. 3.1(c) and 3.1(d)) is realized in two different configurations. The first beam of the running wave crossed dipole trap is always provided by the axial dipole trap, that also guides Rb during the magnetic transport. In the first approach, both lattice beams are independently adiabatically lowered. The transformation is accomplished in this case by lowering one beam to a finite intensity while completely extinguishing the other. The result is a "dichromatic" running wave crossed dipole trap at the end of the lowering ramp, where one beam has a wavelength of 1064 nm (axial beam) and the other 899.93 nm (single lattice beam). In the second configuration, the lattice beams are lowered simultaneously and then extinguished at the same time. The second beam of the crossed dipole trap in this configuration is provided by the radial dipole trap introduced above. In this way, the atoms are stored in an usual "monochromatic" running wave dipole trap at the end of the sequence.

In the following, the characteristics of both configurations are discussed in detail. Both configurations are employed later to study interspecies ground state interactions.

3.3.1 Dichromatic running wave dipole trap

The experimentally simplest way to transform the lattice to a running wave crossed dipole trap is to use a single lattice beam as the second beam of the cross. In Fig. 3.3(b), the intensity ramp of both lattice beams in this approach is plotted

logarithmically. The shape of the ramp is the same as the one introduced in section 2.3.2, so that adiabaticity is fulfilled for Cs. Both arms of the lattice are ramped down in 100 ms, one arm to 11% of the initial intensity, the second arm is completely extinguished after 100 ms. At this time, the intensity has a value of about 0.2%. During the course of the lowering, the intensity difference between both arms increases, thereby creating a running wave crossed dipole trap.

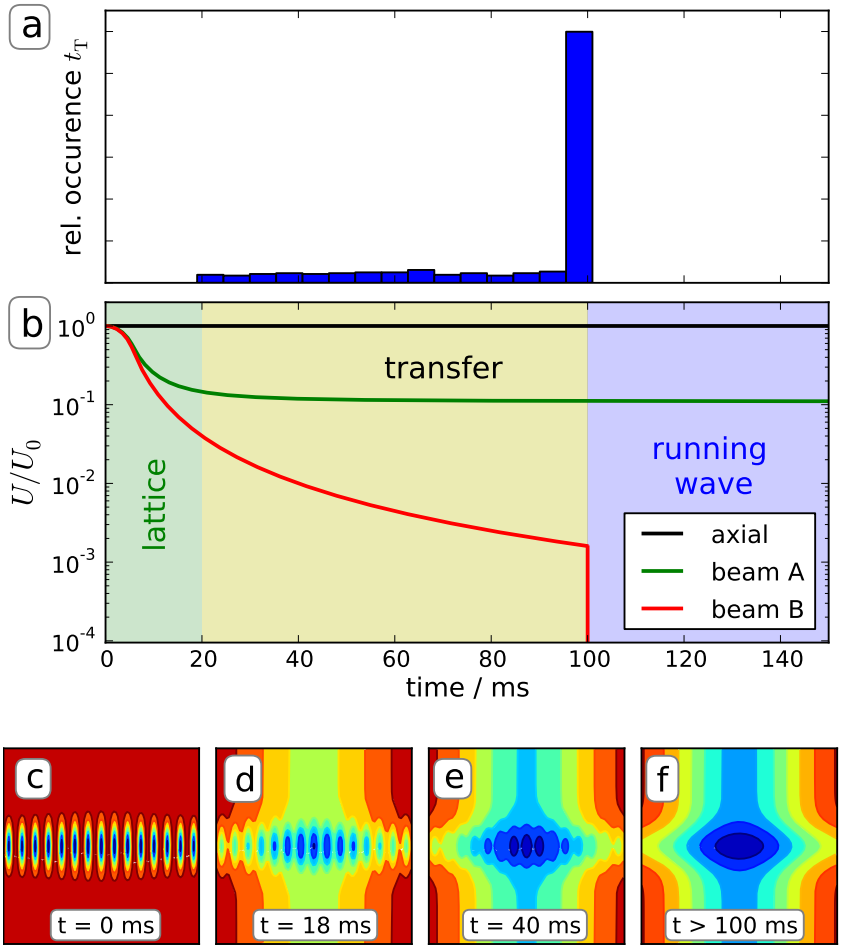

Figure 3.3: Transformation of the lattice to a "dichromatic" running wave crossed dipole trap. **a**) Histogram of transfer times t_T obtained by the simulation. **b**) Intensity ramp of the two counter propagating lattice beams (beam A and beam B) and the axial dipole trap. One beam (beam B) is completely extinguished after the adiabatic lowering, the other one (beam A) is lowered to a finite level of 11% of the initial intensity. The axial dipole trap stays at constant intensity during the whole sequence. **c)-f**) Resulting overall potential for Cs at different stages of the sequence. The lattice spacing is increased by a factor of 30 for clarity, the field of few is 200 µm × 200 µm. The color coding corresponds to a potential depth of 770 µK (**c**)), 105 µK (**d**)), 76 µK (**e**)) and 67 µK (**f**)).

Since one lattice beam is left at finite power, the adiabatic lowering is different from the basic process in the pure lattice. The influence of gravity is weaker, because there is always one arm of the lattice potential that supports the atoms. Furthermore, the axial dipole trap is at constant trap depth during the whole transformation, providing additional confinement. This is also the main reason why the atoms leave the lattice at relatively low intensities. For comparison, in the pure lattice potential only about 10% of the atoms survive a lowering to 1% of the initial lattice depth.

In order to get a quantitative description of the transformation, a numerical simulation of the trajectories of a Cs atom during the transformation process is performed. For this, the simulation in the same manner introduced in section 2.4 is employed. It starts by choosing an Cs atom with random energy, where the energy distribution is governed by a Maxwell-Boltzmann distribution with $T = 27$ µK. Then, the atom is put into the lattice at full intensity at random spatial position and velocity. The insertion point of the atom in z-direction is chosen at 30 µm offset from the center of the axial dipole trap, corresponding to the position of the MOT. The atomic trajectory is then calculated for the complete time evolution of the intensity shown in Fig. 3.3(b). During the whole time of the simulation, the axial dipole stays at constant intensity.

The atomic trajectory can be described in two major regimes. In the first part ($0 < t < \approx 20$ ms), the atom is trapped in its lattice site and experiences an adiabatic expansion. Therefore the velocity of its oscillation shrinks, the energy is lowered. In the second part (≈ 20 ms $< t < 100$ ms), there is a finite probability that the atom leaves its lattice site and gets trapped in the running wave trap, 30 µm offset. The time of the transfer depends on the energy of the atom and the initial conditions. Finally, at $t = 100$ ms, the remaining lattice is non-adiabatically extinguished. At this point, any Cs atom is transferred into the running wave trap, irrespective of its energy.

In order to quantify the transfer timing, for each calculated atomic trajectory the point in time is found where the atom first crosses the focus of the running wave trap at $z = 0$. In Fig. 3.3(a) the histogram of transfer times is shown. The majority of the atoms leave the trap at $t = 100$ ms, when the lattice is extinguished. A finite fraction, however, is transferred already during the course of the lowering. As a consequence, with Rb stored in the trap, the interspecies interaction in this sequence starts before the lattice is completely extinguished. This effect is also observed in the thermalization measurement in section 4.2, discussed below.

The fraction of atoms leaving the lattice before $t = 100$ ms and the shape of the histogram is found to strongly depend on parameters like the offset between MOT

and crossed dipole trap and the temperature. Also, the simulation for the transfer process provides only a rough approximation. The distribution of the start positions of the atoms due to the finite size of the MOT, for instance, is not considered here. Therefore, the result of the simulation has to be interpreted with care. However, the simulation provides an approximate description of the process, that can be employed to compare the two different trap configurations used.

Because one of the lattice beams is used to form the potential, the dichromatic running wave dipole trap is relatively near resonant. The photon scattering rate for Cs atoms can be estimated to be $\Gamma_{\mathrm{Cs,dc}} \approx 9\ \mathrm{s}^{-1}$, the corresponding heating rate is accordingly $P_{\mathrm{Cs,dc}} \approx 1.7\ \mu\mathrm{Ks}^{-1}$.

3.3.2 Monochromatic running wave dipole trap

In a second approach, the running wave dipole trap at the end of the transformation is formed by two beams at a wavelength of 1064 nm, that create the axial and the radial dipole trap introduced above. The result is an usual monochromatic crossed dipole trap. This configuration has several advantages, the most important being the wavelength. Heating and optical pumping of Cs are significantly suppressed at 1064 nm ($\Gamma_{\mathrm{Cs,mc}} \approx 1\ \mathrm{s}^{-1}$, $P_{\mathrm{Cs,mc}} \approx 130\ \mathrm{nKs}^{-1}$). Another benefit is the free choice of the trap geometry. The drawback is the higher complexity in experimental setup and adjustment.

The experiment in this case starts with preparing an ultracold Rb sample in the monochromatic crossed dipole trap. Subsequently, the sequence to insert single Cs atoms described above is applied. During the whole procedure, the crossed dipole trap at 1064 nm is held at constant intensity. The transformation back into the pure running wave crossed dipole trap is in this case simply accomplished by ramping down both lattice beams simultaneously in 80 ms to about 0.5% of the initial lattice depth. At this point, both arms are completely extinguished, leaving the original crossed dipole trap as the only potential. Fig. 3.4 shows the lattice potential ramp during the transformation in the same scale like the dichromatic case in Fig. 3.3.

The approach with the monochromatic running wave crossed dipole trap shows a slightly sharper transfer timing. The fraction of atoms being transferred before the lattice is extinguished is smaller, furthermore the time period in which atoms are transferred is shorter. Additionally, the suppression of photon-scattering in this trap facilitates the control of the internal state of Cs.

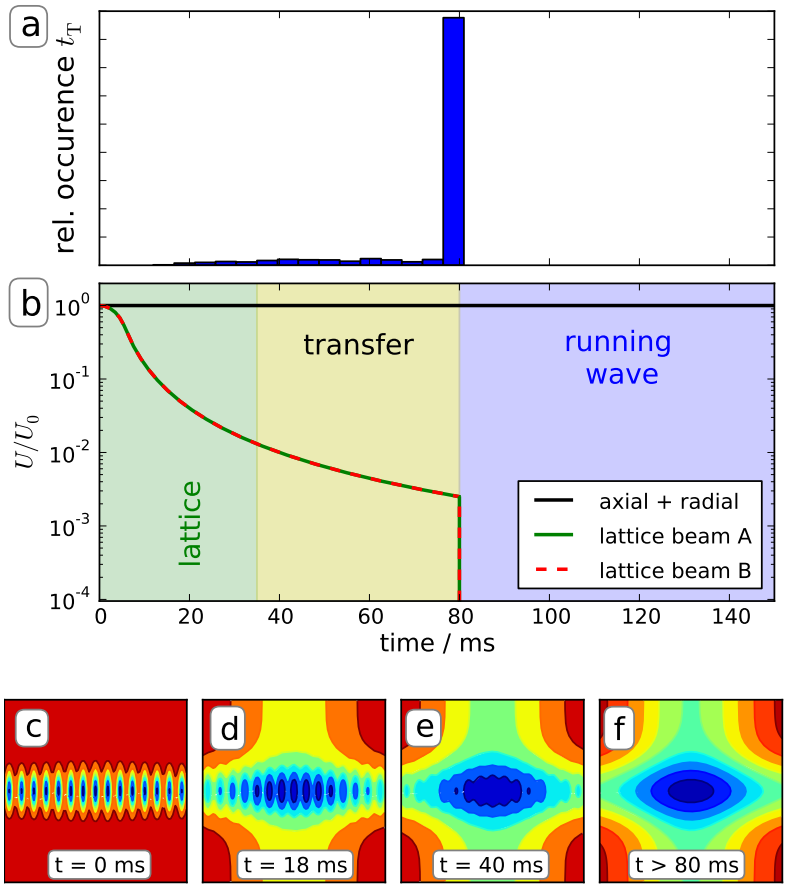

Figure 3.4: Transformation of the lattice to a "monochromatic" running wave crossed dipole trap. **a**) Histogram of transfer times t_T obtained by the simulation. **b**) Intensity ramp of the two counter propagating lattice beams. Both beams (beam A + beam B) are completely extinguished after the adiabatic lowering. The axial and radial dipole trap, forming the final crossed dipole trap, stay at constant intensity during the whole sequence. **c)-f**) Resulting overall potential for Cs at different stages of the sequence. The lattice spacing is increased by a factor of 30 for clarity, the field of few is 200 µm × 200 µm. The color coding corresponds to a potential depth of 946 µK (**c**)), 138 µK (**d**)), 104 µK (**e**)) and 96 µK (**f**)).

Manipulation of the internal degree of freedom of Cs in the monochromatic running wave crossed dipole trap

For the interspecies interaction, the control of the internal degrees of freedom of both species is substantial. This section introduces the techniques used for the case of single Cs atoms stored in the monochromatic running wave crossed dipole trap and presents the experimentally achieved manipulation. For all experiments in this section, the same sequence discussed above (section 3.1) is used without Rb stored

in the trap. Cs is loaded in the center of the running wave dipole trap, causing accordingly slightly higher survival probabilities of Cs.

Optical pumping. To prepare Cs in the $F = 3$, $m_F = 3$ Zeeman sublevel, an optical pumping scheme is applied. A laser with σ^+-polarization, resonant with the $F = 3 \rightarrow F' = 3$ transition, pumps atoms from any Zeeman sublevel within the $F = 3$ manifold into the $F = 3, m_F = 3$ state. At the same time, atoms in the $F = 4$ state are pumped (back) into the $F = 3$ hyperfine manifold by another laser resonant to the $F = 4 \rightarrow F' = 4$ transition. The quantization axis is provided by the same coil that is used to optically pump Rb into the $|2, 2\rangle$ state.

The optical pumping is applied in the lowered lattice (see Fig.3.1(c)), before Cs and Rb are brought into contact. On one hand, this ensures that the photon scattering rate is kept low such that Cs is not pumped into different states by off-resonant Raman scattering. On the other hand, Cs is prepared in its target state before interacting with Rb, such that the interspecies interaction can be studied with well-defined states. Additionally, light-induced processes during interaction with the optical pumping beams are avoided.

Microwave spectroscopy and Rabi oscillations. To read out the Zeeman sublevel of Cs, the state-selective pushout cannot be used due to the small level splitting. Therefore a transition between the hyperfine states of Cs is driven using microwave radiation to map the Zeeman sublevel onto the hyperfine states. The hyperfine state can then be determined by the state-selective pushout. This also enables the estimation of the efficiency of the optical pumping.

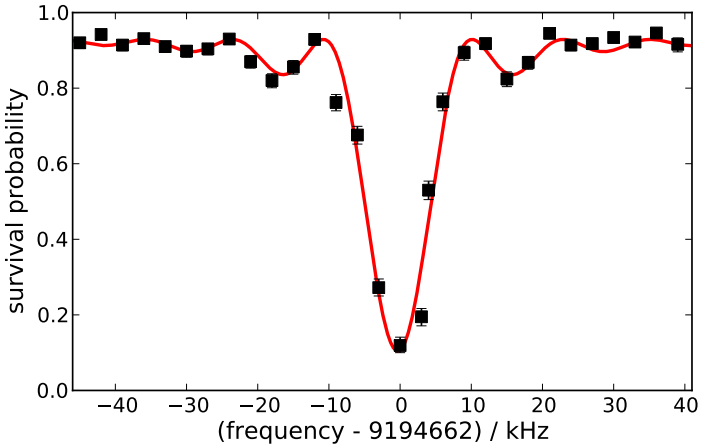

Figure 3.5: Fourier-limited spectrum of single Cs atoms stored in the running wave dipole trap.

In a first experiment, the microwave spectrum of single Cs atoms is measured. For this, a Cs sample is prepared in the running wave crossed dipole trap without Rb stored. Then the atoms are pumped into the $|3,3\rangle$ state. Subsequently, a microwave pulse with a duration of 80 µs is applied (see [72] for details). The frequency of this pulse is scanned across the $|3,3\rangle \rightarrow |4,2\rangle$ transition. Finally, the state-selective pushout removes atoms in the $F = 4$ state from the trap. The remaining atoms in the $F = 3$ state are counted.

In Fig. 3.5 the corresponding spectrum is presented. When the mircowave pulse is resonant to the transition, the survival probability (for atoms transferred into $F = 4$) decreases to about 10%, whereas the survival probability for a far detuned pulse amounts to about 90%. From this, the efficiency of the optical pumping can be estimated to be better than 80%. The reduction in efficiency can be caused by the optical pumping itself, loss during the transfer or by the state-selective push out. The width of the transition is Fourier-limited, the red line is a fit corresponding to the expected transfer.

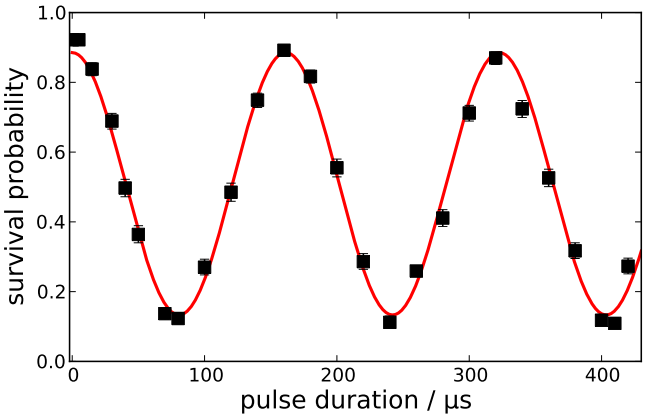

Figure 3.6: Rabi flopping of single Cs atoms showing a Rabi frequency of $\omega_{|3,3\rangle\rightarrow|4,2\rangle} \approx 2\pi \times 6.2$ kHz.

With the microwave radiation, it is possible to drive Rabi oscillations between the two hyperfine states of Cs. For this the frequency is set to the resonance of the transition. Then the pulse duration is varied and, after the state-selective pushout, the number of atoms remaining in the trap is counted. Fig. 3.6 shows the Rabi flopping of single Cs atoms in the running wave crossed dipole trap. For several Rabi cycles, the contrast stays constant at about 75%. This enables the coherent manipulation of Cs, that is used for Ramsey spectroscopy (see section 5.1 and master thesis of Farina Kindermann [72]).

A main advantage of the running wave crossed dipole trap is the strongly suppressed

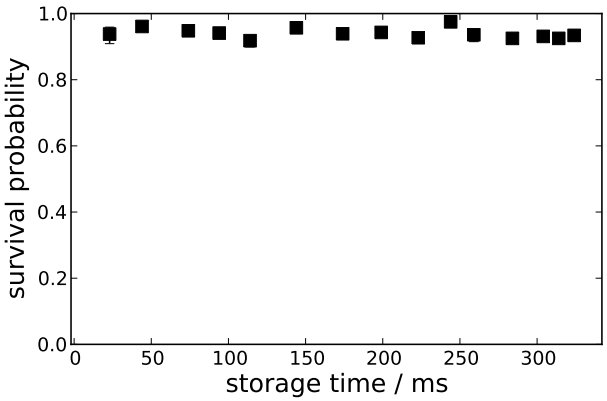

Figure 3.7: Experiment to estimate the off-resonant scattering of dipole trap photons. The state of Cs does not change on the observed time scale.

photon scattering rate. To confirm this experimentally, Cs is prepared in the running wave crossed dipole trap in the $|3,3\rangle$ state. After a holding time, the state-selective pushout is used to read out the state.

In Fig. 3.7 the resulting data is plotted. For the investigated time scale on the order of several hundred ms seconds, no loss indicating a change of state can be detected. This is consistent with the expected time on the order of several seconds [75, 78]. Compared with the situation in the lattice even at low intensities (section 2.3.4), this is a drastic improvement.

3.4 Conclusion

A sequence to dope ultracold Rb gases with Cs impurity atoms was introduced. Two configurations were presented, both of which are used in the next chapter to study ground state interspecies interactions. The approach using the dichromatic trap is suited best, when the photon scattering from the lattice beam can be neglected, as in the case of the rapid interspecies thermalization in section 4.2. The monochromatic running wave trap allows to store both species for long times with negligible off-resonant photon scattering. This is the prerequisite for the measurement of three-body collisions in defined Zeeman sublevels of both species presented in section 4.3. Furthermore, in the monochromatic running wave dipole trap, coherent manipulation of single Cs atoms was demonstrated.

For future experiments, the doping of a BEC with impurity atoms is of special interest. However, the experiments presented in this thesis deal with the interactions of both subsystems. For this, a BEC is not necessary, therefore the insertion sequence was up to now only applied to thermal, high-phase space density samples. In general,

however, the introduced technique should be directly applicable to dope a BEC. Due to the selectivity of both the monochromatic and the dichromatic trap, it should be possible to cool the high density thermal Rb cloud to quantum degeneracy without loosing the Cs atom, if necessary.

Chapter 4

Single Cs atoms interacting with an ultracold Rb gas

Many properties of ultracold gases are governed by interactions of the constituent atoms. Accordingly, the interaction between an impurity atom and the buffer gas determines the properties of the hybrid system that is the object of this thesis. In this chapter, elastic and inelastic collisions between the impurity atom and atoms of the buffer gas are studied, providing insight into the interaction properties. Here, our system shows some distinctive features.

In most experiments, large ensembles of atoms are employed, as for example in mixtures of two species [29, 55, 87]. Therefore usually both subsystems are affected by the interaction. In the experiments presented in the following, in contrast, few and single Cs impurity atoms interact with a by far larger many-body system, represented by the Rb buffer gas. The time-resolved thermalization of the impurity atom via elastic collisions with atoms of the buffer gas is observed, allowing the estimation of the interspecies collisional cross section. While the impurity atom experiences a strong change of its thermodynamical properties, the buffer gas remains effectively unaffected. This demonstrates the probing of the temperature of the many-body system by the impurity atom.

Accordingly, experiments dealing with a large number of atoms are sensitive to averaged properties of the ensemble, so that fluctuations of the probed quantity usually do not play a role. However, these fluctuations are governed by the statistics of the ultracold gas and can therefore be employed to gain information about the system. This has been exploited, for instance, to directly observe sub-Poissonian number statistics in a BEC [41], pair-correlations in a gas of fermionic atoms [88] and number squeezing in a Mott insulator [21, 42]. Since our experiment monitors single impurity atoms, number fluctuations are resolved with atomic resolution. This is exploited when the decay of the survival probability of the impurity atoms due

to interspecies three-body recombination is studied. The exact knowledge of the impurity atom number allows observing interactions atom-by-atom. Furthermore, the fluctuating number of atoms lost facilitates to study losses event-by-event. With this additional information, losses can be attributed to a single loss channel, which is not directly possible in experiments dealing with balanced mixtures. Extending the demonstrated approach to higher impurity atom numbers could be employed to study the transition from two-body to many-body systems in future experiments.

4.1 Interactions at ultracold temperatures

Before discussing the experimental results of the interspecies interaction, in this section, the relevant theoretical framework of ultracold collisions is briefly reviewed [13, 86, 89, 90]. The emphasis here is given to the interaction of an impurity atom with one atom of the buffer gas (two-body collisions) or with two atoms of the buffer gas (three-body collisions). The discussion focuses on collisions of distinguishable particles in the regime realized in the experiment.

4.1.1 Elastic two-body collisions

In our experiment, single Cs atoms are interacting with an ultracold Rb gas with a mean density below $\bar{n} = 10^{14}\,\mathrm{cm}^{-3}$. Despite the low temperature, the gas is therefore dilute such that $\bar{n}a^3 \ll 1$, where a is the scattering length. Hence, interactions can be described to a large extend by elastic two-body collisions, where a single Cs atom is colliding with a single Rb atom of the many-body system. In this framework the interspecies thermalization discussed in section 4.2 can be understood.

By introducing the reduced mass $m_{\mathrm{red}} = m_1 m_2/(m_1 + m_2)$, the two-body problem can be reduced to a one-body problem and is described in the centre-of-mass frame by the stationary Schrödinger equation

$$\left(\frac{\hbar^2}{2m_{\mathrm{red}}}\nabla^2 + V(\vec{r})\right)\Psi(\vec{r}) = E\Psi(\vec{r}). \tag{4.1}$$

The incoming wave can be assumed to be a plane wave with wavevector $\vec{k}$. For large distances, the asymptotic solution for a short range potential $V(\vec{r})$ is a spherical wave, so that

$$\lim_{r\to\infty}\Psi(\vec{r}) \propto e^{i\vec{k}\vec{r}} + f(k,\Theta)\frac{e^{ikr}}{r}. \tag{4.2}$$

The scattering amplitude $f(k, \Theta)$ is connected to the total cross section σ via

$$\sigma = \int_{\Omega} |f(k, \Theta)|^2 d\Omega, \tag{4.3}$$

where Θ is the angle between the incoming wave and the axis of detection and Ω is the solid angle.

For a spherical potential the total angular momentum has to be conserved during a collision. Since the problem is independent from the azimuthal angle, the Schrödinger equation is reduced to a one-dimensional problem. The solutions can be expanded in partial waves for the angular momenta l. The effective potential can then be written as the sum of a spherical potential $V(r)$ and a centrifugal potential

$$V_{\text{eff}}(r) = V(r) + \frac{l(l+1)}{2m_{\text{red}}r^2}. \tag{4.4}$$

The centrifugal potential vanishes for $l = 0$ (s-wave scattering). For higher l, the centrifugal potential adds a barrier that can not be passed for low scattering energies, so that no interaction occurs. In the temperature regime in our experiment with $T < 10$ µK, only the s-wave scattering contributes to the interaction.

The scattering can be described by a phase shift $\delta_l(k)$ of the outgoing wave with respect to the incoming wave. The total cross section is then given by

$$\sigma = \frac{4\pi}{k^2} \sin^2 \delta_0(k) \tag{4.5}$$

where only s-wave scattering is considered. In the limit of vanishing k, the phase vanishes because $\delta_0 \propto k$. The total cross section in this regime becomes

$$\sigma_0 = 4\pi a^2, \tag{4.6}$$

with the s-wave scattering length

$$a = -\lim_{k \to 0} \frac{\tan \delta_0(k)}{k}. \tag{4.7}$$

In general, Alkali atoms feature several asymptotic states. For small distances, the corresponding atomic quantum numbers are no good quantum numbers anymore. Instead, coupled quantum numbers have to be employed, that lead to corresponding potentials, that are in general different from each other. Each of the corresponding potentials can be described in terms of a respective s-wave scattering length. In

Table 4.1 singlet (a_s) and triplet (a_t) intra- and interspecies s-wave scattering lengths for Rb and Cs are listed.

	Rb [91]	Cs [92]	Rb-Cs [56]
$a_s(a_0)$	90.4	280	unknown
$a_t(a_0)$	99	2400	≥ 150

Table 4.1: Singlet and triplet scattering lengths for Rb and Cs.

4.1.2 Inelastic two-body collisions

Depending on the initial states of two colliding atoms, final states with a lower total energy can exist. The difference in energy is then transformed into kinetic energy, leading to a loss from the trap if the energy difference is sufficiently large.

Inelastic two-body collisions can be classified into spin-exchange collisions with $\Delta m_F = 0$ and dipolar relaxation with $\Delta m_F + \Delta m_l = 0$, where Δm_l is the quantum number of the projection of the angular momentum. The Zeeman splitting for Rb is 700 kHz / G and 350 kHz / G for Cs [74, 93]. In section 4.3.3 two-body loss of Cs impurity atoms in the excited hyperfine state ($F = 4$) is observed. If both species are prepared in their absolute ground state ($|3,3\rangle$ for Cs, $|1,1\rangle$ for Rb), no final states with lower energy exist, such that inelastic two-body collisions are forbidden. In this case, losses are dominated by three-body recombination.

4.1.3 Inelastic three-body collisions

Even though a major part of the interactions of ultracold gases can be understood in terms of two-body collisions, ultracold gases are strongly subcooled and therefore meta-stable. In a two-body collisions, energy and momentum conservation can not be fulfilled at the same time, effectively inhibiting molecule formation. Three-body collisions, in contrast, allow the conservation of energy and momentum. For increasing interaction times, collisions of the impurity atom with two atoms of the ultracold ensemble play an increasing role and can lead to the formation of a molecule. The binding energy in the range of typically several hundred MHz is then converted into kinetic energy that is shared among the colliding atoms according to their mass ratio. Since the typical trap depth is on the order of $k_B \times 10$ µK corresponding to $\approx h \times 200$ kHz, it is safe to assume that the atoms are lost from the trap. The three-body loss rate coefficient L_3 shows a strong dependence on the s-wave scattering

length a. It is predicted to scale as

$$L_3 = \frac{3C\hbar}{m} a^4 \tag{4.8}$$

where C is a dimensionless constant between 0 and 70 [43, 94, 95]. This scaling was observed in several experiments [44, 96, 97]. In our experiment, three-body recombination limits the lifetime of the impurity atom, as observed in the experiment described in section 4.3.2.

4.2 Elastic collisions – Thermalization

A fundamental signature of interspecies interaction in the hybrid system is the sympathetic cooling of the impurity atom by the buffer gas. In order to avoid interspecies two-body losses during interaction with the buffer gas, Cs is pumped into the lowest hyperfine manifold ($F = 3$ state). The experiments in this section use the "dichromatic" crossed dipole trap, where the axial dipole trap and one arm of the lattice are combined. Fig. 4.1 gives an impression of the setup in this configuration.

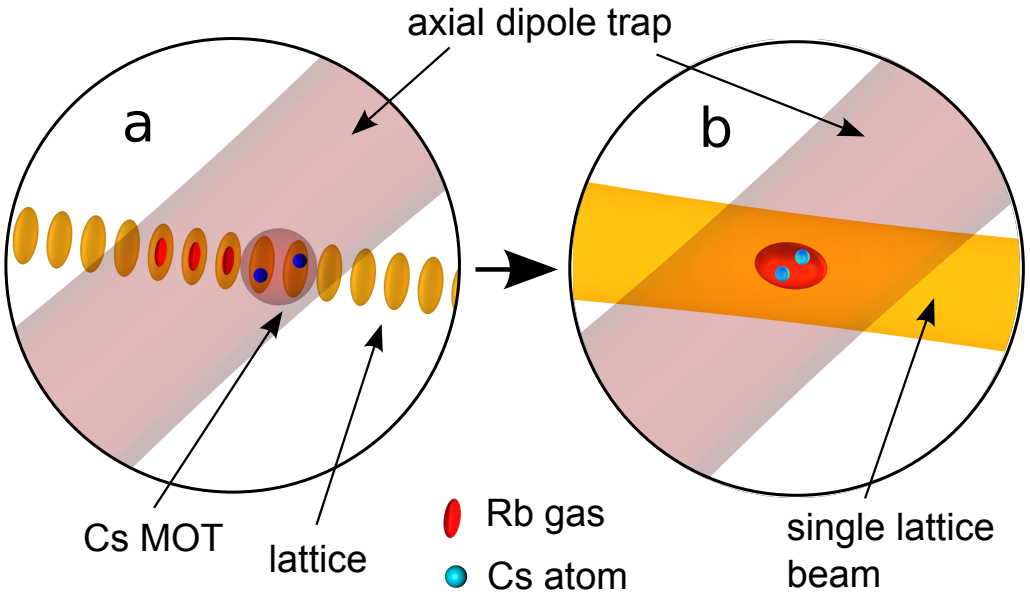

Figure 4.1: Illustration of the setup for the dichromatic running wave dipole trap, as used in this section (not to scale). **a)** Loading single Cs atoms into the MOT with Rb stored (see also Fig. 3.1(b)). **b)** Interaction of both species in the dichromatic running wave dipole trap, consisting of axial dipole trap and a single lattice beam (see also Fig. 3.1(d)).

4.2.1 Temperature measurement of Cs in the running wave crossed dipole trap

To study the interspecies thermalization, the determination of the temperature of Cs in the running wave crossed dipole trap is necessary. The main demand here is the measurement of relatively low temperatures of the impurity atom, therefore the release and recapture method, as discussed in section 2.4, is best suited.

In a first experiment, single Cs atoms are inserted into the dichromatic running wave dipole trap with the sequence presented in the previous chapter 3, without Rb stored in the trap. The parameters of the trap used are given in Table 4.2. Then the release and recapture measurement is performed by switching off non-adiabatically the running wave trap. Fig. 4.2 shows the results. Again, the initial survival probability is about 80%, as expected due to the insertion sequence. From this value, the survival probability decays within a release time of 2 ms to below 10%. The shape of this decay is significantly different from the corresponding experiment in the lattice, presented in section 2.4.2.

This characteristic shape is reproduced by a numerical simulation in the same manner as for the lattice potential in section 2.4.2. The corresponding potential is now the dichromatic running wave crossed dipole trap, where one beam is formed by the radial dipole trap and the other one by a single arm of the lattice. It can be described by

$$\begin{aligned} V_{\mathrm{DT}}(x,y,z,t) &= U_{\mathrm{TiSa}}(t)\exp(-2(x^2+y^2)/w_{\mathrm{TiSa}}^2) \\ &+ U_{\mathrm{YAG}}(t)\exp(-2(x^2+z^2)/w_{\mathrm{YAG}}^2). \end{aligned} \tag{4.9}$$

	radial	axial	Ti:Sa running wave
Rb depth/k_B (µK)	0	27	1.8
Cs depth/k_B (µK)	0	48	19
Wavelength (nm)	1064	1064	899.9
Waist (µm)	48	100	31
Rb rad. freq. (Hz)	-	160	130
Rb ax. freq. (Hz)	-	<1	<1
Cs rad. freq. (Hz)	-	170	350
Cs ax. freq. (Hz)	-	<1	2

Table 4.2: Parameters of the traps used in this section for the thermalization measurement.

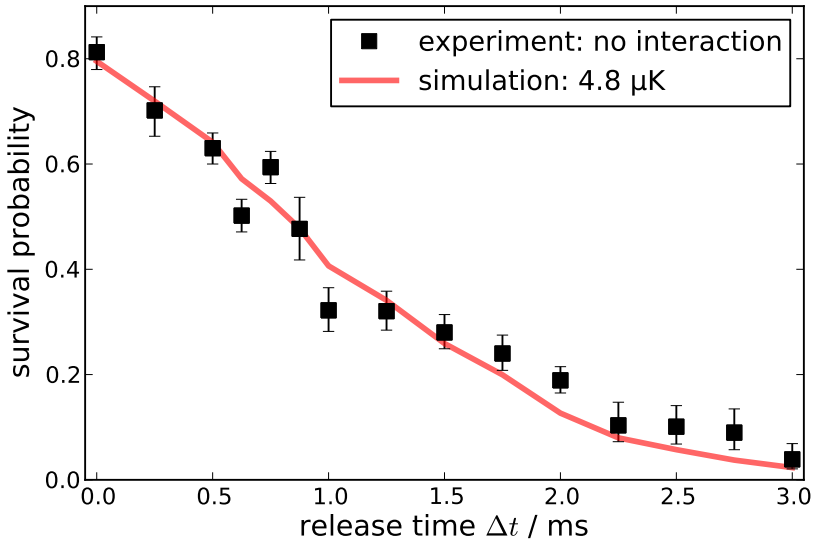

Figure 4.2: Release and recapture experiment with single Cs atoms in the running wave dipole trap, without Rb present. The solid line indicates the decay of survival probability obtained by the simulation, yielding $T_{\mathrm{Cs}} \approx 4.8$ µK.

The release and recapture experiment in the running wave is computed for temperatures $0.2 < T < 5$ µK in steps smaller than 200 nK. To extract the absolute value of the temperature from the release and recapture measurements like in Fig. 4.2, a least-square fit is performed for all simulated temperatures, where the only free parameter is the initial transfer efficiency. This value amounts to around 80%, in good agreement with the transfer discussed in section 3. As a measure of the goodness-of-fit, χ^2 is calculated. The simulation with the smallest χ^2 then determines the temperature, discussed in more detail below (section 4.2.3).

In Fig. 4.2 the result of this analysis is plotted as a solid line. The decay of survival probability agrees with the experimental data within the uncertainty, corresponding to a temperature of 4.8 µK. The experimental sequence bringing both species into contact relies on the adiabatic extinguishing of the lattice, causing an adiabatic expansion and thereby a cooling of the Cs sample. The initial temperature of Cs in the lattice was determined to be $T_0 \approx 30$ µK (see chapter 2). In harmonic approximation the trap frequency scales with the square root of the potential depth $\omega \propto \sqrt{U}$, the temperature after the expansion can be estimated for the new trap depth by $T(U') = T_0\sqrt{U/U'}$. Thus the temperature is expected to be $T_0\sqrt{U/U'} \approx$ 5 µK, in good agreement with the measured temperature of 4.8 µK.

Regarding the task to insert a "hot" laser-cooled atom into the ultracold gas, the importance of the adiabatic cooling via the lattice becomes apparent. The trap

depth of the potential for the ultracold gas is only on the order of few 10 µK (see Table 4.2). The Cs atom has a temperature of about 30 µK when loaded from the MOT, which is already below the Doppler limit. To reliably store the Cs atom in the dipole trap the potential depth should be at least a factor of ten deeper than the temperature. This can also be seen from Fig. 2.12, where the temperature distribution for an atom with $T = 30$ µK is plotted. Hence, without adiabatic cooling, Cs can not be transferred efficiently into the running wave trap. With the adiabatic cooling the trap used to store ultracold Rb can easily be made deep enough to fulfill the criteria and therefore reliably store Cs.

It should be noted that this cooling process is a purely thermodynamic expansion and does not involve any dissipation. The vibrational state does not change during the expansion. This is different for the sympathetic cooling discussed below.

4.2.2 Experimental techniques for the realization of interspecies interaction

In the first step of a typical experiment, the sequence described in chapter 3 is used to prepare a Rb sample doped with single Cs atoms. Light-induced collisions lead to a rapid loss of Cs stored in a MOT, when interacting with ultracold Rb, as was observed in our experiment (chapter 3, [58]). Therefore, after a variable interaction time t_I, in which both species are stored in the common running wave crossed dipole trap, the Rb cloud is pushed out of the trap with a resonant light pulse. This light pulse does not affect Cs, no influence on the survival probability is observed. After that push-out, the MOT can be employed to recapture and count the Cs atoms.

The production of the ultracold Rb gas takes about one minute in our experiment, roughly half a minute for loading the UHV-MOT and another half a minute for evaporative cooling. Typically, about two impurity atoms are inserted into the buffer gas on average. Hence the data acquisition rate is limited to the result of experiments with about two atoms per minute. To obtain data with reasonable statistical sigificance, the experiment has to be repeated sufficiently frequent. For achieving an uncertainty of $\approx \pm 5\%$ at a total survival probability of 50%, experiments with 120 atoms are necessary, which requires about 60 minutes measurement time (see Eq. 2.4). For higher and for lower survival probabilities, the uncertainty decreases slightly faster. Overall, measuring the temperature of the Cs impurity atom *once* with the resolution like shown in this thesis takes about 10 hours. The challenge here is to get the apparatus running stably and reproduceably over such long times. Accordingly, monitoring of the buffer gas is required. Because both subsystems are necessarily stored in a common trap, standard time-of-flight imaging of the Rb buffer gas unevitably removes also the Cs impurity atoms from the trap.

Therefore, the Rb push-out beam is employed to obtain absorption images of the Rb cloud in the trap in each shot. However, the information obtained by these images has to be interpreted with care. Because these images are taken in trap, it is not possible to extract information about the momentum distribution and therefore the temperature of the gas. Due to the small size of the sample (below the optical resolution of the imaging system), the atom number can only roughly be estimated. However, this is sufficient for a check if the apparatus is running well. Furthermore, the relative change in the number of the Rb atoms can be determined, despite a constant systematic error.

To get reliable quantitative parameters for the Rb sample, independent time-of-flight measurements with otherwise identical conditions are performed. In these shots, Cs can not be recaptured and is completely lost. The obtained parameters for the buffer gas are checked from time to time while running interspecies interaction experiments. The properties of the buffer gas are determined from the averaged time-of-flight measurements. Here, the Rb temperature is observed to have a good reproducibility. This can be expected due to the fact that the achieved temperature is mainly determined by evaporative cooling, which itself is governed by the well controlled magnetic and optical potentials. The Rb atom number depends on many more parameters and is therefore much more prone to fluctuations, which is also observed in the experiment. Due to our limited monitoring capability of the buffer gas during most shots of a typical experimental run, the error of the atom number is estimated to be 20% in the following.

The conditions for Cs, other than the interaction time t_I, in any of these experiments, are held constant. For instance, the storage time of Cs is always held at the same time, typically at one second. The reduction of survival probability without Rb is constant and on the order of a few percent. Any mechanisms that affect Cs when stored without Rb, like collisions with background gas atoms and loss due to transfer, are thus constant for all interaction times. The experiment is therefore only sensitive to the interspecies interaction.

4.2.3 Thermalization of Cs in the hyperfine ground state

To study the sympathetic cooling of Cs, a Rb sample is prepared in the $|1,0\rangle$ state. The properties of the Rb sample are measured independently by time-of-flight experiments, yielding an average atom number of $N_\mathrm{Rb} \approx 12.000$ and a temperature of $T_\mathrm{Rb} = (250 \pm 50)$ nK. The error of the atom number is assumed to be 20%. Subsequently, the ultracold Rb gas is doped with single Cs atoms prepared in the $F = 3$ hyperfine manifold. For varying interspecies interaction times t_I, the temperature

of Cs is measured with the release and recapture method.

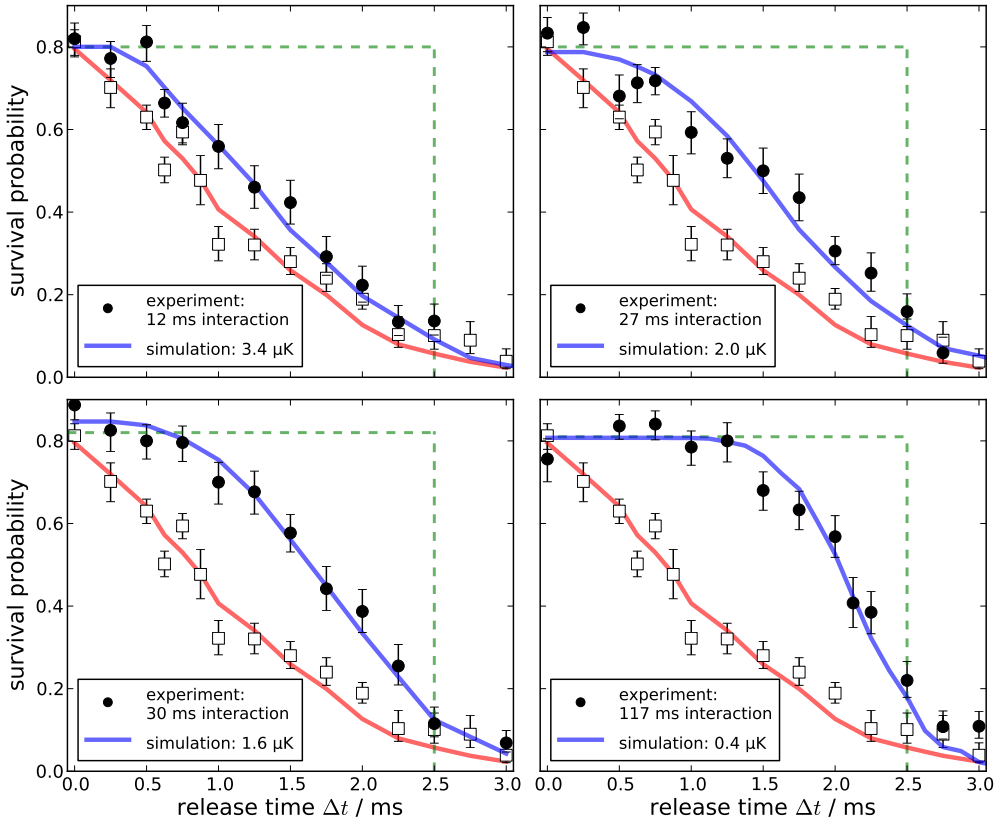

Figure 4.3: Thermometry of single Cs atoms interacting with an ultracold Rb gas. For increasing interaction time t_I, a release and recapture measurement is performed (●). The solid line shows the simulation corresponding to the temperature that reproduces the experiment best (blue solid line). For reference, the data without Rb present is plotted (□, red solid line). The green dashed line indicates the limit for atoms with vanishing initial velocity, for details see text.

In Fig. 4.3 the results are presented, for reference the release and recapture measurement for Cs without Rb is plotted. Already for short t_I, at the same release time Δt the survival probability is slightly enhanced. Accordingly, for longer Δt the slope of the decay increases. For the longest interaction time $t_\mathrm{I} = 117$ ms, the shape of the decay is changed drastically. The trap can be extinguished for as long as 1.4 ms without any reduction in the survival probability. At longer release time, the decay is correspondingly much steeper.

This observation can be understood by the cooling of Cs deep into the trap. The ultimate limit for the release time is given by gravity. An atom at $v = 0$ initially stored in the center of the trap needs $\Delta t_\mathrm{l} \approx \sqrt{2w_{\mathrm{Ti:Sa}}/g} \approx 2.5$ ms to leave the

trapping volume. In this simple picture, the survival probability is constant for $\Delta t < \Delta t_\mathrm{I}$ and then drops abruptly to zero. In Fig. 4.3 this limit is plotted as a green dashed line. For atoms with a finite temperature, this decay is smeared out towards a smaller survival probability.

In the same manner like above, the simulation with the temperature that fits the experimental data best, is determined. For all interaction times, the simulation is shown in Fig. 4.3 as a solid blue line. The agreement is reasonable, the change of the shape of the decay is reproduced by the simulation. With the help of the simulation, the absolute value of the temperature of Cs is extracted from all data sets, discussed in more detail below. The release and recapture measurement for the longest interaction time comes already quite close to the ultimate limit discussed above. In this regime, the dynamic range of this technique is mostly used up.

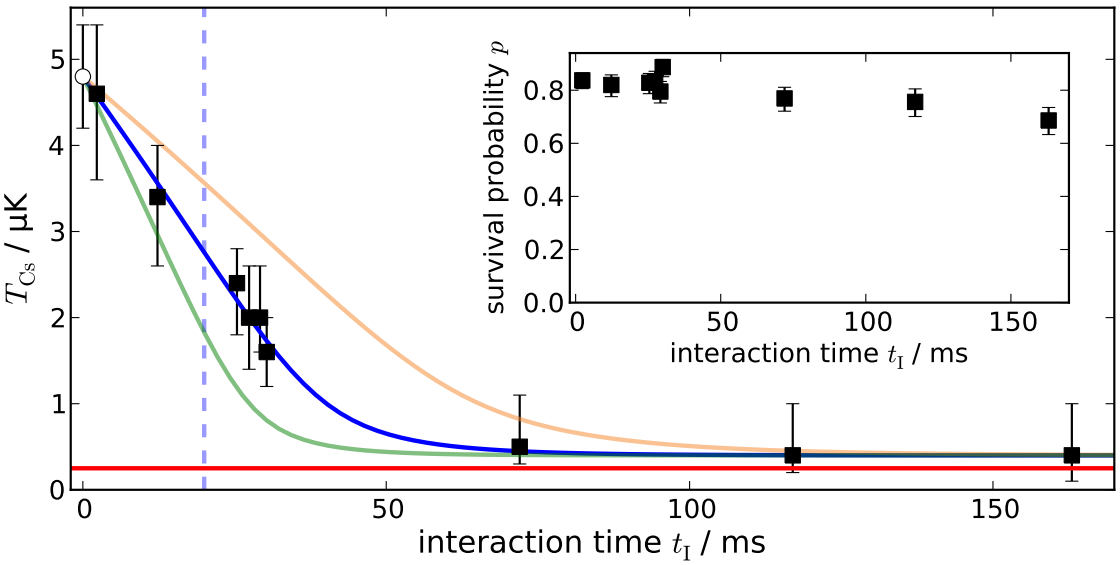

Figure 4.4: Thermalization of single Cs atoms. **Main graph:** Cs is cooled from its initial temperature of $T_\mathrm{Cs,initial} \approx 4.8$ µK to $T_\mathrm{Cs,final} \approx 0.4$ µK within a few tens of ms. The final temperature $T_\mathrm{Cs,final} \approx 0.4$ µK is compatible within the uncertainty to the temperature of the Rb buffer gas $T_\mathrm{Rb} \approx 0.25$ µK, as determined independently by time-of-flight velocimetry (red solid line). The blue solid line indicates the sympathetic cooling corresponding to the model as described in the text for an scattering length of $|a_\mathrm{RbCs}| = 450\ a_0$ (blue line). For comparison, the green (orange) solid line shows the expected cooling for $|a_\mathrm{RbCs}| = 550\ a_0$ ($|a_\mathrm{RbCs}| = 350\ a_0$). The dashed line indicates the time at which the lattice is completely extinguished. For details see text. **Inset:** Lifetime of the Cs atoms during sympathetic cooling, taken from the same data.

In Fig. 4.4 the cooling of the Cs immersed in the Rb cloud is presented. From the initial temperature of about 4.6 µK Cs is cooled in about 50 ms close to the temperature of the Rb gas of $T = (250 \pm 50)$ nK, as determined by time-of-flight velocimetry. Within the uncertainty, the temperature of both species is the same. This consistency check confirms the methods used to measure the temperature of single Cs atoms.

The survival probability of the impurity atom is found to be only slightly reduced during the sympathetic cooling (inset of Fig. 4.4). One reason for this loss is interspecies three-body recombination. Due to the relatively high photon scattering rate of $\Gamma_{\mathrm{Cs,dc}} \approx 9\ \mathrm{s}^{-1}$ and the small detuning of about 5 nm in the dichromatic running wave dipole trap, the Cs atom can also be transferred into the excited $F = 4$ hyperfine state, additionally opening an interspecies two-body loss channel. In the dichromatic dipole trap, a distinction between these loss channels is not directly possible. Therefore, both loss channels are studied in detail in section 4.3, where the photon scattering rate can be neglected.

The dashed line in Fig. 4.4 indicates the point where the lattice is completely extinguished. The cooling of the impurity atom is observed to start about 20 ms before this point. This can be understood by our loading sequence discussed in section 3.3. With a certain probability, Cs atoms are evaporated out of the lattice before the end of the lowering sequence. Therefore, the interspecies interaction takes place initially in the combined potential of running wave dipole trap and lattice. However, the lattice intensity at this point of the sequence is already below 3×10^{-3} of the initial intensity (see Fig. 3.3). Since a more detailed analysis of this effect as presented in section 3.3 would require more information about the insertion dynamics, the influence of this effect is neglected here and the interaction is assumed to start at $t \approx -20$ ms. The consequences for the determination of the scattering length are discussed in more detail below.

Another effect of our loading scheme is the off-center loading of the Cs impurity atoms. Initially, its trajectory in the trap will be strongly anisotropic. This could lower the probability of Cs interacting with Rb, which is stored in a small volume in the center of the trap. However, due to the coupling of the different axes because of gravity and trap inhomogeneities, the oscillation should quickly recover an isotropic trajectory. Additionally, after the first collision with Rb, the direction of the Cs trajectory is randomized. This is also supported by the temperature measurements, which assume a random phase-space distribution for the modeling.

Uncertainties of the temperature measurement of the Cs impurity atoms

To obtain a measure for the uncertainty of the temperature determination of the Cs atom, the least-square analysis is employed. For each simulated data set, corresponding to a certain temperature, χ^2 is calculated. Fig. 4.5(a) shows the release and recapture measurement for an interaction time of 29 ms, in Fig. 4.5(b) the obtained χ^2 for different simulated temperatures is plotted. The best fit occurs at $T = 2$ µK. As a measure for the uncertainty, the temperature is found at which χ^2 is increased by one [98]. The respective simulations showing this deviation are plotted in Fig. 4.5(a). Hence, the result in this example is a temperature of $T = (2.0 \pm 0.6)$ µK.

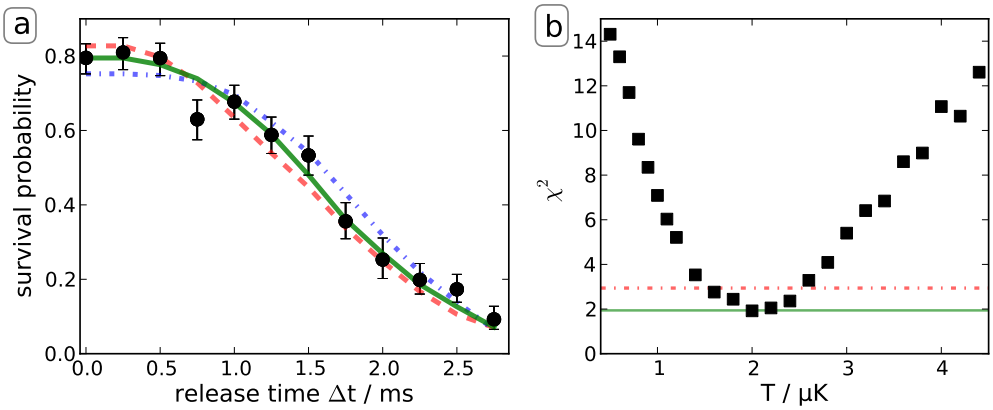

Figure 4.5: Error estimation of the temperature determined by the release and recapture measurement. **a)** Release and recapture experiment after an interaction time of 29 ms, taken from the data presented above. The green solid line indicates the simulation that fits the experiment best, corresponding to $T = 2$ µK. The error is estimated by the simulation, where χ^2 is increased by about one, plotted as red dashed line ($T = 2.6$ µK) and blue dash-dotted line ($T = 1.4$ µK). **b)** χ^2 of this data set for some simulated temperatures. The lowest χ^2 is indicated by the green solid line, the red dash-dotted line shows where χ^2 has increased by one.

Results: Scattering length

For a mixture of classical gases with a temperature difference ΔT, the average energy transfer can be written as $\dot{E} = \Gamma_{\mathrm{RbCs}} \cdot k_{\mathrm{B}} \cdot \Delta T \cdot \xi$, where Γ_{RbCs} is the interspecies collision rate and $\xi = 4m_1m_2/(m_1 + m_2)^2$ is the reduction factor due to the mass difference, in the case of a Rb-Cs mixture ξ =0.96 [87, 99, 100]. Here, the interactions are assumed to be in the collisionless regime, such that the elastic collision rate does not exceed the trap frequencies. This will be validated in the following analysis.

The change of the temperatures of the two components of the gas is given by

$$\begin{aligned} \dot{T}_{\mathrm{Rb}} &= \frac{\dot{E}_{\mathrm{Rb}}}{C_{\mathrm{Rb}}} \\ \dot{T}_{\mathrm{Cs}} &= -\frac{\dot{E}_{\mathrm{Cs}}}{C_{\mathrm{Cs}}} \end{aligned} \tag{4.10}$$

where $C_{\mathrm{Rb}} = 3N_{\mathrm{Rb}}k_{\mathrm{B}}$ and $C_{\mathrm{Cs}} = 3N_{\mathrm{Cs}}k_{\mathrm{B}}$ are the heat capacities of the harmonically trapped atoms. Hence the thermalization time constant can be expressed as [101, 102]

$$\tau_{\mathrm{therm}}^{-1} = -\frac{1}{\Delta T}\frac{d}{dt}\Delta T = \frac{\Gamma_{\mathrm{RbCs}}\xi}{3}\frac{N_{\mathrm{Rb}} + N_{\mathrm{Cs}}}{N_{\mathrm{Rb}}N_{\mathrm{Cs}}}. \tag{4.11}$$

In order to connect the thermalization rate to the microscopic interspecies cross section σ_{RbCs}, the density distributions $n_{\mathrm{Rb}}(\vec{r})$ and $n_{\mathrm{Cs}}(\vec{r})$ of the two species need to be taken into account. The collision rate can be written as

$$\Gamma_{\mathrm{RbCs}} = \sigma_{\mathrm{RbCs}}\bar{v}\int \mathrm{d}^3r\, n_{\mathrm{Rb}}(\vec{r})n_{\mathrm{Cs}}(\vec{r}), \tag{4.12}$$

where

$$\bar{v} = \sqrt{\frac{8k_{\mathrm{B}}}{\pi}\left(\frac{T_{\mathrm{Rb}}}{m_{\mathrm{Rb}}} + \frac{T_{\mathrm{Cs}}}{m_{\mathrm{Cs}}}\right)} \tag{4.13}$$

is the mean thermal relative velocity and the integral is a measure of the interspecies spatial overlap [101, 103]. Due to the different polarizabilities and masses of Rb and Cs, each species experiences a different potential depth and different trap frequencies. Table 4.2 summarizes these parameters.

The difference of the gravitational sag amounts to $\Delta = g(1/\omega_{\mathrm{Rb,x}}^2 - 1/\omega_{\mathrm{Cs,x}}^2) \approx 4$ µm, leading to slightly different trap centers for the two species. The spatial overlap is therefore reduced by a factor $\exp\left(-\frac{\Delta^2}{\rho_x^2}\right)$, where

$$\rho_x = \sqrt{\frac{2k_{\mathrm{B}}T_{\mathrm{Rb}}}{\omega_{\mathrm{Rb,x}}^2 m_{\mathrm{Rb}}} + \frac{2k_{\mathrm{B}}T_{\mathrm{Cs}}}{\omega_{\mathrm{Cs,x}}^2 m_{\mathrm{Cs}}}} \tag{4.14}$$

is the root-mean-square sum of the sizes of the clouds. In Fig. 4.6(a) the normalized overlap for the relevant temperatures is plotted. Due to the shrinking size of the trapping volume of Cs during the sympathetic cooling, the decrease of overlap caused

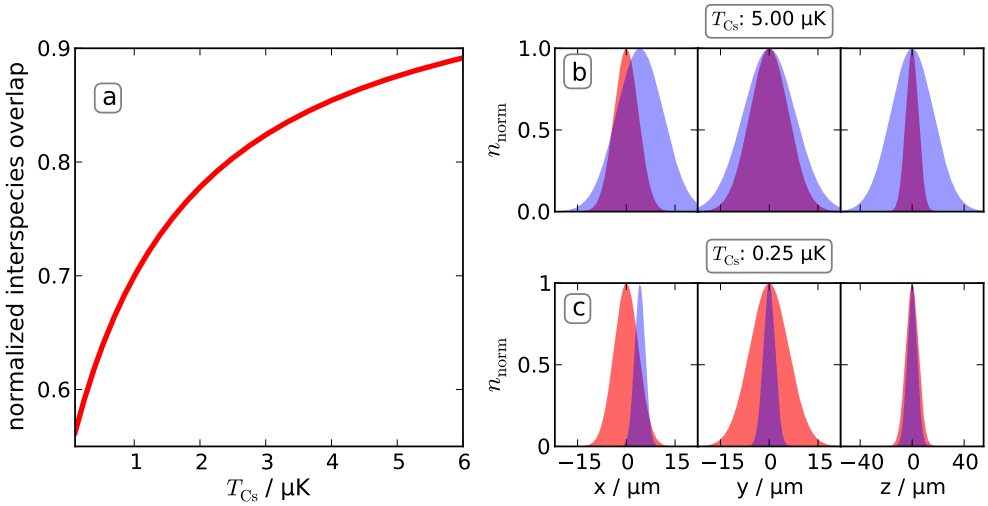

Figure 4.6: Temperature dependence of the effective interspecies interaction volume. **a)** Reduction of the spatial overlap due to gravitational sag in dependence of Cs temperature. **b) + c)** Shrinking trapping volume during the sympathetic cooling, plotted is the normalized density of Rb (red) and Cs (blue). The peak density of Rb amounts to $\approx 7 \times 10^{12}$ cm^{-3}, the peak density of Cs increases from initially $\approx 7 \times 10^{7}$ cm^{-3} to $\approx 6 \times 10^{9}$ cm^{-3} at the end of sympathetic cooling.

by the sag is enhanced from initially about 90% at $T_{\mathrm{Cs}} = 5$ µK to about 60% at $T_{\mathrm{Cs}} = 250$ nK. Fig. 4.6 gives an impression of the scales realized in the experiment.

While the sag reduces the interspecies overlap and accordingly the collision rate during the sympathetic cooling, the shrinking trapping volume of Cs strongly enhances the collision rate. This is described by the temperature dependent densities that are used to calculate the interspecies trapping volume. With the analytic solution of the integral expressed in terms of experimentally accessible parameters, we find the overall spatial overlap

$$\int \mathrm{d}^3 r n_{\mathrm{Rb}}(\vec{r}) n_{\mathrm{Cs}}(\vec{r}) = N_{\mathrm{Rb}} N_{\mathrm{Cs}} \left(2\pi k_{\mathrm{B}}\right)^{-\frac{3}{2}} \left[\frac{T_{\mathrm{Cs}}}{m_{\mathrm{Cs}}\omega_{\mathrm{Cs,x}}^2} + \frac{T_{\mathrm{Rb}}}{m_{\mathrm{Rb}}\omega_{\mathrm{Rb,x}}^2}\right]^{-\frac{1}{2}}$$
$$\times \left[\frac{T_{\mathrm{Cs}}}{m_{\mathrm{Cs}}\omega_{\mathrm{Cs,y}}^2} + \frac{T_{\mathrm{Rb}}}{m_{\mathrm{Rb}}\omega_{\mathrm{Rb,y}}^2}\right]^{-\frac{1}{2}} \left[\frac{T_{\mathrm{Cs}}}{m_{\mathrm{Cs}}\omega_{\mathrm{Cs,z}}^2} + \frac{T_{\mathrm{Rb}}}{m_{\mathrm{Rb}}\omega_{\mathrm{Rb,z}}^2}\right]^{-\frac{1}{2}} \exp\left(-\frac{\Delta^2}{\rho_x^2}\right). \quad (4.15)$$

For equal masses and trap frequencies (linear dependent trap frequencies) we reproduce the results of [100] ([102]). Summarizing the analysis outlined above, we obtain for the thermalization rate

$$\tau_{\text{therm}}^{-1} = \frac{\sigma_{\text{RbCs}}\xi(N_{\text{Rb}}+N_{\text{Cs}})\sqrt{\frac{8k_{\text{B}}}{\pi}\left(\frac{T_{\text{Rb}}}{m_{\text{Rb}}}+\frac{T_{\text{Cs}}}{m_{\text{Cs}}}\right)}}{3\left(2\pi k_{\text{B}}\right)^{\frac{3}{2}}\exp\left(\frac{\Delta^2}{\rho_x^2}\right)}\left[\frac{T_{\text{Cs}}}{m_{\text{Cs}}\omega_{\text{Cs,x}}^2}+\frac{T_{\text{Rb}}}{m_{\text{Rb}}\omega_{\text{Rb,x}}^2}\right]^{-\frac{1}{2}} \times\left[\frac{T_{\text{Cs}}}{m_{\text{Cs}}\omega_{\text{Cs,y}}^2}+\frac{T_{\text{Rb}}}{m_{\text{Rb}}\omega_{\text{Rb,y}}^2}\right]^{-\frac{1}{2}}\left[\frac{T_{\text{Cs}}}{m_{\text{Cs}}\omega_{\text{Cs,z}}^2}+\frac{T_{\text{Rb}}}{m_{\text{Rb}}\omega_{\text{Rb,z}}^2}\right]^{-\frac{1}{2}}. \tag{4.16}$$

Note that only the sum of the number of atoms of both species enters, so that the exact number of Cs atoms does not influence the determination of the scattering cross section significantly. This reflects the negligible heat capacity of the impurity atoms. The thermalization rate τ_{therm} depends on the spatial size and therefore on the temperature of both species. The heating of the Rb buffer gas ΔT_{Rb} caused by the sympathetic cooling of a single impurity Cs atom is given by

$$\begin{aligned}\Delta T_{\text{Rb}} &= \left(T_{\text{Rb,initial}} - T_{\text{Rb,final}}\right)\\ &= T_{\text{Rb,initial}} - \frac{N_{\text{Rb}}T_{\text{Rb,initial}} + N_{\text{Cs}}T_{\text{Cs,initial}}}{N_{\text{Cs}}+N_{\text{Rb}}} < 1\,\text{nK}\end{aligned} \tag{4.17}$$

and can clearly be neglected here. Furthermore, the atom number of the buffer gas is approximately constant (discussed in more detail in the next section), so that the properties of the Rb buffer gas remain effectively unaffected. Cs, in contrast, is cooled by more than one order of magnitude in temperature, causing the trapping volume to shrink significantly and leading to stronger interspecies interaction. It is therefore not sufficient to assume a single cooling time constant for the entire thermalization. Instead, the sympathetic cooling of Cs is calculated in discrete steps in an iterative approach for a fixed, energy independent scattering cross section σ_{RbCs}. Starting at $t_0 = 0$ with the initial Cs temperature $T_{\text{Cs,initial}}$, Eq. 4.16 is used to compute $\tau_{\text{therm},0}$. The temperature at $t_1 = t_0 + \Delta t$ is determined to be

$$T_{\text{Cs,t}_1} = \left(T_{\text{Cs,initial}} - T_{\text{Cs,final}}\right)\exp\left(-t/\tau_{\text{therm},0}\right) + T_{\text{Cs,final}} \tag{4.18}$$

where $T_{\text{Cs,final}}$ is the final temperature of Cs. With the new temperature $T_{\text{Cs,t}_1}$ the new thermalization time constant is calculated, and the next step of the thermalization is computed. This is repeated with sufficiently short time steps to the desired extend in time. In this way, the sympathetic cooling is described with a time constant that is itself time-dependent.

Fig. 4.4 shows the result of this calculation that best fits the experiment, corresponding to a scattering cross section of

$$\sigma_{\mathrm{RbCs}} \approx 7.4 \times 10^{-11}\mathrm{cm}^2. \tag{4.19}$$

From the scattering cross section σ_{RbCs} the corresponding s-wave scattering length is calculated to be

$$|a_{\mathrm{RbCs}}| = \sqrt{\sigma_{\mathrm{RbCs}}/4\pi} \approx 450\, a_0 \tag{4.20}$$

where a_0 is the Bohr radius. The agreement with the experiment is reasonable. For comparison, the model for sympathetic cooling is also plotted for a scattering length of $|a_{\mathrm{RbCs}}| = 550\ a_0$ (green solid line) and $|a_{\mathrm{RbCs}}| = 350\ a_0$ (orange solid line). Both cases feature a significant deviation, so that the uncertainty, without considering systematic errors, can be estimated to be on the order of $\pm 50\ a_0$. Since only the hyperfine state of Cs is controlled in this experiment, the impurity atoms are distributed across all Zeeman sublevel. The scattering cross section is therefore the effective value including all Zeeman sublevels within the $F = 3$ hyperfine manifold of Cs. Additionally, our experiment is not sensitive for the sign of the scattering length.

At the determined scattering cross section, the thermalization time constant decreases during the cooling from initially $\tau_{\mathrm{therm,initial}} \approx 44$ ms to $\tau_{\mathrm{therm,final}} \approx 16$ ms. Accordingly, the interspecies collisions rate per Cs atom increases from initially $\Gamma_{\mathrm{RbCs,initial}}/N_{\mathrm{Cs}} \approx 70\ \mathrm{s}^{-1}$ to $\Gamma_{\mathrm{RbCs,final}}/N_{\mathrm{Cs}} \approx 200\ \mathrm{s}^{-1}$ at the end of the sympathetic cooling, despite the effect of the gravitational sag. This underlines the need of assuming τ_{therm} to be temperature and therefore time-dependent.

The highest possible thermalization rate is reached, when the collisional dynamics enter the hydrodynamic regime. This happens when the elastic collision rate exceeds the frequencies of the trap by far. In this case, the thermalization rate is limited by the trap frequencies, since local thermal perturbations can not spread across the sample faster than the trap frequencies [104–107]. In our case, the radial trap frequencies are at least a factor of two higher even at the lowest reached temperatures, whereas the axial trap frequency is on the order of the elastic collision rate only at the end of the thermalization, when both species are almost in thermal equilibrium. Therefore, the cooling dynamics can be described in the collisionless regime and the assumption in the derivation of Eq. (4.11) is justified.

In a thermalization experiment in a magnetic trap, in a nearly balanced Rb-Cs

mixture (Rb: $|1,-1\rangle$, Cs: $|3,-3\rangle$) at temperatures of several 10 µK, the scattering length was measured to be $|a_{\mathrm{RbCs}}| \approx 595\ a_0$ [108]. In our group, from the sympathetic cooling dynamics in the magnetic trap (Rb: $|2,2\rangle$, Cs: $|4,4\rangle$) a lower limit of $|a_{\mathrm{RbCs}}| \geq 150\ a_0$ was deduced [55]. Recently, magnetic field spectroscopy of a mixture with both species in the ground state yielded $a_{\mathrm{RbCs}} = +(630 \pm 60)\ a_0$ [109].

In the light of our insertion sequence, the derived value for the interspecies scattering length should be regarded as a lower limit. Nevertheless, the interspecies interaction is very strong for our species combination. The impurity atom is cooled rapidly below one µK, with only a few percent lifetime decay (see Fig. 4.4). The temperature of the impurity atom is given by the temperature of the buffer gas, which could easily be cooled further into the degenerate regime. During the sympathetic cooling, the impurity atom becomes tightly localized, enhanced by the species selective trap, causing the density to increase by about two orders of magnitude. The buffer gas remains completely unaffected by the sympathetic cooling. Despite the differential gravitational sag, already with this first easy experimental realization the doping of the Rb gas with a strongly interacting, tightly localized impurity atom is achieved.

4.3 Inelastic collisions – Two-body and three-body losses

The limit of the lifetime of the impurity atom is given by inelastic collisions with atoms of the buffer gas. Depending on the internal state of both species, inelastic two-body and three-body collisions are possible.

The main experimental challenge for measuring three-body recombination is to distinguish three-body losses from two-body losses. In magnetic traps, this is difficult in general, because dipolar relaxation is present as an inherent two-body loss mechanism. When both species are stored in an optical dipole trap in their absolute ground state, the only remaining loss channel is a three-body collision [44, 110].

In the following, the lifetime of the impurity atom is studied with both species prepared in the absolute ground state. Owing to the atomic resolution for Cs, three-body recombination is observed atom-per-atom and event-by-event. Again, the buffer gas is unaffected by the probing with the Cs atom. The timescale of the losses is on the order of hundreds of ms. The timing behavior of the insertion sequence, as discussed in the framework of the sympathetic cooling, can therefore be neglected here. Finally, in the last section the decay of Cs in the excited hyperfine state due to inelastic two-body collisions is presented.

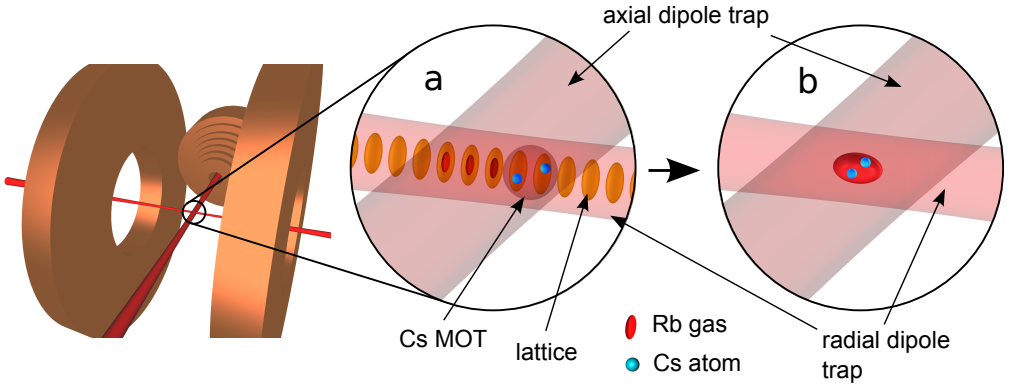

Figure 4.7: Illustration of the setup for the monochromatic running wave dipole trap, as used in this section (not to scale). **a)** Loading single Cs atoms into the MOT with Rb stored (see also Fig. 3.1(b)). **b)** Interaction of both species in the monochromatic running wave dipole trap, consisting of axial dipole trap and radial dipole trap (see also Fig. 3.1(d)).

4.3.1 Experimental techniques for the realization of three-body loss experiments

All experiments in this section use the monochromatic crossed dipole trap, where the axial dipole trap and the radial dipole trap are combined. Fig. 4.7 illustrates the setup in this configuration. This ensures that the photon scattering rate can be neglected for the relevant time scale (see Fig. 3.7). Furthermore, the confinement of both species after thermalization is nearly equal in this case (see Fig. 4.8(c)), so that it is sufficient to assume the same, common trapping volume for both species, simplifying the analysis.

To facilitate an unambiguous interpretation of the loss channels, the Rb buffer gas should be solely prepared in the absolute ground state ($|1,1\rangle$). During the insertion

	radial	axial	Ti:Sa running wave
Rb depth/k_B (µK)	27	27	0
Cs depth/k_B (µK)	48	48	0
Wavelength (nm)	1064	1064	899.93
Waist (µm)	48	100	31
Rb rad. freq. (Hz)	326	160	-
Rb ax. freq. (Hz)	2	<1	-
Cs rad. freq. (Hz)	365	172	-
Cs ax. freq. (Hz)	2	<1	-

Table 4.3: Parameters of the traps for inelastic collision experiments.

sequence of single Cs atoms, Rb is transferred with a π-pulse from the $|1,1\rangle$ state into the $|1,0\rangle$ state. This is necessary to employ the magnetic field for the Cs MOT, as discussed in detail in chapter 3. For this experiment, with both species stored in the lattice, the same π-pulse is applied a second time to transfer the Rb gas back into the $|1,1\rangle$ state. To avoid any admixture of Rb atoms remaining in the $|1,0\rangle$ state, subsequently a microwave pulse with a duration of typically 40 ms resonant to the transition $|1,0\rangle \rightarrow |2,-1\rangle$ is applied. In this way, any Rb atom left in the $|1,0\rangle$ state will eventually be transferred into the $|2,-1\rangle$ state, where it is removed by a push-out pulse resonant to the $F = 2 \rightarrow F' = 3$ transition.

Accordingly, Cs is optically pumped into the desired state ($|3,3\rangle$ or $F = 4$) before being immersed in the Rb cloud. Then, both species are brought into contact and are stored in the running wave dipole trap for a varying interaction time t_{I}. During the hold time in the dipole trap, a homogeneous offset field of ≈ 800 mG is applied to provide a quantization axis. In Table 4.3 the parameters of the traps in this experiment are summarized. Finally, Rb is pushed out of the trap and the number of surviving Cs atoms is counted.

4.3.2 Three-body recombination with atomic resolution

To study the interspecies three-body recombination, single Cs atoms prepared in the $|3,3\rangle$ state are immersed in a Rb buffer gas containing on average $N_{\mathrm{Rb}} \approx 21.000$ atoms prepared in the $|1,1\rangle$ state at a temperature of $T_{\mathrm{Rb}} = (700 \pm 50)$ nK. The error of the atom number is assumed to be 20%.

Fig. 4.8 shows the results, averaged over shots with 1 – 4 Cs atoms initially immersed in the buffer gas. From the survival probability of about 80% due to losses during the insertion, the survival probability for the impurity atoms decays with a time constant of $\tau_{L_3} = (732 \pm 47)$ ms. At the same time, the Rb buffer gas does not show a significant loss of atoms. This is in agreement with the expected lifetime due to intraspecies three-body recombination of Rb in this state (see Table 4.4, [111]) and the decay of lifetime due to collisions with the background gas, which is measured independently with a time constant of $\tau_1 \approx 160$ s. Both effects lead to the theoretical lifetime plotted as a solid red line in Fig. 4.8(a). The effect of the small number of interspecies three-body collisions on the Rb gas can obviously be neglected completely. This implies that the density of Rb, which determines the interspecies interaction dynamics, is effectively constant during the whole interaction time.

From the same data, the loss rate can be inferred for an exactly defined number of impurity atoms by selecting the experimental shots with the respective atom

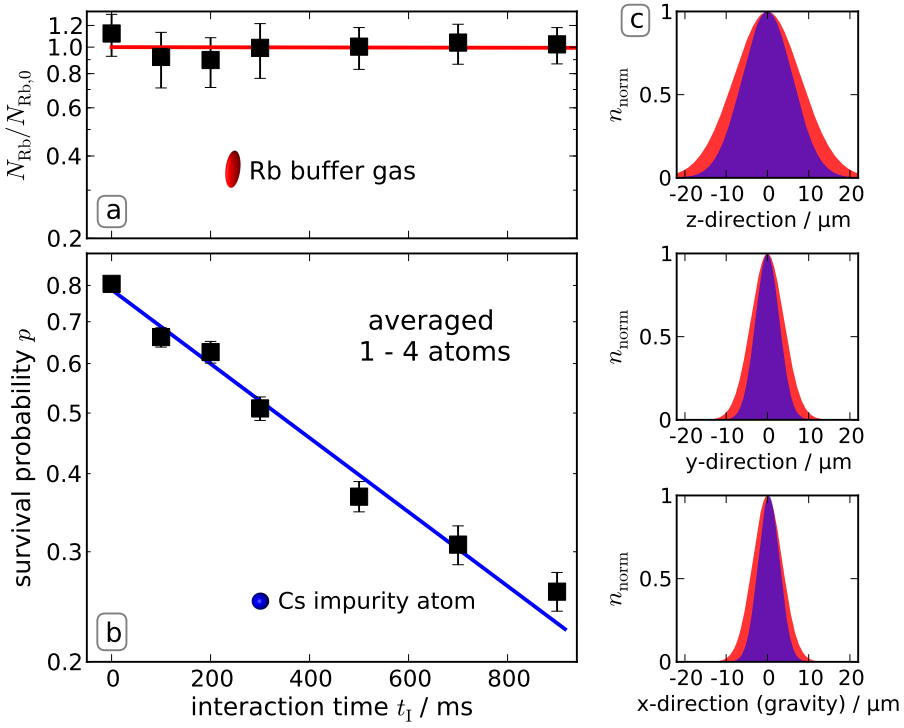

Figure 4.8: Three-body recombination of impurity atoms with atoms of the buffer gas. **a)** During the interaction, the buffer gas does not experience any loss of atoms in the relevant time. The red line is the expected decay, taking into account the known intraspecies three-body loss rate for Rb (see Table 4.4, [111]) and the decay of lifetime due to collisions with background gas atoms, in our case given by $\tau_1 \approx 160$ s. **b)** Decay of 1 – 4 Cs impurity atoms immersed in the ultracold Rb gas, showing an exponential time constant of $\tau_{L_3} = (732 \pm 47)$ ms. **c)** Normalized density distribution of both species in the trap after thermalization (Rb: red, Cs: blue). The peak density of Rb (Cs) amounts to 1.2×10^{13} cm^{-3} (1.4×10^{9} cm^{-3}).

number. In Fig. 4.9(a–d) the decay is shown for exactly 1, 2, 3 and 4 atoms initially immersed in the buffer gas, respectively. For each data set, the fit of the averaged data is plotted to provide a comparison. The decay rate for all atom numbers as well as the average data set agrees within the uncertainty.

In an approximately balanced mixture, potentially all possible combinations (Rb-Rb-Cs, Cs-Cs-Rb, Cs-Cs-Cs) cause Cs loss due to three-body recombination. The knowledge of the exact number of impurity atoms allows to constrain the possible loss channels, as illustrated in Fig. 4.9. For a single Cs atom, for instance, only Rb-Rb-Cs three-body recombination remains. Accordingly, for two impurity atoms Cs-Cs-Cs collisions are impossible, whereas for three and four impurity atoms all

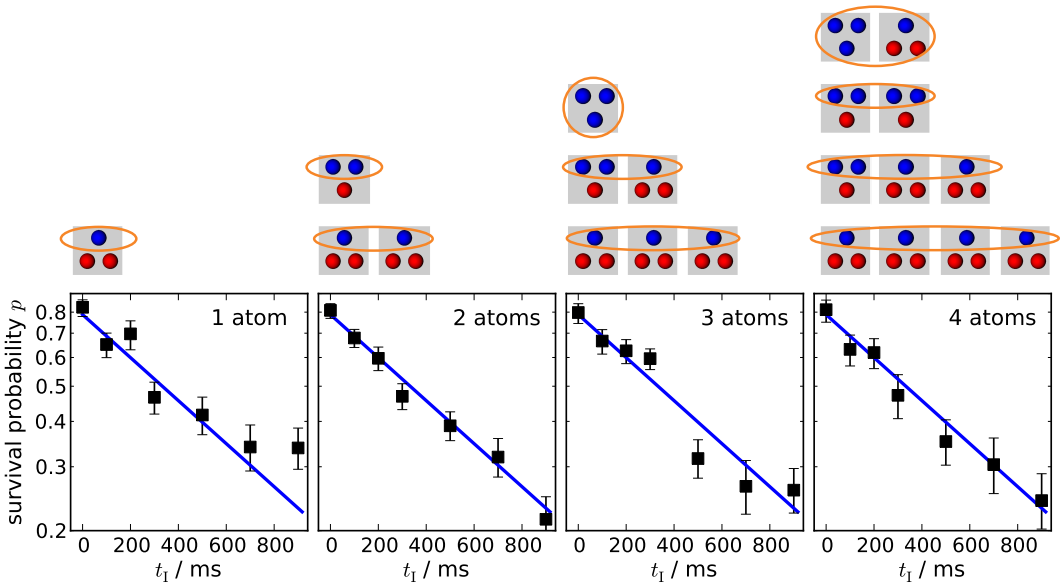

Figure 4.9: Three-body losses observed atom-by-atom. **Lower row:** For all impurity atom numbers from one to four, the data can be described by a simple exponential decay with the same time constant determined from the average data of Fig. 4.8. **Upper row:** Illustration of the possible loss channels corresponding to the impurity atom number. Blue (red) spheres represent Cs (Rb) atoms.

loss channels are allowed. The fact that all decay rates for 1 – 4 impurity atoms are the same, points to Rb-Rb-Cs three-body recombination as the only relevant loss channel in our experiment.

This can be verified by looking one step closer at the statistics of the losses, which are also resolved by our experiment. There are three possible outcomes of a single experiment of immersing two impurity atoms in the buffer gas: Two atoms, one atom or no atom may be lost. These cases are easily identified by the fluorescence traces after recapture, examples are presented in Fig. 4.10(a). From many experimental realizations, the respective probabilities p_0 (no atom lost), p_1 (single atom loss) and p_2 (two atoms loss) are determined for each interaction time t_I, corresponding to a certain total survival probability p.

Assuming the same, independent survival probability p for each Cs atom, the probability for each of these cases can be written as

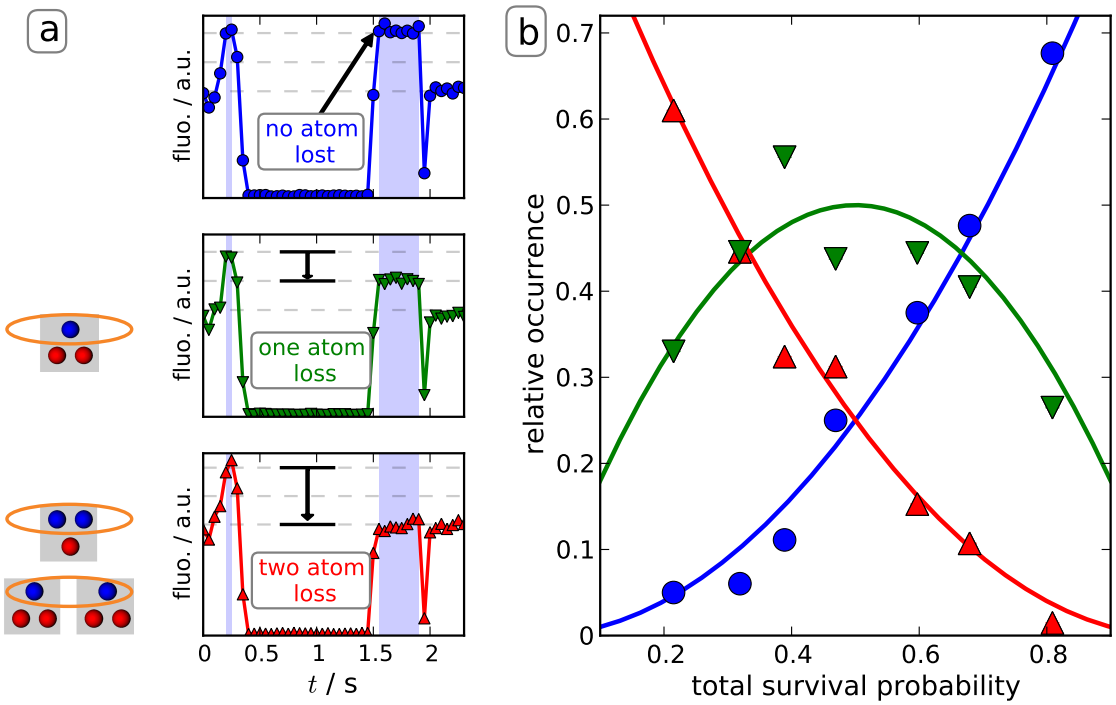

Figure 4.10: Three-body losses for exactly two impurity atoms, observed event-by-event. **a)** Fluorescence traces showing all three possible loss events and the according allowed loss channels. **b)** Corresponding relative occurrences for all possible case: two atom loss (▲), one atom loss (▼) and no atom loss (●). The solid lines show the expectation according to Eqs. (4.21).

$$\begin{aligned} p_0 &= p^2 \\ p_1 &= 2p(1-p) \\ p_2 &= (1-p)(1-p). \end{aligned} \tag{4.21}$$

If there was any inelastic loss process involving two Cs atoms (Cs-Cs-Rb three-body recombination), the probability p_2 that both Cs atoms are lost from the trap would be increased compared to the probability p_1 of a single atom loss and to the probability p_0 that no atom is lost. In Fig. 4.10 the expectation according to Eqs. (4.21) is plotted together with the corresponding relative occurrences obtained from the experiment, showing a good agreement. It is therefore solely Rb-Rb-Cs three-body recombination, which leads to the observed decay rate.

Results: Three-body loss rate

In a three-body recombination, the released binding energy is shared among the colliding atoms. Depending on the trap depth and the gained energy, the atoms leave the trap. However, a part of the energy can be transferred to the remaining atoms of the gas, leading to heating of the whole sample. Because the probability of three-body recombination depends quadratically on the density of the buffer gas, this effect happens predominantly in the cold and dense parts of a cloud in the center of the trap. Since it removes colder atoms with higher probability, this effect is called "anti-evaporation" [44]. In our case, the small number of collision events allows neglecting this effect. Indeed, no significant heating of the Rb gas is observed. This further facilitates the interpretation of the lifetime measurement.

The decay of lifetime of Cs immersed in the Rb gas can be described by

$$\frac{1}{N_{\mathrm{Cs}}}\frac{dN_{\mathrm{Cs}}}{dt} = \frac{\dot{N}_{\mathrm{Cs}}}{N_{\mathrm{Cs}}} = -L_3 <n_{\mathrm{Rb}}^2> \tag{4.22}$$

where $<n_{\mathrm{Rb}}^2>$ is the mean squared Rb density and L_3 the three-body loss coefficient. Usually, both Cs atom number and Rb density are time dependent, so that Eq. 4.22 can in general not be solved analytically. In our case, in contrast, $<n_{\mathrm{Rb}}^2>$ is constant (see Fig. 4.8), so that Eq. 4.22 is solved by $N(t) = N_0 \exp(-t/\tau_{L_3}) = N_0 \exp(-L_3 <n_{\mathrm{Rb}}^2> t)$. This is also validated by the experimental data being well described by an exponential decay (see Fig. 4.8). Expressing the mean squared density of Rb by the directly observed quantities N_{Rb} and T_{Rb}, the three-body loss rate L_3 can be inferred from the measured decay time τ_{L_3} by

$$L_3 = \frac{1}{\tau_{L_3}} \left(\frac{2\pi k_{\mathrm{B}} \sqrt{27}}{m_{\mathrm{Rb}} \bar{\omega}_{\mathrm{Rb}}^2} \right)^3 \frac{T_{\mathrm{Rb}}^3}{N_{\mathrm{Rb}}^2} \tag{4.23}$$

where $\bar{\omega}_{\mathrm{Rb}}$ is the geometric mean of the trap frequencies of Rb. With the decay time and the experimental parameters, Eq. 4.23 yields

$$L_3 = (5 \pm 2) \times 10^{-26}\,\mathrm{cm^6 s^{-1}}. \tag{4.24}$$

Here, the error includes uncertainties of T_{Rb}, τ_{L_3} and N_{Rb}. The main contribution to the error comes from the uncertainty of N_{Rb}.

In other experiments working with Rb-Cs mixtures, the three-body loss coefficient was measured with (nearly) balanced mixtures. Due to the difficulties to extract

	^{87}Rb			^{133}Cs
$\|F, m_F\rangle$	$\|2,2\rangle$ (BEC)	$\|1,1\rangle$ (BEC)	$\|1,-1\rangle$ (BEC)	$\|3,3\rangle$
L_3 (cm^{6}s^{-1})	1.8×10^{-29} [112]	3×10^{-29} [111]	5.8×10^{-30} [113]	$\approx 10^{-24}$ [44]

Table 4.4: Intraspecies three-body loss rates for some states of ^{87}Rb and ^{133}Cs in thermal clouds and BECs at low magnetic fields.

the pure loss coefficient in this case as discussed above, these groups give a rather rough estimation of $L_3 \approx (10^{-25} - 10^{-26})$ cm^{6}s^{-1} [114] and $L_3 < 10^{-25}$ cm^{6}s^{-1} [109]. Our results are compatible to these findings, which implies that Rb-Rb-Cs three-body recombination is the reason for a significant fraction of the losses observed in balanced Rb-Cs mixtures.

For comparison, in Table 4.4 intraspecies three-body loss coefficients for some states of Rb and Cs are summarized. For Rb, the loss rate is suppressed by about two orders of magnitude, which facilitates the use of this species as the "workhorse" species in ultracold atom experiments. For Cs, in contrast, the loss rate at low magnetic fields in the absolute ground state is about two orders of magnitude higher than the interspecies rate. Cs in the ground state features a Feshbach resonance close to zero magnetic field, which makes the interaction strongly dependent on the external magnetic field already at low field strengths [92, 105, 115]. Since the three-body loss rate coefficient scales with the fourth power of the interaction strength a (see Eq. 4.8), this also drastically changes the three-body recombination rate. Overall, this makes Cs gases difficult to handle. Bose-Einstein condensation of Cs, for instance, was achieved only in optical traps with samples in the absolute ground state and by tuning the interaction strength [105, 116].

The three-body recombination coefficient for Rb-Cs mixtures lies in between these two cases. Combined with the challenges of single species Cs gases, in balanced mixtures the relatively high interspecies three-body loss rate leads to quite demanding experimental requirements [109, 114]. It is not possible to tune interactions to a region where all Rb-Rb, Rb-Cs and Cs-Cs interaction strength are reasonably small, in fields of up to 667 G, as has been reported lately [109]. Only recently, double BECs of Rb and Cs have been produced [109, 117], in one case by merging ultracold clouds prepared in separated traps to avoid strong losses due to interspecies collisions [109].

In our experiment, in contrast, there are no Cs-Cs interactions, as was discussed in this section, while the Cs impurity atoms interact strongly with the Rb buffer gas. Accordingly, the employment of Feshbach resonances to tune the interspecies interaction is not limited to magnetic fields where Cs-Cs losses are low. Without

tuning the interspecies interaction, evaporative cooling of the Rb gas with Cs atoms immersed is limited to a few 100 ms. However, with the sequence presented in chapter 3, Rb can be cooled independently to the desired temperature before Cs is inserted. Since the thermalization due to elastic collisions is much faster than the decay of lifetime due to three-body collisions, the lifetime of the impurity atom is sufficiently long for future experiments.

By using few and single atoms as probes, the interspecies three-body loss rate was determined without affecting the Rb buffer gas. The decay in lifetime can be traced back to a single loss channel, allowing an unambiguous estimation of the three-body loss coefficient.

4.3.3 Two-body loss rate in the excited hyperfine state of Cs

To experimentally investigate the effect of two-body collisions in the "excited" hyperfine ground state, Cs is pumped into the $F = 4$ hyperfine manifold, with an otherwise identical experimental sequence like in the preceding section. For a direct comparison, the lifetime measurement for Cs in the absolute ground state is repeated. The Rb atom number in this experiment is about $N_{\mathrm{Rb}} \approx 19.000$, slightly lower than in the preceding L_3 measurement. The uncertainty of the atom number is assumed to be 20%. The temperature of the Rb gas is $T_{\mathrm{Rb}} = (700 \pm 50)$ nK, the trap parameter are the same as listed in Table 4.3.

Fig. 4.11 shows the experimental results. The loss is again well described by a simple exponential decay. For Cs in the absolute ground state, the survival probability decays with a time constant of $\tau_{L_3} \approx 900$ ms, slightly slower compared to section 4.3.2 due to the lower Rb density. For atoms in the excited hyperfine state, the decay shows a much faster time constant of $\tau_{L_2} = (111 \pm 10)$ ms.

Like in the case discussed in the preceding section, heating and atom loss in the Rb gas can be neglected, so that the properties of the buffer gas are constant during the interaction with Cs. The amount of internal energy (about 9.2 GHz) is extremely large compared to the trap depth. When it is released in a collision with an atom of the Rb buffer gas, both atoms involved leave the trap.

Assuming the loss to be caused solely by two-body collisions, the lifetime of the impurity atom can be described by

$$\frac{1}{N_{\mathrm{Cs}}}\frac{dN_{\mathrm{Cs}}}{dt} = \frac{\dot{N}_{\mathrm{Cs}}}{N_{\mathrm{Cs}}} = -L_2 <n_{\mathrm{Rb}}> \tag{4.25}$$

where $<n_{\mathrm{Rb}}>$ denotes the mean density of the Rb gas. Like in the case of the

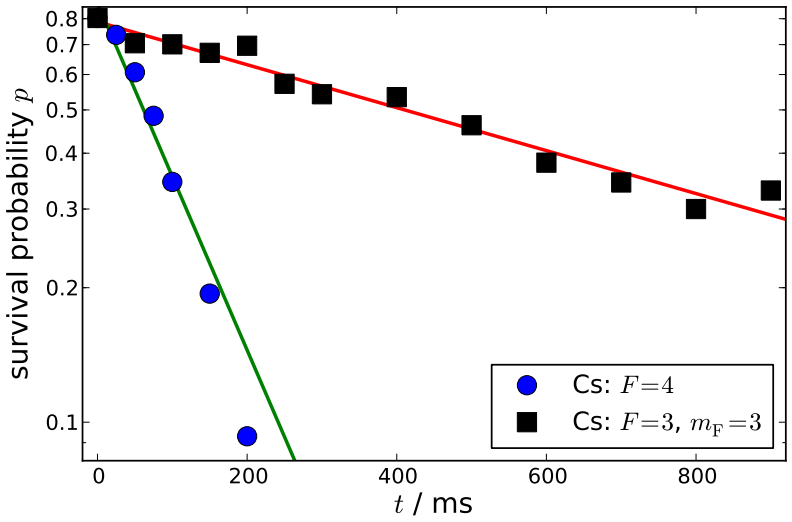

Figure 4.11: Lifetime for on average about 10 Cs atoms prepared in the absolute ground state ($F = 3$, $m_F = 3$ (■)) and in the excited hyperfine state ($F = 4$ (●)) immersed in an ultracold Rb gas. The statistical errors are on the order of the markersize and therefore not shown.

three-body collisions discussed in the preceding section, this equation is solved with a simple exponential decay $N_0 \exp(-t/\tau_{L_2}) = N_0 \exp(-L_2 <n_{\mathrm{Rb}}> t)$. Expressing L_2 in experimentally directly accessible quantities, we get

$$L_2 = \frac{1}{\tau_{L_2} N_{\mathrm{Rb}}} \left(\frac{4\pi k_{\mathrm{B}} T_{\mathrm{Rb}}}{m_{\mathrm{Rb}} \bar{\omega}_{\mathrm{Rb}}^2} \right)^{\frac{3}{2}}. \tag{4.26}$$

With the experimental parameters, this yields for the interspecies two-body loss rate coefficient

$$L_2 = (3 \pm 1) \times 10^{-12}\,\mathrm{cm^3 s^{-1}}. \tag{4.27}$$

	^{87}Rb		^{133}Cs	
$\lvert F, m_F \rangle$	$\lvert 2,2 \rangle$ (BEC)	$\lvert 1,-1 \rangle$ (BEC)	$\lvert 4,4 \rangle$	$\lvert 3,-3 \rangle$
L_2 ($\mathrm{cm^3 s^{-1}}$)	1×10^{-15} [112, 118]	1×10^{-15} [112, 118]	4×10^{-12} [119]	4×10^{-13} [120]

Table 4.5: Intraspecies two-body loss rates for ^{87}Rb and ^{133}Cs for some states, that can be trapped magnetically.

In Table 4.5 the corresponding intraspecies two-body loss rate coefficient for Rb and Cs are listed. Compared with the determined interspecies loss rate, two-body losses

in Rb gases are strongly suppressed by about three orders of magnitude, which is one of the reasons why Rb is very well suited to study high density clouds and BECs. For Cs gases, in contrast, the two-body loss rate for states, that can be trapped magnetically, is on the same order of magnitude. For this reason, Cs can only be condensed in optical traps and with tuning its interactions via Feshbach resonances. For our experiment, the loss rate in this state also poses a limit, which is the reason to prepare Cs in its ground state for most experiments.

4.4 Conclusion

A system of single Cs atoms interacting with an ultracold Rb gas was presented in this chapter. During the sympathetic cooling of single Cs atoms, the survival probability decays by an amount of only a few percent. While the impurity atoms are cooled by more than one order of magnitude, the Rb buffer gas is observed to remain unaffected. Three-body recombination was measured with atomic resolution, while again leaving the many-body system unchanged. By employing a species-selective trap, the impurity atom was tightly localized inside the ultracold Rb gas, demonstrating the doping of a many-body system with a spatially confined impurity.

Chapter 5

Conclusion and outlook

In this thesis, I have presented a method to prepare ultracold gases doped with an exactly known number of few and single impurity atoms. The sympathetic cooling of the impurity atoms without a significant decay of the survival probability was observed, where the temperature is limited only by the temperature of the ultracold Rb gas. The thermalization dynamics were analyzed to deduce the elastic interspecies scattering length. Inelastic three-body collisions were studied with atomic resolution, allowing to unambiguously assign losses to Rb-Rb-Cs three-body recombination.

These observations reveal the elementary properties of the interspecies interactions, that determine the properties of the hybrid system. The ratio of "bad" inelastic collisions to "good" elastic collisions was found to be favorable enough to perform experiments with the hybrid system, without the need of tuning the interspecies interactions. In all experiments, the buffer gas remains unaffected by the interaction with the impurity atoms, demonstrating the employment of single atoms as non-destructive probes for a many-body system. The presented hybrid system paves the way for a set of interesting scenarios.

For these scenarios, outlined in some detail below, mainly two requirements remain to be shown. The first one is to dope a BEC, rather than an ultracold, high phase-space density thermal gas, like employed for most of the studies described in this thesis. However, production of BECs in the employed traps was demonstrated and the presented preparation scheme should accordingly allow the doping of a BEC. Alternatively, a doped high phase-space density sample could be further evaporatively cooled to degeneracy. Secondly, tuning of the interspecies scattering length would allow to tailor the interactions in a controlled way, as was demonstrated in a variety of ultracold atom experiments. In a balanced Rb-Cs mixture, several interspecies Feshbach resonances have been observed in the absolute ground state [121]. By ap-

plying a homogeneous magnetic field to our hybrid system, tuning of the interaction should be immediately possible. It should be observable by enhanced three-body recombination, like in balanced mixtures. With these next steps, the proposals introduced in the following should be within reach.

5.1 Coherence properties of single atom impurities immersed in a BEC

Single neutral atoms are candidates for use as qubits in quantum information processing experiments [14, 31, 68, 122], where the quantum state is usually stored in internal states of the atom. In most manipulation and trapping schemes, a certain heating rate is unevitable. The decoherence time in these experiment is crucial, since it determines the storage time of quantum states. Higher temperatures usually cause shorter coherence times [72, 123], hence cooling of such qubits might be necessary. This cooling is not allowed to change the quantum state of the atom. A possible solution to this challenge has been proposed by the immersion of qubits into a BEC [36, 37]. Potentially, the atom could be cooled coherently and continuously in this way by transferring energy to excitations of the superfluid. Furthermore, excitation of the quantum gas could be employed to mediate interaction between two impurity atoms. Provided this interaction could be tailored adequately, even the entanglement of two impurities could be possible [124].

A similiar idea is to study the coherence of the BEC with the help of the impurity atom, as suggested in [40]. The basic concept here is to immerse a single atom prepared in a superposition of two internal states into a BEC and study the interaction of both sub-systems. By a species-selective trap, in the same manner like shown in the thermalization measurement in this thesis, the impurity atom could additionally be tightly localized inside the BEC, which would allow to spatially resolve the experiment. In another proposal, the interaction between an impurity atom trapped on a lattice site and an ensemble of probe atoms is studied. The adequate interactions provided, the probe atoms are reflected if the impurity atom is in one spin state, but transmitted if it is in another spin state. This could be exploited for a single-shot non-demolition read-out of the quantum state of the impurity atom [125].

For all these scenarios, coherent manipulation of the impurity atom is crucial. In a set of experiments, we studied the decoherence of single Cs atoms, stored in the running wave crossed dipole trap without Rb present, by Ramsey spectroscopy [123, 126]. In Fig. 5.1(a) a typical Ramsey fringe for a hold time $t_{\mathrm{hold}} = 500$ µs is shown. By measuring the contrast for different holding times, the decoherence time t_{deco} can be determined. The corresponding data is presented in Fig. 5.1(b),

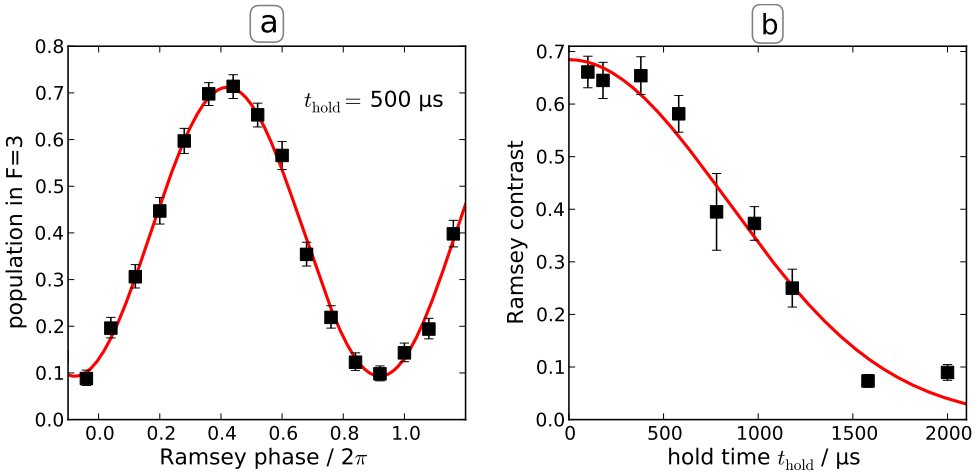

Figure 5.1: Ramsey spectroscopy of single Cs atoms. **a)** Ramsey fringe after a hold time of 500 µs. **b)** Ramsey contrast in dependence of the hold time, showing a decoherence time of $t_{\mathrm{co}} \approx 1.2$ ms. Details are discussed in the master thesis of Farina Kindermann [72].

yielding $t_{\mathrm{deco}} \approx 1.2$ ms. Details on these experiments can be found in the master thesis of Farina Kindermann [72]. In chapter 4, the lifetime of the impurity atom in both the hyperfine ground state ($F = 3$) and the excited state ($F = 4$) was found to be on the order of hundreds of ms, more than two orders of magnitude longer than the decoherence time t_{deco}. Hence, the study of an impurity atom in a superposition state immersed in the buffer gas would not be limited by inelastic three-body recombination. Furthermore, it was shown in this thesis, that single Cs atoms are sympathetically cooled within a few tens of ms. Therefore it could also be possible to observe the coherence of the impurity atom during sympathetic cooling. Unfortunately, a sudden vacuum leak detained us from continuing Ramsey spectroscopy with Rb stored in the trap.

5.2 Polaron physics

Another possible line of research is the investigation of polaron physics in our system. A single-atom impurity in a BEC is predicted to have a bound ground state in which it is self-localized [127, 128], provided strong enough interaction. In this polaronlike state, the atom distorts the surrounding density of the BEC which leads to a self-trapping potential. The polaron is suggested to be probed by "Bose-Nova" experiments, where a strong expansion of the BEC is observed in time-of-flight images [129]. An alternative probing method would be microwave or rf spectroscopy of the impurity atom. Formation of a polaron should be visible by a distinct peak

in the spectrum, as was demonstrated in Fermi polarons [38].

5.3 New apparatus – Choice of species

Since a new apparatus with the same research goal is currently designed, the question arises which atomic species are to be used. Rb and Cs are quite strongly interacting already without tuning, as was observed in this thesis. While a strong interaction is desired in principal, the drawback is a strong interspecies three-body recombination, limiting the lifetime of the impurity atom to several hundred ms. This time is sufficiently long for most envisioned experiments. Due to the long time scale for evaporative cooling of the buffer gas on the order of several seconds, the only way to prepare a doped many-body system with this choice of species is therefore to first prepare ultracold Rb, and then dope it with single Cs atoms. One relatively simple way to achieve this was presented in this thesis.

The three-body recombination rate scales with the density of the buffer gas squared. Experiments with higher buffer gas density will therefore lead to a farther shortened lifetime of the impurity atom. In these cases, the tuning of the interaction strength via Feshbach resonances could be necessary. Because intraspecies Cs interactions can be neglected in our case, tuning the interaction is not limited to regions were Cs interactions are small enough, like discussed above. This would provide a means to reduce the interaction strength and therefore elongate the lifetime of the impurity atom. The use of Rb has the advantage that BECs are easy to produce because of the favorable intraspecies scattering properties.

Another advantage of our species combination is the maximum possible difference of the wavelength of atomic transitions for a combination of stable Alkali atoms of about 70 nm. This allows the optical adressing of one species without affecting the other. In particular, we can operate a MOT to cool and trap single Cs atoms, while an ultracold Rb gas is stored inside the beam diameter of the Cs MOT, without affecting the Rb gas.

Overall, Rb and Cs seem to be good candidates also for future experiments. Therefore, the primary demand for the new apparatus will be a faster cycle time. Employing more recent technologies, mainly a two-dimensional MOT for a high flux atomic beam and an all-optical route to BEC, should shorten the time for one shot from about one minute to a few seconds.

Bibliography

[1] T.W. Hänsch and A.L. Schawlow. Cooling of gases by laser radiation. *Optics Communications*, 13(1):68–69, January 1975.

[2] S. Chu, L. Hollberg, J. E. Bjorkholm, A. Cable, and A. Ashkin. Three-dimensional viscous confinement and cooling of atoms by resonance radiation pressure. *Physical Review Letters*, 55(1):48–51, July 1985.

[3] N. Masuhara, J. M. Doyle, J. C. Sandberg, D. Kleppner, T. J. Greytak, H. F. Hess, and G. P. Kochanski. Evaporative cooling of Spin-Polarized atomic hydrogen. *Physical Review Letters*, 61(8):935–938, 1988.

[4] M. H. Anderson, J. R. Ensher, M. R. Matthews, C. E. Wieman, and E. A. Cornell. Observation of Bose-Einstein condensation in a dilute atomic vapor. *Science*, 269(5221):198 –201, July 1995.

[5] K. B. Davis, M. -O. Mewes, M. R. Andrews, N. J. van Druten, D. S. Durfee, D. M. Kurn, and W. Ketterle. Bose-Einstein condensation in a gas of sodium atoms. *Physical Review Letters*, 75(22):3969, November 1995.

[6] M. R. Andrews, C. G. Townsend, H.-J. Miesner, D. S. Durfee, D. M. Kurn, and W. Ketterle. Observation of interference between two bose condensates. *Science*, 275(5300):637 –641, January 1997.

[7] Z. Hadzibabic, S. Stock, B. Battelier, V. Bretin, and J. Dalibard. Interference of an array of independent Bose-Einstein condensates. *Physical Review Letters*, 93(18):180403, October 2004.

[8] K. W. Madison, F. Chevy, W. Wohlleben, and J. Dalibard. Vortex formation in a stirred Bose-Einstein condensate. *Physical Review Letters*, 84(5):806–809, January 2000.

[9] J. R. Abo-Shaeer, C. Raman, J. M. Vogels, and W. Ketterle. Observation of vortex lattices in Bose-Einstein condensates. *Science*, 292(5516):476 –479, April 2001.

[10] M.-O. Mewes, M.R. Andrews, D.M. Kurn, D.S. Durfee, C.G. Townsend, and W. Ketterle. Output coupler for Bose-Einstein condensed atoms. *Physical Review Letters*, 78(4):582–585, January 1997.

[11] I. Bloch, T. W. Hänsch, and T. Esslinger. Atom laser with a cw output coupler. *Physical Review Letters*, 82(15):3008, April 1999.

[12] G. Cennini, G. Ritt, C. Geckeler, and M. Weitz. All-Optical realization of an atom laser. *Physical Review Letters*, 91(24):240408, December 2003.

[13] I. Bloch, J. Dalibard, and W. Zwerger. Many-body physics with ultracold gases. *Reviews of Modern Physics*, 80(3):885, July 2008.

[14] D. Schrader, I. Dotsenko, M. Khudaverdyan, Y. Miroshnychenko, A. Rauschenbeutel, and D. Meschede. Neutral atom quantum register. *Physical Review Letters*, 93(15):150501, October 2004.

[15] M. Karski, L. Förster, J.-M. Choi, A. Steffen, W. Alt, D. Meschede, and A. Widera. Quantum walk in position space with single optically trapped atoms. *Science*, 325(5937):174 –177, July 2009.

[16] E. Urban, T. A. Johnson, T. Henage, L. Isenhower, D. D. Yavuz, T. G. Walker, and M. Saffman. Observation of rydberg blockade between two atoms. *Nat Phys*, 5(2):110–114, February 2009.

[17] Alpha Gaetan, Yevhen Miroshnychenko, Tatjana Wilk, Amodsen Chotia, Matthieu Viteau, Daniel Comparat, Pierre Pillet, Antoine Browaeys, and Philippe Grangier. Observation of collective excitation of two individual atoms in the rydberg blockade regime. *Nat Phys*, 5(2):115–118, February 2009.

[18] M. Karski, L. Förster, J. M. Choi, W. Alt, A. Widera, and D. Meschede. Nearest-Neighbor detection of atoms in a 1D optical lattice by fluorescence imaging. *Physical Review Letters*, 102(5):053001, February 2009.

[19] T. Gericke, P. Würtz, D. Reitz, T. Langen, and H. Ott. High-resolution scanning electron microscopy of an ultracold quantum gas. *Nat Phys*, 4(12):949–953, December 2008.

[20] W. S. Bakr, J. I. Gillen, A. Peng, S. Fölling, and M. Greiner. A quantum gas microscope for detecting single atoms in a hubbard-regime optical lattice. *Nature*, 462(7269):74–77, November 2009.

[21] J. F. Sherson, C. Weitenberg, M. Endres, M. Cheneau, I. Bloch, and S. Kuhr. Single-atom-resolved fluorescence imaging of an atomic mott insulator. *Nature*, 467(7311):68–72, 2010.

[22] Sebastian Will, Thorsten Best, Simon Braun, Ulrich Schneider, and Immanuel Bloch. Coherent interaction of a single fermion with a small bosonic field. *Physical Review Letters*, 106(11):115305, March 2011.

[23] F. Serwane, G. Zürn, T. Lompe, T. B. Ottenstein, A. N. Wenz, and S. Jochim. Deterministic preparation of a tunable Few-Fermion system. *Science*, 332(6027):336 –338, April 2011.

[24] C. Zipkes, S. Palzer, C. Sias, and M. Köhl. A trapped single ion inside a Bose-Einstein condensate. *Nature*, 464(7287):388–391, March 2010.

[25] S. Schmid, A. Härter, and J. Hecker Denschlag. Dynamics of a cold trapped ion in a Bose-Einstein condensate. *Physical Review Letters*, 105(13):133202, 2010.

[26] Christoph Zipkes, Lothar Ratschbacher, Carlo Sias, and Michael Köhl. Kinetics of a single trapped ion in an ultracold buffer gas. *New Journal of Physics*, 13(5):053020, May 2011.

[27] M. Tinkham. *Introduction to superconductivity*. Courier Dover Publications, 2004.

[28] S. Inouye, M. R. Andrews, J. Stenger, H.-J. Miesner, D. M. Stamper-Kurn, and W. Ketterle. Observation of feshbach resonances in a Bose-Einstein condensate. *Nature*, 392(6672):151–154, 1998.

[29] C. A. Stan, M. W. Zwierlein, C. H. Schunck, S. M. F. Raupach, and W. Ketterle. Observation of feshbach resonances between two different atomic species. *Physical Review Letters*, 93(14):143001, 2004.

[30] R. Wynar, R. S. Freeland, D. J. Han, C. Ryu, and D. J. Heinzen. Molecules in a Bose-Einstein condensate. *Science*, 287(5455):1016 –1019, February 2000.

[31] O. Mandel, M. Greiner, A. Widera, T. Rom, T. W. Hänsch, and I. Bloch. Controlled collisions for multi-particle entanglement of optically trapped atoms. *Nature*, 425(6961):937–940, October 2003.

[32] M. W. Zwierlein, C. A. Stan, C. H. Schunck, S. M. F. Raupach, A. J. Kerman, and W. Ketterle. Condensation of pairs of fermionic atoms near a feshbach resonance. *Physical Review Letters*, 92(12):120403, March 2004.

[33] M. Bartenstein, A. Altmeyer, S. Riedl, S. Jochim, C. Chin, J. Hecker Denschlag, and R. Grimm. Crossover from a molecular Bose-Einstein condensate to a degenerate fermi gas. *Physical Review Letters*, 92(12):120401, March 2004.

[34] C. A. Regal, M. Greiner, and D. S. Jin. Observation of resonance condensation of fermionic atom pairs. *Physical Review Letters*, 92(4):040403, January 2004.

[35] R. Gehr, J. Volz, G. Dubois, T. Steinmetz, Y. Colombe, B. L. Lev, R. Long, J. Estève, and J. Reichel. Cavity-Based single atom preparation and High-Fidelity hyperfine state readout. *Physical Review Letters*, 104(20):203602, May 2010.

[36] A. J. Daley, P. O. Fedichev, and P. Zoller. Single-atom cooling by superfluid immersion: A nondestructive method for qubits. *Physical Review A*, 69(2):022306, February 2004.

[37] A. Griessner, A. J. Daley, S. R. Clark, D. Jaksch, and P. Zoller. Dark-State cooling of atoms by superfluid immersion. *Physical Review Letters*, 97(22):220403, November 2006.

[38] A. Schirotzek, C.-H. Wu, A. Sommer, and M. W. Zwierlein. Observation of fermi polarons in a tunable fermi liquid of ultracold atoms. *Physical Review Letters*, 102(23):230402, June 2009.

[39] M. Bruderer and D. Jaksch. Probing BEC phase fluctuations with atomic quantum dots. *New Journal of Physics*, 8(6):87–87, June 2006.

[40] H. T. Ng and S. Bose. Single-atom-aided probe of the decoherence of a Bose-Einstein condensate. *Physical Review A*, 78(2):023610, 2008.

[41] C.-S. Chuu, F. Schreck, T. P. Meyrath, J. L. Hanssen, G. N. Price, and M. G. Raizen. Direct observation of Sub-Poissonian number statistics in a degenerate bose gas. *Physical Review Letters*, 95(26):260403, December 2005.

[42] W. S. Bakr, A. Peng, M. E. Tai, R. Ma, J. Simon, J. I. Gillen, S. Fölling, L. Pollet, and M. Greiner. Probing the Superfluid–to–Mott insulator transition at the Single-Atom level. *Science*, 329(5991):547 –550, July 2010.

[43] B. D. Esry, Chris H. Greene, and James P. Burke. Recombination of three atoms in the ultracold limit. *Physical Review Letters*, 83(9):1751, 1999.

[44] T. Weber, J. Herbig, M. Mark, H.-C. Nägerl, and R. Grimm. Three-Body recombination at large scattering lengths in an ultracold atomic gas. *Physical Review Letters*, 91(12):123201, 2003.

[45] S. Jochim, M. Bartenstein, A. Altmeyer, G. Hendl, C. Chin, J. Hecker Denschlag, and R. Grimm. Pure gas of optically trapped molecules created from fermionic atoms. *Physical Review Letters*, 91(24):240402, December 2003.

[46] E. Majorana. Atomi orientati in campo magnetico variabile. *Il Nuovo Cimento (1924-1942)*, 9(2):43–50, February 1932.

[47] T. Esslinger, I. Bloch, and T. W. Hänsch. Bose-Einstein condensation in a quadrupole-Ioffe-configuration trap. *Physical Review A*, 58(4):R2664, 1998.

[48] M. Greiner, I. Bloch, T. W. Hänsch, and T. Esslinger. Magnetic transport of trapped cold atoms over a large distance. *Physical Review A*, 63(3):031401, February 2001.

[49] C. Klempt, T. Henninger, O. Topic, J. Will, St. Falke, W. Ertmer, and J. Arlt. Transport of a quantum degenerate heteronuclear Bose-Fermi mixture in a harmonic trap. *The European Physical Journal D*, 48(1):6 pages, 2008.

[50] A. J. Leggett. Bose-Einstein condensation in the alkali gases: Some fundamental concepts. *Reviews of Modern Physics*, 73(2):307–356, April 2001.

[51] C. Pethick and H. Smith. *Bose-Einstein condensation in dilute gases*. Cambridge University Press, 2002.

[52] E. W. Streed, A. P. Chikkatur, T. L. Gustavson, M. Boyd, Y. Torii, D. Schneble, G. K. Campbell, D. E. Pritchard, and W. Ketterle. Large atom number Bose-Einstein condensate machines. *Review of Scientific Instruments*, 77(2):023106–023106–13, February 2006.

[53] A. L. Migdall, J. V. Prodan, W. D. Phillips, T. H. Bergeman, and H. J. Metcalf. First observation of magnetically trapped neutral atoms. *Physical Review Letters*, 54(24):2596–2599, June 1985.

[54] D. Frese. *Bose-Einstein Condensation of Rubidium: Towards Ultracold Binary Bosonic Mixtures*. PhD thesis, Rheinische Friedrich-Wilhelms-Universität Bonn, 2005.

[55] M. Haas, V. Leung, D. Frese, D. Haubrich, S. John, C. Weber, A. Rauschenbeutel, and D. Meschede. Species-selective microwave cooling of a mixture of rubidium and caesium atoms. *New Journal of Physics*, 9(5):147–147, May 2007.

[56] M. Haas. *Sympathetisches Kühlen in einer Rubidium-Cäsium-Mischung: Erzeugung ultrakalter Cäsiumatome.* PhD thesis, Rheinische Friedrich-Wilhelms-Universität Bonn, 2007.

[57] C. Weber. *Controlled few-body interactions in ultracold bosonic mixtures.* PhD thesis, Rheinische Friedrich-Wilhelms-Universität Bonn, 2010.

[58] S. John. *Towards single atom aided probing of an ultracold quantum gas.* PhD thesis, Rheinische Friedrich-Wilhelms-Universität Bonn, Bonn, 2011.

[59] P. D. Lett, R. N. Watts, C. I. Westbrook, W. D. Phillips, P. L. Gould, and H. J. Metcalf. Observation of atoms laser cooled below the doppler limit. *Physical Review Letters*, 61(2):169, July 1988.

[60] H. J. Metcalf and P. Van der Straten. *Laser cooling and trapping.* Springer, 1999.

[61] R. Grimm, M. Weidemüller, and Y.B. Ovchinnikov. Optical dipole traps for neutral atoms. *Advances in Atomic, Molecular, and Optical Physics*, 42:95–170, 2000.

[62] G. Breit and I. I. Rabi. Measurement of nuclear spin. *Physical Review*, 38(11):2082, 1931.

[63] W. Gerlach and O. Stern. Der experimentelle nachweis der richtungsquantelung im magnetfeld. *Zeitschrift für Physik*, 9(1):349–352, December 1922.

[64] Z. Hu and H. J. Kimble. Observation of a single atom in a magneto-optical trap. *Optics Letters*, 19(22):1888–1890, November 1994.

[65] D. Haubrich, H. Schadwinkel, F. Strauch, B. Ueberholz, R. Wynands, and D. Meschede. Observation of individual neutral atoms in magnetic and magneto-optical traps. *Europhysics Letters (EPL)*, 34(9):663–668, June 1996.

[66] F. Ruschewitz, D. Bettermann, J. L. Peng, and W. Ertmer. Statistical investigations on single trapped neutral atoms. *Europhysics Letters (EPL)*, 34:651–656, June 1996.

[67] S. Kuhr, W. Alt, D. Schrader, M. Müller, V. Gomer, and D. Meschede. Deterministic delivery of a single atom. *Science*, 293(5528):278–280, July 2001.

[68] N. Schlosser, G. Reymond, I. Protsenko, and P. Grangier. Sub-poissonian loading of single atoms in a microscopic dipole trap. *Nature*, 411(6841):1024–1027, June 2001.

[69] T. Grünzweig, A. Hilliard, M. McGovern, and M. F. Andersen. Near-deterministic preparation of a single atom in an optical microtrap. *Nat Phys*, 6(12):951–954, December 2010.

[70] T. Weikum. *Ein System zur Fluoreszenzdetektion einzelner Cäsiumatome in einem Rubidium-Bose-Einstein-Kondensat*. Diplomarbeit, Rheinische Friedrich-Wilhelms-Universität Bonn, 2009.

[71] C. Weber, S. John, N. Spethmann, D. Meschede, and A. Widera. Single cs atoms as collisional probes in a large rb magneto-optical trap. *Physical Review A*, 82(4):042722, October 2010.

[72] F. Kindermann. *Towards Coherent Control of a Single Cs Atom in an Ultracold Rb Cloud*. Master thesis, Rheinische Friedrich-Wilhelms-Universität Bonn, 2011.

[73] D. S Sivia and J Skilling. *Data analysis a Bayesian tutorial*. Oxford University Press, Oxford; New York, 2006.

[74] D. A. Steck. Cs d line data (revision 2.1.2, 12 august 2009). *http://steck.us/alkalidata/*, 2009.

[75] S. Kuhr. *A controlled quantum system of individual neutral atoms*. PhD thesis, Rheinische Friedrich-Wilhelms-Universität Bonn, 2003.

[76] W. Alt. *Optical control of single neutral atoms*. PhD thesis, Rheinische Friedrich-Wilhelms-Universität Bonn, 2004.

[77] D. Frese, B. Ueberholz, S. Kuhr, W. Alt, D. Schrader, V. Gomer, and D. Meschede. Single atoms in an optical dipole trap: Towards a deterministic source of cold atoms. *Physical Review Letters*, 85(18):3777, October 2000.

[78] R. A. Cline, J. D. Miller, M. R. Matthews, and D. J. Heinzen. Spin relaxation of optically trapped atoms by light scattering. *Optics Letters*, 19(3):207–209, February 1994.

[79] J. D. Miller, R. A. Cline, and D. J. Heinzen. Far-off-resonance optical trapping of atoms. *Physical Review A*, 47(6):R4567, June 1993.

[80] A. Fuhrmanek, A. M. Lance, C. Tuchendler, P. Grangier, Y. R. P. Sortais, and A. Browaeys. Imaging a single atom in a time-of-flight experiment. *New Journal of Physics*, 12:053028, May 2010.

[81] L. Förster, M. Karski, J.-M. Choi, A. Steffen, W. Alt, D. Meschede, A. Widera, E. Montano, J. H. Lee, W. Rakreungdet, and P. S. Jessen. Microwave control of atomic motion in optical lattices. *Physical Review Letters*, 103(23):233001, 2009.

[82] G. van Rossum and F.L. Drake. Python reference manual, PythonLabs, virginia, USA, 2001. available at http://www.python.org. 2001.

[83] E. Jones, T. Oliphant, and P. Peterson. SciPy: open source scientific tools for Python, http://www.scipy.org/. 2001.

[84] C. Tuchendler, A. M. Lance, A. Browaeys, Y. R. P. Sortais, and P. Grangier. Energy distribution and cooling of a single atom in an optical tweezer. *Physical Review A*, 78(3):033425, 2008.

[85] L. J. LeBlanc and J. H. Thywissen. Species-specific optical lattices. *Physical Review A*, 75(5):053612, May 2007.

[86] J. Weiner, V. S. Bagnato, S. Zilio, and P. S. Julienne. Experiments and theory in cold and ultracold collisions. *Reviews of Modern Physics*, 71(1):1, January 1999.

[87] M. Anderlini and D. Guéry-Odelin. Thermalization in mixtures of ultracold gases. *Physical Review A*, 73(3):032706, March 2006.

[88] M. Greiner, C. A. Regal, J. T. Stewart, and D. S. Jin. Probing Pair-Correlated fermionic atoms through correlations in atom shot noise. *Physical Review Letters*, 94(11):110401, March 2005.

[89] A. J. Moerdijk and B. J. Verhaar. Collisional two- and three-body decay rates of dilute quantum gases at ultralow temperatures. *Physical Review A*, 53(1):R19–R22, January 1996.

[90] C. Chin, R. Grimm, P. Julienne, and E. Tiesinga. Feshbach resonances in ultracold gases. *Reviews of Modern Physics*, 82(2):1225, April 2010.

[91] E. G. M. van Kempen, S. J. J. M. F. Kokkelmans, D. J. Heinzen, and B. J. Verhaar. Interisotope determination of ultracold rubidium interactions from three High-Precision experiments. *Physical Review Letters*, 88(9):093201, February 2002.

[92] P.J. Leo, C.J. Williams, and P.S. Julienne. Collision properties of ultracold cs-133 atoms. *Physical Review Letters*, 85(13):2721–2724, September 2000.

[93] D.A. Steck. Rubidium d line data (revision 2.1.2, 12 august 2009). *http://steck.us/alkalidata/*, 2009.

[94] P. F. Bedaque, Eric Braaten, and H.-W. Hammer. Three-body recombination in bose gases with large scattering length. *Physical Review Letters*, 85(5):908–911, July 2000.

[95] P. O. Fedichev, M. W. Reynolds, and G. V. Shlyapnikov. Three-Body recombination of ultracold atoms to a weakly bound s level. *Physical Review Letters*, 77(14):2921–2924, 1996.

[96] J. Stenger, S. Inouye, M. R. Andrews, H.-J. Miesner, D. M. Stamper-Kurn, and W. Ketterle. Strongly enhanced inelastic collisions in a Bose-Einstein condensate near feshbach resonances. *Physical Review Letters*, 82(12):2422–2425, March 1999.

[97] J. L. Roberts, N. R. Claussen, S. L. Cornish, and C. E. Wieman. Magnetic field dependence of ultracold inelastic collisions near a feshbach resonance. *Physical Review Letters*, 85(4):728–731, July 2000.

[98] P. R. Bevington and K. D. Robinson. *Data Reduction and Error Analysis for the Physical Sciences*. Mcgraw-Hill Higher Education, 3. a. edition, August 2002.

[99] M. Arndt, M. Ben Dahan, D. Guéry-Odelin, M. W. Reynolds, and J. Dalibard. Observation of a Zero-Energy resonance in Cs-Cs collisions. *Physical Review Letters*, 79(4):625, July 1997.

[100] G. Delannoy, S. G. Murdoch, V. Boyer, V. Josse, P. Bouyer, and A. Aspect. Understanding the production of dual Bose-Einstein condensation with sympathetic cooling. *Physical Review A*, 63(5):051602, April 2001.

[101] M. Mudrich, S. Kraft, K. Singer, R. Grimm, A. Mosk, and M. Weidemüller. Sympathetic cooling with two atomic species in an optical trap. *Physical Review Letters*, 88(25):253001, June 2002.

[102] A. Mosk, S. Kraft, M. Mudrich, K. Singer, W. Wohlleben, R. Grimm, and M. Weidemüller. Mixture of ultracold lithium and cesium atoms in an optical dipole trap. *Applied Physics B: Lasers and Optics*, 73(8):791–799, December 2001.

[103] M. Mudrich. *Interactions in an optically trapped mixture of ultracold lithium and cesium atoms: Thermalization, spin-exchange collisions and photoassociation*. PhD thesis, Ruperto-Carola University of Heidelberg, 2003.

[104] D. M. Stamper-Kurn, H.-J. Miesner, S. Inouye, M. R. Andrews, and W. Ketterle. Collisionless and hydrodynamic excitations of a Bose-Einstein condensate. *Physical Review Letters*, 81(3):500–503, July 1998.

[105] V. Vuletic, A.J. Kerman, C. Chin, and S. Chu. Observation of low-field feshbach resonances in collisions of cesium atoms. *Physical Review Letters*, 82(7):1406–1409, February 1999.

[106] I. Shvarchuck, Ch. Buggle, D. S. Petrov, M. Kemmann, W. von Klitzing, G. V. Shlyapnikov, and J. T. M. Walraven. Hydrodynamic behavior in expanding thermal clouds of ^{87}Rb. *Physical Review A*, 68(6):063603, December 2003.

[107] Ch. Buggle, P. Pedri, W. von Klitzing, and J. T. M. Walraven. Shape oscillations in nondegenerate bose gases: Transition from the collisionless to the hydrodynamic regime. *Physical Review A*, 72(4):043610, October 2005.

[108] M. Anderlini, E. Courtade, M. Cristiani, D. Cossart, D. Ciampini, C. Sias, O. Morsch, and E. Arimondo. Sympathetic cooling and collisional properties of a Rb-Cs mixture. *Physical Review A*, 71(6):061401, June 2005.

[109] A. D. Lercher, T. Takekoshi, M. Debatin, B. Schuster, R. Rameshan, F. Ferlaino, R. Grimm, and H.-C. Nägerl. Production of a dual-species Bose-Einstein condensate of rb and cs atoms. *The European Physical Journal D*, March 2011.

[110] D. M. Stamper-Kurn, M. R. Andrews, A. P. Chikkatur, S. Inouye, H.-J. Miesner, J. Stenger, and W. Ketterle. Optical confinement of a Bose-Einstein condensate. *Physical Review Letters*, 80(10):2027, March 1998.

[111] A. Marte. *Feshbach-Resonanzen bei Stößen ultrakalter Rubidiumatome*. Dissertation, Technische Universität München, 2003.

[112] J. Söding, D. Guéry-Odelin, P. Desbiolles, F. Chevy, H. Inamori, and J. Dalibard. Three-body decay of a rubidium Bose–Einstein condensate. *Applied Physics B: Lasers and Optics*, 69(4):257–261, 1999.

[113] E. A. Burt, R. W. Ghrist, C. J. Myatt, M. J. Holland, E. A. Cornell, and C. E. Wieman. Coherence, correlations, and collisions: What one learns about Bose-Einstein condensates from their decay. *Physical Review Letters*, 79(3):337, July 1997.

[114] H.W. Cho, D.J. McCarron, D. L. Jenkin, M. P. Köppinger, and S. L. Cornish. A high phase-space density mixture of ^{87}Rb and ^{133}Cs: towards ultracold heteronuclear molecules. *The European Physical Journal D*, April 2011.

[115] C. Chin, V. Vuletic, A.J. Kerman, and S. Chu. High resolution feshbach spectroscopy of cesium. *Physical Review Letters*, 85(13):2717–2720, September 2000.

[116] T. Weber, J. Herbig, M. Mark, H.-C. Nägerl, and R. Grimm. Bose-Einstein condensation of cesium. *Science*, 299(5604):232–235, January 2003.

[117] D. J. McCarron, H. W. Cho, D. L. Jenkin, M. P. Köppinger, and S. L. Cornish. Dual-species Bose-Einstein condensate of rb87 and cs133. *Physical Review A*, 84(1):011603, July 2011.

[118] P. S. Julienne, F. H. Mies, E. Tiesinga, and C. J. Williams. Collisional stability of double bose condensates. *Physical Review Letters*, 78(10):1880–1883, March 1997.

[119] J. Söding, D. Guery-Odelin, P. Desbiolles, G. Ferrari, and J. Dalibard. Giant spin relaxation of an ultracold cesium gas. *Physical Review Letters*, 80(9):1869–1872, March 1998.

[120] D. Guéry-Odelin, J. Söding, P. Desbiolles, and J. Dalibard. Is Bose-Einstein condensation of atomic cesium possible? *Europhysics Letters (EPL)*, 44(1):25–30, October 1998.

[121] K. Pilch, A. D. Lange, A. Prantner, G. Kerner, F. Ferlaino, H.-C. Nägerl, and R. Grimm. Observation of interspecies feshbach resonances in an ultracold Rb-Cs mixture. *Physical Review A*, 79(4):042718, April 2009.

[122] P. Treutlein, T. Steinmetz, Y. Colombe, B. Lev, P. Hommelhoff, J. Reichel, M. Greiner, O. Mandel, A. Widera, T. Rom, I. Bloch, and TheodorW Hänsch. Quantum information processing in optical lattices and magnetic microtraps. *Fortschritte der Physik*, 54(8-10):702–718, August 2006.

[123] S. Kuhr, W. Alt, D. Schrader, I. Dotsenko, Y. Miroshnychenko, W. Rosenfeld, M. Khudaverdyan, V. Gomer, A. Rauschenbeutel, and D. Meschede. Coherence properties and quantum state transportation in an optical conveyor belt. *Physical Review Letters*, 91(21):213002, November 2003.

[124] A. Klein and M. Fleischhauer. Interaction of impurity atoms in Bose-Einstein condensates. *Physical Review A*, 71(3):033605, March 2005.

[125] A. Micheli, A. J. Daley, D. Jaksch, and P. Zoller. Single atom transistor in a 1D optical lattice. *Physical Review Letters*, 93(14):140408, October 2004.

[126] N. F. Ramsey. A molecular beam resonance method with separated oscillating fields. *Physical Review*, 78(6):695–699, June 1950.

[127] R. M. Kalas and D. Blume. Interaction-induced localization of an impurity in a trapped Bose-Einstein condensate. *Physical Review A*, 73(4):043608, April 2006.

[128] F. M. Cucchietti and E. Timmermans. Strong-Coupling polarons in dilute gas Bose-Einstein condensates. *Physical Review Letters*, 96(21):210401, June 2006.

[129] S. L. Cornish, N. R. Claussen, J. L. Roberts, E. A. Cornell, and C. E. Wieman. Stable ^{85}Rb Bose-Einstein condensates with widely tunable interactions. *Physical Review Letters*, 85(9):1795, 2000.